Connecting 3D printing parameters and mechanical properties of FDM polymers: Experiments and modelling

Sara Garzón Hernández

A dissertation submitted in partial fulfilment of the requirements for the degree of Doctor in Mechanical Engineering and Industrial Organisation

Universidad Carlos III de Madrid

Advisors:
Daniel García González
Ángel Arias Hernández

November 2019

Agradecimientos

En primer lugar, me agradecer a mis directores Ángel Arias y Daniel García la confianza que depositaron en mi hace ahora más de tres años y que hoy culmina con esta tesis. Agradecer a Ángel por el aprendizaje y oportunidades que me ha ofrecido durante estos años. Agradecer a Daniel por creer en mí, por su dedicación en esta tesis, por sus consejos, conocimientos y amistad.

Al profesor Antoine Jerusalém, supervisor durante mi estancia doctoral, y al Departamento of Engineering Sciene de University of Oxford por su contribución a esta investigación. Sus ideas, aportaciones y equipos experimentales han sido fundamentales para el completar el desarrollo de esta tesis doctoral.

Al departamento de Mecánica de Medios Continuos y Teoría de Estructuras, por toda la experiencia y apoyo durante estos años. A los técnicos de laboratorio David y Sergio por ayuda tanto el en desarrollo de los estudios experimentales de esta tesis como en el resto de los trabajos experimentales llevadas a cabo durante mi doctorado. A los que empezaron siendo compañeros y hoy son amigos: Luis, Nacho, Andrés, Pablo, Óscar, Ramón, Mahy, Damián, Javi, Lorena, Pablo... En especial agradecer a Nacho su ayuda directa en la componente experimental de esta tesis.

A todos aquellos amigos que han estado a mi lado durante estos años. Especialmente a mis amigas Patricia, Noelia y Alicia, por su amistad, consejos y apoyo, tanto en los momentos buenos como especialmente en los malos. Y a todos esos "amigos" a los que llamo familia.

Por último, agradecer a mis padres, mi hermano y mis abuelos, por apoyarme en todas mis decisiones y estar presentes siempre, y especialmente en los momentos duros que he pasado durante la realización de esta tesis, lo cual reconozco, no ha tenido que ser tarea fácil. Nunca tendré palabras suficientes para ellos.

Resumen

Los polímeros tradicionales presentan un comportamiento mecánico no lineal y dependiente de la temperatura y velocidad de deformación. A este complejo comportamiento, hay que añadirle una dependencia extra con los parámetros de impresión cuando se trata con piezas fabricadas por impresión 3D. Todas estas dependencias hacen que la caracterización mecánica y el modelado de polímeros impresos por 3D sean complejos. Entre todas las tecnologías de impresión 3D, el modelado por deposición fundida (FDM) es la más común para trabajar con polímeros termoplásticos. Toda pieza fabricada por FDM presenta cierta porosidad y una respuesta mecánica anisótropa debidas al propio proceso de fabricación. Sin embargo, lejos de ver esto como una desventaja, FDM puede permitir fabricar piezas con propiedades mecánicas a medida mediante el control de los parámetros del proceso de impresión.

Esta tesis doctoral profundiza en el estudio de la relación entre los parámetros de impresión y las propiedades mecánicas de piezas poliméricas fabricadas por FDM. Para ello, es necesario estudiar y comprender la mecánica y termodinámica del proceso de impresión para avanzar en el conocimiento de la relación última entre parámetros de impresión y propiedades mecánicas. El objetivo final de esta tesis ha sido desarrollar herramientas de análisis y un modelo constitutivo para predecir la respuesta mecánica de termoplásticos fabricados por impresión 3D. Para alcanzar este objetivo, esta tesis se ha dividido en tres bloques principales:

i. El primer bloque proporciona una caracterización experimental de la mesostructura y del comportamiento mecánico de probetas fabricadas por FDM. Se ha estudiado la influencia del espesor de capa, la orientación de impresión y el número de capas. Además, a partir de observaciones experimentales, se han desarrollado expresiones analíticas para la predicción de la densidad de vacíos y las propiedades mecánicas.

ii. En el segundo bloque se han desarrollado modelos térmicos y de sinterización que permiten analizar la mecánica y termodinámica del proceso de impresión. Estos modelos han permitido estudiar el proceso de unión entre filamentos que tiene lugar durante la fabricación y la influencia de los parámetros de impresión sobre la mesostructura de piezas fabricadas por FDM. La combinación de estos modelos con las expresiones analíticas propuestas en el bloque previo, han permitido

crear una metodología para predecir las propiedades mecánicas en función de los parámetros de impresión. Esta metodología proporciona los fundamentos sobre las características de los termoplásticos fabricados por FDM que motiva futuros modelos para la optimización de las propiedades mecánicas en función de los requisitos de servicio.

iii. Finalmente, basado en observaciones experimentales, el tercer bloque presenta un modelo anisótropo visco-hiperelástico del continuo para polímeros fabricados por FDM. Este modelo incluye la dependencia de la respuesta mecánica con los parámetros de impresión analizados.

La metodología propuesta en esta tesis se ha aplicado a un caso específico, incluyendo experimentación y simulaciones computacionales sobre el Acrilonitrilo Butadieno Estireno (ABS). Este termoplástico ha sido elegido, sin pérdida de generalidad, por ser uno de los materiales más empleados en FDM.

Abstract

Traditional polymers present a complex mechanical behaviour by means of nonlinearity, temperature and rate dependencies. To these complexities, we need to add extra dependencies on printing process parameters when dealing with components manufactured by 3D printing. All these dependencies together make the characterisation and modelling of 3D printed polymers very challenging. Among all the 3D printing techniques, fused deposition modelling (FDM) is the most common for thermoplastic components. FDM components are porous materials with an anisotropic behaviour derived from the manufacturing process. However, despite it can seem a disadvantage, customised mechanical properties can be obtained by controlling these variables through the printing process.

This doctoral dissertation deepens in the understanding of the relationship between the printing parameters and mechanical properties of FDM polymers. In this regard, it is also necessary to deal with the study of the mechanics and thermodynamics of the printing process. The final aim of this thesis is to provide analytical tools and a continuum mechanics constitutive model to predict the mechanical response of 3D printed thermoplastics. To this end, this thesis is composed of three principal blocks:

i. The first block provides an experimental characterisation of the mesostructure and mechanical performance of FDM components. The influence of layer height, raster orientation and number of layers is studied. On the other hand, from the experimental observations, analytical expressions for the prediction of the void density and mechanical properties are developed.

ii. In the second block, the mechanics and thermodynamics of the FDM process are studied through the development of thermal and sintering models. These permit to analyse the bonding process that takes place during the manufacturing process and study the influence of the printing parameters on the mesostructure of the FDM components. The combination of these models with the analytical expressions developed in the previous block allows for the proposal of a methodology to predict the final mechanical properties as a function of the printing parameters. This methodology provides the fundamentals of FDM thermoplastic characteristics to motivate further models and tools for optimisation of the mechanical properties as a function of the final requirements *in service*.

iii. Finally, based on experimental observations, an anisotropic viscous-hyperelastic constitutive model for FDM polymers is developed in the third block. This model includes the dependence of the printing parameters on the mechanical behaviour.

The methodology proposed in this thesis has been applied to a specific case, including experiments and computational simulations on Acrylonitrile Butadiene Styrene (ABS). This FDM thermoplastic has been chosen, without loss of generality, because it is one of the most common solutions for FDM components.

Contents

List of Figures

List of Tables

1 Introduction

This doctoral research aims at analysing the mechanical behaviour of 3D printed polymers and the influence of the printing process on it. To this end, this dissertation develops a complete study going from an experimental characterisation of the mechanical response of 3D printed polymers to constitutive modelling.

1.1 Motivation of the research

Additive manufacturing (AM) technologies are in continuous development and progressively incorporated into numerous manufacturing processes (Bandyopadhyay and Bose, 2015). Among the other names used for AM, such as rapid prototyping or solid freeform fabrication, the most common is three-dimensional (3D) printing. Contrary to traditional manufacturing, which fabricates products by removing material, AM techniques fabricate components by the addition of material. This comes down to efficient use of the material and minimal waste while offering components with satisfactory accuracy in geometry (Srivatsan and Sudarshan, 2015). Moreover, 3D printing allows for building 3D designs directly from a computer-aided design (CAD) file without the need for specific tools or dies (Bandyopadhyay and Bose, 2015).

Since the manufacture of the first printer in 1988, the AM market has been evolving reaching approximately $1850 million in 2012 and having been projected almost the double in 2017 (Bandyopadhyay and Bose, 2015). Therefore, industrialised rapid manufacturing has been positioned on the cup of emerging technologies providing shorter production times and great flexibility in the design (Bandyopadhyay and Bose, 2015).

The original technologies were developed for quick prototyping by the use of polymeric materials. However, this initial purpose has been moved, over the last years, into the idea of fabricating functional parts incorporating other materials. Nowadays, the different AM processes allow for the use of various materials such as polymers, composites, metals and ceramics. Currently, the use of polymers in 3D printing remains primarily intended

for the manufacture of prototypes; however, the incorporation of new polymers for 3D printing has opened the opportunity to manufacture polymeric functional parts.

Despite all these advantages, 3D printing techniques offer inferior mechanical properties due to their manufacture process by layers (Ngo et al., 2018). Multiple layers are deposited in the plane (X–Y direction), one on top of the other, building the third dimension (Z) (Bandyopadhyay and Bose, 2015). This causes additional porosity resulting in anisotropic behaviour. Therefore, unlike thermoplastic polymers manufactured by other traditional techniques, the mechanical response of 3D printed polymers is highly influenced by the printing and process parameters.

However, far from considering the porosity and anisotropy as disadvantages, they allow for the customisation of mechanical properties by controlling the influence of printing parameters. Although there have been many authors approaching this study in the last years, there is still an absence of adequate tools that allow for the optimisation of the printing parameters as a function of the final requirements.

In order to deepen in the control of the mechanical performance of 3D printed polymers, this doctoral dissertation proposes the study of the influence of printing parameters on the mechanical properties of 3D printed polymers. Thus, this research connects experimental results with modelling tools, providing a breakthrough in the future customisation of mechanical properties of 3D printed polymers.

1.2 Objectives and methodology

This doctoral dissertation deals with the study of the influence of printing parameters on the mechanical behaviour of 3D printed polymers. The final aim is to develop modelling tools for the prediction of the mechanical behaviour of these materials. To this end, it is necessary to study the mechanics and thermodynamics of the 3D printing process.

Among all the AM technologies for polymers, this research focuses on fused deposition modelling (FDM), a specific manufacturing process for thermoplastic materials.

To achieve the main purpose, some specific objectives have been established as follows:

i. Experimental characterisation of the influence of 3D printing on the mesostructural and mechanical properties of FDM thermoplastics; and development of analytical expressions for the prediction of these properties. To this end, starting from the analysis of the studies available in the literature, the most relevant printing parameters are identified. The mesostructural characterisation analyses the influence of these printing parameters on porosity and internal geometry of the 3D printed structures. For the mechanical characterisation, an experimental campaign is proposed through the development of uniaxial tensile test under quasi-static conditions at two different strain rates. In addition, analytical expressions are proposed based on experimental results for the prediction of void density and mechanical properties.

ii. Analysis of the thermodynamics of the FDM process. The understanding of the final properties of these materials requires the identification of the different processes that take place from the extrusion to deposition and the subsequent bonding process between adjacent filaments. This analysis is accompanied by the development of thermal and sintering models.

iii. Modelling of the manufacturing process and prediction of the mechanical properties through the proposal of a methodology combining the tools developed in the previous tasks.

iv. Development of a continuum constitutive model for FDM polymers formulated for finite deformations within a thermodynamically consistent framework.

1.3 Outline of the research

This doctoral dissertation is divided into seven chapters following the objectives and tasks presented above:

- **Chapter 1**. This chapter introduces the motivation of this research as well as the objectives and methodology followed to archive them.
- **Chapter 2**. This chapter presents the bases for the further development of this doctoral research. First, an introduction of the additive manufacturing technologies is presented. Then, an analysis of the mechanical behaviour of thermoplastic polymers and 3D thermoplastic polymers is introduced. Lastly, a review of modelling approaches used to model the mechanical response of thermoplastics and 3D printed thermoplastics is presented. These provide the basis for the further development of the continuum constitutive model.
- **Chapter 3**. The mesostructure and mechanical behaviour of FDM polymers are highly influenced by the manufacturing process. In order to study the influence of printing parameters on both structural and mechanical properties of FDM thermoplastics, a complete characterisation program is conducted. Specifically, the study focuses on the influence of layer height, raster orientation and number of layers on FDM acrylonitrile butadiene styrene (ABS) components. In addition, based on the results obtained from the mechanical characterisation, analytical expressions are proposed for the prediction of void density and mechanical properties as a function of the printing parameters studied.
- **Chapter 4**. This chapter deals with a thermodynamic analysis of the FDM printing process. This chapter provides an adequate understanding of the FDM process and the development of thermal and sintering models that allow the reproduction of the bonding process between filaments.

- **Chapter 5**. This chapter combines the thermal and sintering models developed in Chapter 4 with the analytical expressions proposed in Chapter 3 to develop a methodology that allows for the prediction of the structural and mechanical properties of 3D printed polymers. This takes the printing parameters and filament properties as input data. Finally, this methodology allows us to provide a parametric study from end-to-end simulations of the printing process and analyse the effects of different manufacturing parameters in the mechanical performance of ABS components.

- **Chapter 6**. A new hyperelastic constitutive model for FDM polymers is proposed based on the experimental observations and data obtained in previous chapters. This model describes the mechanical behaviour of porous materials with a transversally isotropic response. Furthermore, it takes into account strain rate and printing parameters dependencies. While the dependency with the layer height is captured by the void density (porosity), a softening model is included to capture the dependency with the number of layers. The model is validated with FDM ABS components manufactured with different printing parameters and tested at different strain rates.

- **Chapter 7**. The main conclusions of this work, along with some research proposals for future works, are presented in the last chapter.

Finally, **Appendix A** presents the fundamentals of continuum mechanics, which are the bases for the development of the constitutive model for 3D printed polymers, and **Appendix B** provides the planes of the grips used in the tests developed for the experimental mechanical characterisation.

2 State of the art

This chapter is devoted to introducing the bases needed for the further development of this Doctoral Research. To this end, the outline of the chapter is as follows: in Section 2.1, a summary of the different additive manufacturing technologies is presented, focusing especially on the description of fused deposition modelling (FDM) process; in Section 2.2, the mechanical behaviour of thermoplastic polymers is analysed as well as the mechanical responses of polymeric structures manufactured by 3D printing; in Section 2.3, some hyperelastic models presented in the literature are introduced. In addition, a review of modelling approaches to define the mechanical response of 3D printed polymers to date is introduced.

2.1 State of the art: additive manufacturing

Additive manufacturing (AM) is defined as a 'process of joining materials to make objects from 3D model data, usually layer upon layer' (ASTM F2792-12a, 2012). Moreover, the term 3D printing defines 'the fabrication of objects through the deposition of a material using a print head, nozzle or another printer technology'. Although both terms are often used as synonymous, 3D printing is particularly associated with machines that are low end in price and overall capability. The first 3D printing technology to appear was stereolithography (SL) developed by Charles Hull in 1986 (Hull, 1986). This development was followed by others such as powder bed fusion, FDM and inkjet printing (Ngo et al., 2018).

Among the advantages of these technologies, one finds the fabrication of complex geometries, flexibility in design permitting personal customization and a decrease in cost and time (Ngo et al., 2018). Initially, 3D printers have been used to manufacture prototypes. However, nowadays, AM is used in a wide variety of industries such as aeronautics, biomechanics and construction, where it is used for manufacturing from

prototypes to products (Ngo et al., 2018). In addition, novel materials and methodologies are continuously being developed (Ngo et al., 2018).

A wide range of material such as metals, polymers, composites, ceramics and even concrete are used in 3D printing. The advanced in metals and alloys for their use in 3D printing technologies has permitted its inclusion in the aerospace and automotive industries. Regarding the polymers employed in 3D printing, Polylactic acid (PLA) and acrylonitrile butadiene styrene (ABS) are the main choices, although high performance polymers such as Polyether ether ketone (PEEK) are increasingly being used for this purpose.

AM technologies can be categorized into seven groups: blinder jetting, directed energy deposition, material extrusion, material jetting, powder bed fusion, sheet lamination and vat photopolymerization (ASTM F2792-12a, 2012). These categories permit the classification of the different AM processes attending to the type of machines, the state of starting material and the working principle used for the manufacturing, Table 2.1. Among the different 3D printing technologies used to fabricate polymeric components, FDM, selective laser sintering and stereolithography are some of the most well-established (Wang et al., 2017).

Table 2.1 Additive Manufacturing Process Categories (ASTM F2792-12a, 2012).

Additive Manufacturing processes	State of starting materials	Working principle
Binder jetting	Powder	Liquid bonding agent
Directed energy deposition	Wire or powder	Thermal energy
Material extrusion	Filament	Extrusion through a nozzle
Material jetting	Droplets	UV light
Powder bed fusion	Powder	Thermal energy
Sheet lamination	Sheets of material	Adhesive or welding process
Vat photopolymerization	Liquid photopolymer	UV light

FDM is a material extrusion process in which a thermoplastic filament goes through a heated extruder and the material is deposited layer-by-layer. Polycarbonate (PC), ABS and PLA are the most common thermoplastic used with this technology due to their low melting temperature (Wang et al., 2017). However, nowadays the variety of thermoplastics with a high melting point, such a PEEK, and reinforced thermoplastics such as carbon fibre reinforced PLA, are available for FDM.

Selective laser sintering (SLS) is a powder bed fusion process where one or more lasers selectively fuse or melt the particles at the surface layer by layer. Different types of powdered materials can be used such as polymers, metals or ceramics.

Finally, stereolithography (SLA) is a vat photopolymerization process where a photopolymer material in liquid state is selectively cured and harden to a predetermined thickness using one or more lasers. Acrylic and epoxy resins are the most used polymers for SLA (Wang et al., 2017). The main advantage of this technology is the high resolution of the finals printed components (Wang et al., 2017).

Despite the advantages that AM techniques offer in terms of versatility, cost and time reductions, the inferior mechanical properties and the anisotropic behaviour of 3D printed components are still the principal inconvenient of 3D printing (Ngo et al., 2018). Due to the manufacturing process by layers, additional porosity is created, reducing the interfacial bonding between layers (Ngo et al., 2018; Wang et al., 2017). The extent of the void formation depends on the 3D printing technique, being more relevant in methods that use materials in the form of filaments like FDM (Ngo et al., 2018; Wang et al., 2017). However, although the porosity is normally considered as a defect, there are some applications such as the design of scaffolds in tissue engineering (Ngo et al., 2018) where this porosity can constitute an advantage. In addition, due to the nature of layer-by-layer, the microstructure inside the layer is different than at the boundaries between layers, giving place to an anisotropic behaviour (Ngo et al., 2018). For all these aspects, it is important to have control over the flaw sensitivity and anisotropic behaviour (Ngo et al., 2018).

2.1.1 Fused Deposition Modelling (FDM)

Among the different technologies that comprise the 3D printing term, FDM is the most used for polymeric materials. As stated before for this technology, the state of the starting materials is a filament that is extruded through a heated nozzle and deposited as a thread of molten material (raster) on the platform (Rankouhi et al., 2016). When a layer is finished, an additional layer is deposited on top of each other until the 3D component is finished (Rankouhi et al., 2016).

This technology is commonly used with thermoplastic materials with a low melting point; however, during the last years, different 3D printers have been developed to reach a higher range of extrusion temperatures permitting the use of thermoplastics with a higher melting point or metals.

A large number of variables have a great influence on FDM processes, see Figure 2.1.

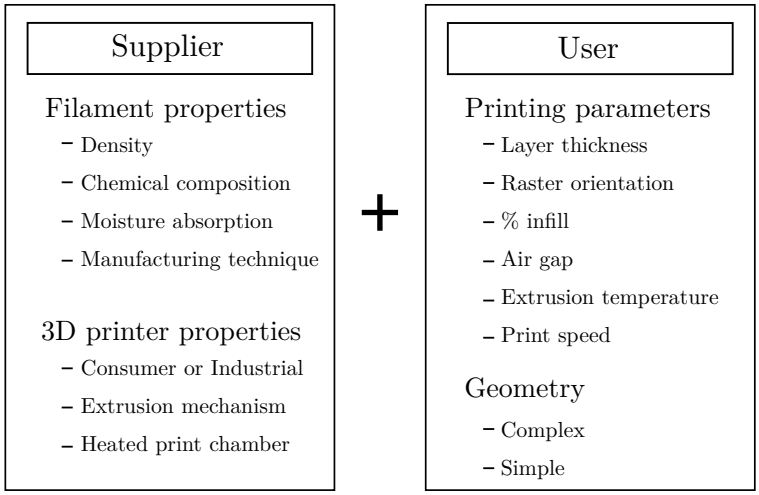

Figure 2.1 Influential parameters for components manufactured by FDM, adapted from Rankouhi et al. (2016).

As users, we do not have control over some variables that affect the properties of the final components, such as the filament properties or the 3D printer characteristics. However, the user is responsible for defining the printing parameters. To understand the influence of these parameters in the final appearance and mechanical properties of the component, it is necessary to know the different steps that take place during the printing processes as well as the influence of different printing parameters. Therefore, in the next subsection, the definition of the printing parameters and the complete process of design and printing is introduced.

2.1.1.1 Printing parameters and G-code definition

The building process of a 3D printed structure starts with the definition of the geometrical features in a computer-aided design (CAD) model that is exported as a stereolithography (STL or 'Standard Triangle Language') file. Then, a slicer software is necessary to slice the 3D model into a build file of 2D layers (Cantrell et al., 2017) that subsequently is converted into the specific instructions for the 3D printer (Wang et al., 2017). These instructions define the deposition path. Apart from the geometry, defined in the STL file, the slicer software needs the selected set of printing parameters to create the output file, known as G-Code. G-Code is the set of commands used to control the nozzles' movement, as well as the speed and the amount of filament needed to extrude in each move. During the modelling process, the material is deposited as a raster following the tour previously designed.

Among the huge number of printing parameters that can be defined by the user, the most relevant are layer height, line width, air gap and raster angle. The layer height defines the thickness of each layer that composes the final component. On the other

hand, the line width defines the width of each raster. Both parameters define the volume of material that has to be extruded between two G-Code lines. The air gap determines the distance between rasters, see Figure 2.2. Zero air gap defines a distance between the centres of rasters equal to the line width. Positive air gap results in non-joint of rasters, while negative air gap results in an overlay between rasters. Finally, the raster orientation defines the infill angle, being the most convenient configuration alternating layers 90°, see Figure 2.3.

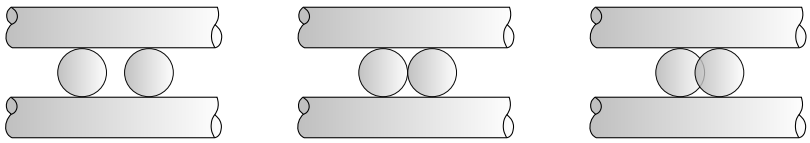

Figure 2.2 Definition of air gap parameter.

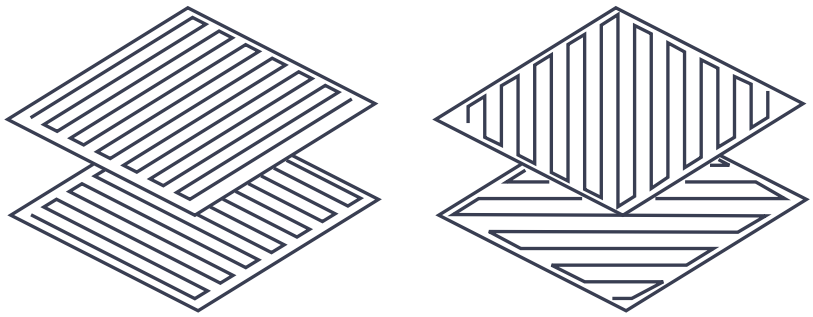

Figure 2.3 Definition of raster orientation.

Once the printing parameters are defined, the slicer software determines the coordinate of each movement necessary for manufacturing. At the beginning of G-code, some instructions define the necessary temperatures for the extruder and the heat bed. The different code lines that define each movement are specified by an initial standard G-Code command, GXXX, followed by the coordinates X, Y, Z. The commands X and Y define the position on the platform to which the extruder must move. The command Z defines the height at which it must place, whose value corresponds to the layer height specified by the user. In addition, in any code line, the command E controls the length of filament to feed into the extruder between the start and endpoints. To do so, the 3D printer first calculates the volume of material that must be deposited between two points, which is calculated as

$$V = HWL \tag{2.1}$$

where H and W are the printing parameters of layer height and line width, and L is the distance between the start and endpoints, which is calculated as a function of the coordinates of each point (x_i, y_i) as

$$L = \sqrt{(x_1 - x_2)^2 + (y_1 + y_2)^2} \tag{2.2}$$

Finally, the length of filament needed to fill that volume is obtained as

$$E = \frac{V}{\pi(\frac{\phi}{2})^2} \tag{2.3}$$

with ϕ being the diameter of the filament.

The space for the deposition of the material is delimited at the bottom by the platform or the previous layer deposited, and by the extruder at the top, while the material flows freely on the sides. Therefore, taking a single filament, the geometry expected is described in Figure 2.4.

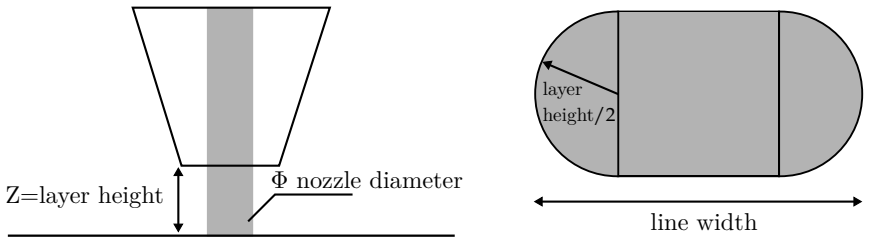

Figure 2.4 Cross-sectional geometry of a filament.

However, this geometry can undergo changes since immediately after the deposition of a filament, it starts to cool from extrusion temperature to environmental temperature (Bahr and Westkamper, 2018) while bonding with the adjacent filaments (Bellehumeur et al., 2004; Sun et al., 2008).

2.2 Thermoplastic materials and 3D printed thermoplastic materials

To understand the mechanical response of 3D printed thermoplastics, it is necessary to know the behaviour of these polymers manufactured by conventional techniques. In this section, a summary of the mechanical behaviour of polymers is presented as well as a review of the response of thermoplastics components manufactured by FDM.

2.2.1 Mechanical behaviour of conventional thermoplastic polymers

Polymers are a class of material whose microstructure contains many different length scales. Their smaller chemical repeat unit is the monomer (Bergström, 2015a). These monomers are linked into chain molecules which form a macromolecular network (Bergström, 2015a).

There are many different approaches to categorize polymers. Based on their properties, polymers can be classified as elastomers, thermoplastics or thermosets (Bower, 2002). Elastomers or rubbers are network polymers that are lightly crosslinked and they are reversibly stretchable to high extensions. Because of the cross-links, they can not melt and flow. Moreover, they become glassy or partially crystallised on cooling (Bower, 2002). Thermoplastic polymers consist of linear or branched molecules. They soften or melt when heated (Bower, 2002) being able to be exposed to different temperature cycles without suffering significant degradation (Bergström, 2015a). Thermoplastic materials can be separated into amorphous and semi-crystalline polymers. In amorphous polymers, molecules form an entangled network with a random structure (Bergström, 2015a). On the other hand, in semi-crystalline polymers, part of the molecular structure is crystalline, consisting of layered lamellar crystals, and the other part is amorphous (Bergström, 2015a). Semi-crystalline polymers have a true melting temperature T_m. At temperatures above T_m, crystalline domains break up and become disordered (Bergström, 2015a). Regarding amorphous polymers and the amorphous region of semi-crystalline polymers, they do not present melting temperature but soften significantly at temperatures above glass transition temperature T_g (Bergström, 2015a). This temperature T_g defines a transition from high to low Young's modulus. In addition, both types of thermoplastics have a ductile to brittle transition temperature whereby at temperatures below it, a brittle failure is expected (Laiarinandrasana et al., 2009), see Figure 2.5. Regarding thermoset polymers, they are network polymers heavily cross-linked (Bower, 2002). These polymers, unlike thermoplastics, cannot be melt and they decompose at high enough temperature (Bower, 2002).

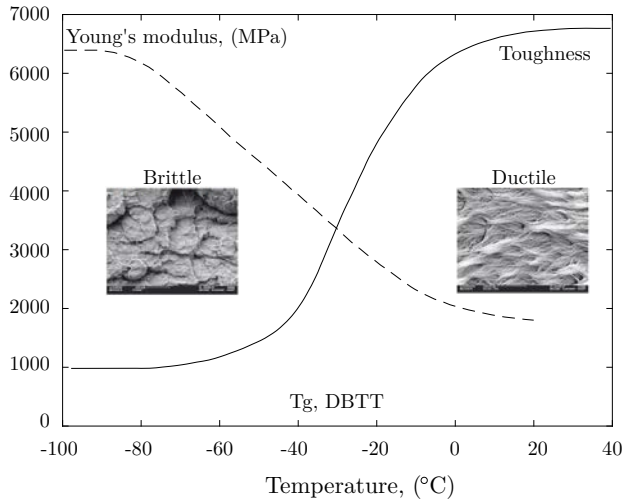

Figure 2.5 Evolution of Young's modulus and toughness versus temperature for glassy polymers (Laiarinandrasana et al., 2009).

Mechanical properties of polymers are highly dependent on temperature and strain rate (Bower, 2002). In addition, polymers are viscoelastic materials that exhibit properties of viscous liquids and elastics solids (Bower, 2002). At high temperatures or low strain rates, polymers may be rubber-like, reaching lower Young's modulus and yield stress and being able to withstand large extensions without permanent deformations. On the contrary, when temperature decreases or strain rate increases, a loss in ductility and continuous hardening is observed. Therefore, polymers may be glass-like, reaching higher Young's modulus and yield stress.

Below the yield point, polymers present an elastic behaviour being able to recover the initial strain when stress is removed. However, above this point, either permanent deformation or fracture are reached after removing the stress. Figure 2.6 shows different possible load-extension curves for a polymer: (a) shows extension with brittle fracture, (b) localised yielding followed by fracture, (c) elastic linear region followed by necking, cold drawing and work hardening process, (d) homogeneous deformation without distinct yield point and (e) rubber-like behaviour (Bower, 2002). Due to the dependences of the mechanical behaviour with temperature and strain rate, most thermoplastic polymers can display all the different behaviours under the appropriate conditions.

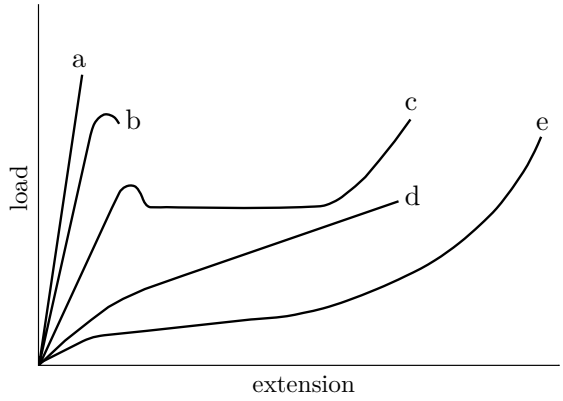

Figure 2.6 Different possible load-extension curves for a polymer (Bower, 2002).

During the deformation process, shear banding can be produced showing an orientation along directions of principal shear stress, Figure 2.7. This mechanism is observed under tension and compression conditions and is a primary mechanism in amorphous glassy polymers. In addition, the development of necks during yielding is formed via shear bands.

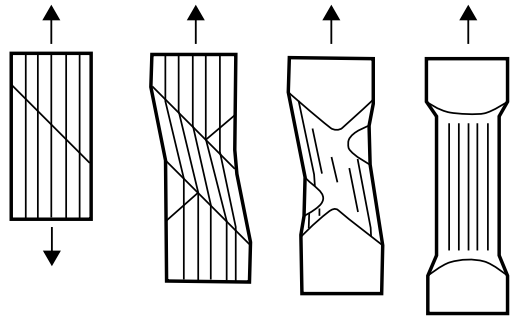

Figure 2.7 Shear banding.

Crazing is another phenomenon observed in some polymers that leads to microvoid formation in a plane perpendicular to the maximum principal tensile stress. This microvoids growth and coalesce leading to the formation of cracks. Contrary to shear banding, crazing takes place only under tension conditions. This phenomenon occurs in regions of high hydrostatic stress state, or in regions of very localized yielding. When thermoplastics are stressed, stress-whitening zones can be observed being a sign of crazing in some cases. While shear banding is more prevalent in semi-crystalline polymers, crazing is typical in amorphous and glassy polymers.

On the other hand, the cavitation phenomenon is observed in many semi-crystalline polymers deformed at temperatures above glass transition (Pawlak et al., 2014). Moreover,

this phenomenon is observed in rubbers, crosslinked and glassy polymers. As crazing, cavitation is produced under tension conditions but do not form in compression or shear.

Among the conventional processing methods for polymers, injection moulding, extrusion and blow moulding can be found (Bower, 2002). While injection moulding allows for complex shapes, the shape obtained by extrusion depends on the shape of the die. Moreover, blow moulding is used for the manufacturing of hollow products.

2.2.1.1 Thermoplastics used in 3D printing

ABS and PLA are two of the most used thermoplastics in FDM. Therefore, the understanding of the mechanical behaviour of these materials under conventional manufacturing processes becomes essential.

Truss and Chadwick (1976) studied the effect of the strain rate and temperature on the tensile response of ABS specimens manufactured by injection moulding. The typical load-extension curve of ABS is shown in Figure 2.8a. In this curve, five different regions can be seen. Initially, there is an elastic and linear region (1) followed by an elastic non-linear region (2). The yield point coincides with the maximum stress (3). After reaching the yield point, there is a strain softening region (4). Finally, the plastic flow continues at constant stress (5). A range from 10^{-4} to 10^{-1} s^{-1} was studied at room temperature tests. Before reaching or near yield point, two different behaviours were observed depending on the strain rate. At low strain rates, diffuse shear zones appeared on the edges of the specimen and began to propagate obliquely into it, producing necking on the surface. On the other hand, at high strain rate, no distinct between shear zones was observed although, at the yield point, a general clouding was observed along the whole gauge length. After the yield point, during the load drop, the shear bands appeared over the whole gauge length and began to propagate slowly into the specimen. Finally, during the period of extension at constant or slightly decreasing load, a continued stress whitening is produced. In all the cases, fracture occurs perpendicular to the applied stress at highly stress whitened region of the gauge length, see Figure 2.8b.

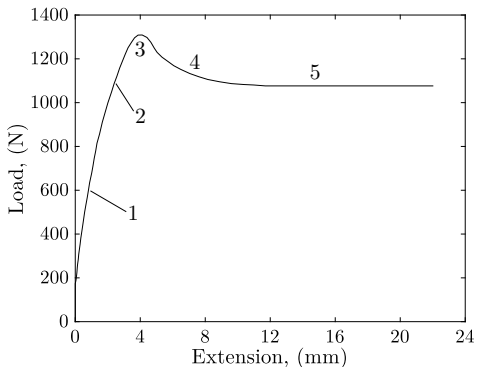

(a)

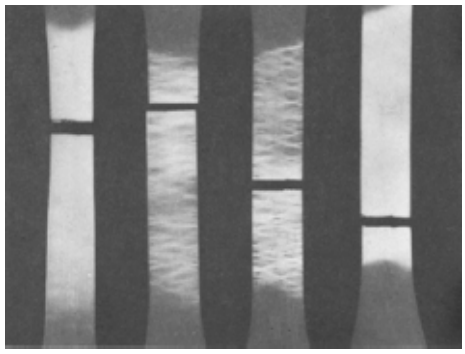

(b)

Figure 2.8 (a) ABS load-extension curve; (b) Fracture at 1.3910^{-4} s^{-1}, 1.3910^{-3} s^{-1}, 1.3910^{-2} s^{-1}, 1.3910^{-1} s^{-1} *and room temperature (Truss and Chadwick, 1976).*

On the other hand, uniaxial tensile tests covering a temperature range from 293 K to 198 K at different strain rates were conducted. Yield stress increases linearly when the temperature decreases. Similar fracture than that described at room temperature tests was observed at low temperatures.

Regarding PLA, it is a biodegradable and bioactive thermoplastic polymer obtained by synthesized of lactic acid (or lactide) from renewable resources like corn or sugarcane. PLA is a semi-crystalline polymer PLA with a relatively high T_g, around 58°, and low T_m, around 180° as compared to other thermoplastics (Lim et al., 2008). Thus, it is suitable for their use in FDM. On contrary to ABS, this polymer presents a brittle mechanical behaviour, with good strength and stiffness (Lim et al., 2008).

2.2.2 Mechanical behaviour of FDM thermoplastic polymers

As for thermoplastic materials, 3D printed thermoplastic polymers exhibit strain rate dependency. This dependency has been observed on FDM processed components by few authors (Rodríguez et al., 2001; Song et al., 2017; Vairis et al., 2016). Rodríguez et al. (2001) studied the effect of strain rate for a range from 10^{-5} to 10^{-2} s^{-1} on ABS specimens with a longitudinal raster orientation, see Figure 2.9. A noticeable increase in the yield stress is observed as strain rate increases, following a logarithmic tendency for both cases. Moreover, a drastic reduction in toughness occurs at the slowest strain rate on FDM specimens. Moreover, Vairis et al. (2016) studied the influence of strain rate on FDM ABS specimens manufactured with a diagonal or 45° raster orientation for the same range of strain rates. An increase in elastic modulus and yield strength was observed as strain rate increases, being more significant the effect on yield strength. In addition, this tendency was also observed by Song et al. (2017) for 3D printed PLA specimens.

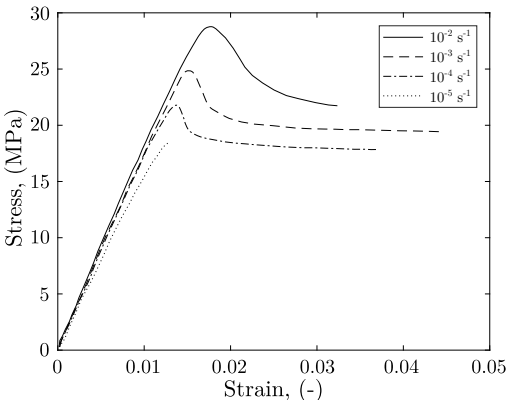

Figure 2.9 Strain rate effects on the longitudinal FDM-ABS components manufactured with an air gap of -25.4 μm (Rodríguez et al., 2001).

The higher porosity due to manufactured layer upon layer is one of the particularities of AM. This porosity, along with the interfacial bonding between layers reached, determines the mechanical properties of the components. For the FDM technique, due to each layer is composed by a specific number of rasters, the formation of voids is more common than in other technologies and is considered one of the main inconvenient (Ngo et al., 2018; Wang et al., 2017). The distribution of this porosity is mainly determined by the build orientation, that is, how the 3D model is positioned on the platform, and by the infill raster orientation (Chacón et al., 2017; Torrado and Roberson, 2016). Therefore, this porosity produces a marked anisotropic behaviour, playing the raster orientation an important role in the mechanical properties of the components manufactured by FDM. Moreover, the strength of the bond formed between filaments will be another factor to take into account, see Figure 2.10.

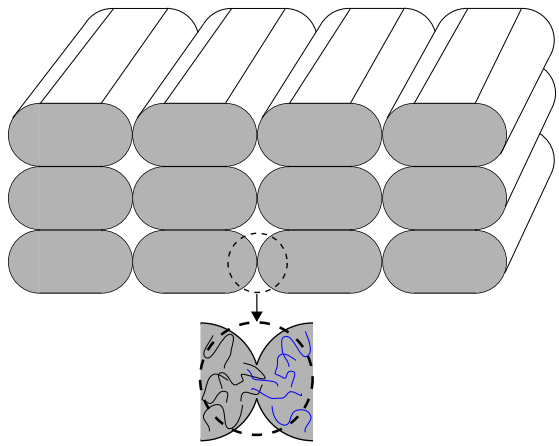

Figure 2.10 Mesostructure and inter filament bonding of FDM components.

Both void density and fibre-to-fibre bond strength are influenced by the printing and process parameters. Thus, numerous studies have shown the influence of these parameters on the final mechanical response. While the influence of build orientation has not been widely studied (Chacón et al., 2017; Torrado and Roberson, 2016), the influence of the raster orientation has been studied by numerous authors (Ahn et al., 2002; Rankouhi et al., 2016; Rodríguez et al., 2001; Torrado and Roberson, 2016; Ziemian et al., 2012; Zou et al., 2016). Chacón et al. (2017) studied the influence of the build orientation on PLA specimens manufactured with three different combinations, see Figure 2.11. *Upright* samples showed the lowest strength and stiffness performance. This effect was also observed by Torrado and Roberson (2016) on ABS specimens. On the other hand, *On its edge* samples showed the most ductile stress-strain response and the best flexural performance.

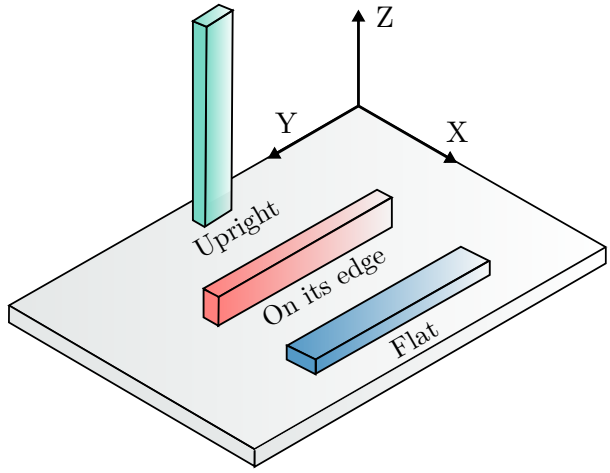

Figure 2.11 Build orientation.

Regarding the influence of raster orientation, different studies have shown that specimens manufactured with a raster orientation of 0° or longitudinal for all the layers, understanding that as a parallel direction to the stress axis direction in a tensile test, present the highest tensile performance. These results can be explained by the fact that molecules tend to align along the stress axis direction. On the other hand, specimens manufactured with a raster angle of 90° or transversal for all the layers, understanding that as the direction of printing in which the raster is perpendicular to the stress axis, present the weakest tensile performance. This is expected due to the fact that, in tensile tests, the loads are taken by the bond between filaments, and not by the filaments themselves (Ziemian et al., 2012). However, in both cases, the mechanical properties are worst than the ones obtained with the virgin filament, as shown by Rodríguez et al. (2001), see Figure 2.12. These differences are attributed to the presence of voids in FDM specimens and the differences in the degree of molecular orientation. In addition,

different failure modes are observed depending on the raster orientation. For the case of 90 and 45°, the failure path follows that orientation and is produced along the bond between filaments, which is the weakest path (Rodríguez et al., 2001; Ziemian et al., 2012). Moreover, specimens with raster orientation of 0° fail primarily in the transverse direction. ABS specimens with longitudinal orientations show craze formation and growth is observed to develop before the yield stress is reached (Rodríguez et al., 2001; Ziemian et al., 2012). Craze nucleation occurs at the edge and the centre of the specimen and then broads (Rodríguez et al., 2001). Failure occurs in the whitened region due to the crazed process (Rodríguez et al., 2001). The same tendencies are observed under flexural conditions while, under compression, the best response is observed with a raster orientation of 90° (Ziemian et al., 2012). However, the mechanical response under compression is not as affected by this parameter as under tensile conditions.

On the other hand, both layer thickness and air gap have a great influence on the void ratio. Rankouhi et al. (2016) analysed the influence of layer thickness providing that void ratio decreases when layer thickness decreases, while the mechanical response improves in terms of elastic modulus and yield stress. In addition, Ahn et al. (2002) studied the influence of the air gap showing that the use of negative air gap increases both strength and stiffness.

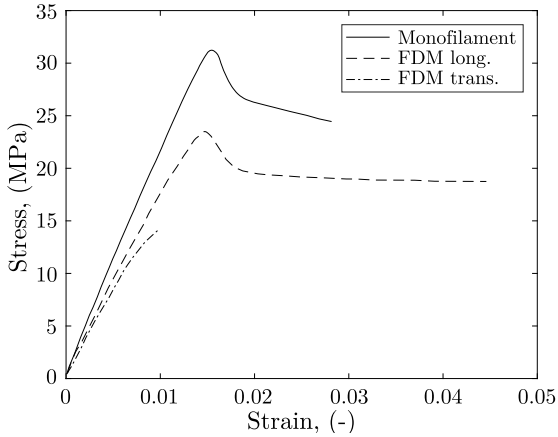

Figure 2.12 Comparison of the stress-strain response of FDM-ABS components manufactured at different raster orientations and monofilament ABS (Rodríguez et al., 2001).

Lastly, the influence of other process parameters as the extrusion temperature has also been analysed. Aliheidari et al. (2017) characterized the fracture resistance and the interlayer adhesion of ABS samples manufactured by FDM at three different extrusion temperatures: 210, 230 and 240 °C. Higher apparent fracture and interlayer fracture resistances are reached when the extrusion temperature increases. In addition, an increase of 53% of the ratio between the real fracture surface area and the apparent fracture surface area (without considering voids) is obtained when the temperature increases

from 210 to 240 °C. Figure 2.13 shows the representative fracture surfaces where the differences in terms of void density are observed. Therefore, this study showed that the interfacial area is affected by the printed temperature.

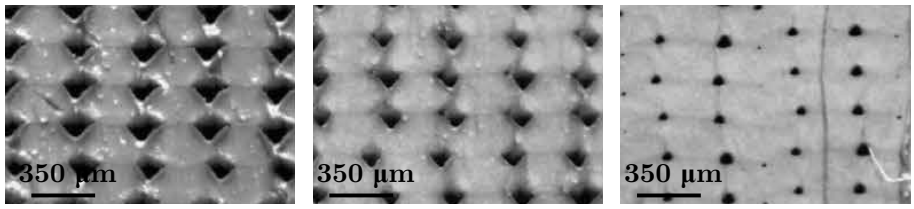

(a) *(b)* *(c)*

Figure 2.13 Micrographs of specimens manufactured at temperatures of: (a) 210 °C; (b) 230 °C; (c) 240 °C (Aliheidari et al., 2017).

2.3 Constitutive models

This section introduces a summary of some constitutive models found in the literature for the prediction of mechanical responses of thermoplastic polymers. In addition, a review of the modelling of 3D printed polymers developed to date is presented.

2.3.1 Thermoplastic modelling

As stated in the previous section, thermoplastic materials present a complex mechanical behaviour. This behaviour is temperature, strain rate and pressure dependent, reaching large deformations and, in some cases, with a nonlinear material response. As a consequence, polymers are modelled as hyperelastic materials.

Hyperelasticity is a generalization of linear elasticity for nonlinear material behaviours and suitable for large deformations (Bergström, 2015c). The definition of these constitutive models is based on an energetic potential from which the stress is derived. In addition, these energetic potentials can describe the micromechanics that drive the deformation process of polymers. A summary of the fundamentals of hyperelastic constitutive modelling can be found in Appendix A.

2.3.1.1 Hyperelastic energy density functions

Among the different hyperelastic models, the Mooney-Rivlin (MR) model is one of the most commonly used ones. In this model, the Helmholtz free energy per unit reference volume is defined as

$$\Psi(C_{10}, C_{01}, k) = C_{10}\,(I_1^* - 3) + C_{01}\,(I_2^* - 3) \tag{2.4}$$

where $I_1^* = tr(\mathbf{C^*})$ and $I_2^* = \frac{1}{2}[I_1^* - \mathbf{C^*} : \mathbf{C^*}]$ are the deviatoric first and second strain invariants, $\mathbf{C^*}$ is the deviatoric right Cauchy-Green deformation tensor and C_{10} and C_{01} are material parameters.

This model is an extension of the classical neo-Hookean (NH) model. NH model is based on two parameters, shear modulus μ and bulk modulus k, and is a particular case of MR model ($C_{10} = \mu$ and $C_{01} = 0$). In this case, the strain energy density is based only on the first strain invariant as

$$\Psi(I_1^*) = \frac{\mu}{2}\left(I_1^* - 3\right) \tag{2.5}$$

Other model based on the first invariant is the proposed by Yeoh where the strain energy density function adopts the form

$$\Psi(C_{10}, C_{20}, C_{30}, k) = \sum_{i=1}^{N} C_{i0}\left(I_1^* - 3\right)^i \tag{2.6}$$

The models presented previously describe the isochoric response. In this regard, the full definition of the energetic potential needs to incorporate a volumetric component. Usually, this volumetric response is defined by a constant bulk modulus κ by $\frac{\kappa}{2}\left(J-1\right)^2$, where $J = \det \mathbf{F}$ is the Jacobian determinant.

Motivated by the deformation behaviour of the microstructure of elastomers, Arruda and Boyce (1993b) proposed a statistical model where parameters are physically motivated known as eight-chain model. The parameters are linked to chain orientations involved in the deformation of a three-dimensional network structure of the rubber. In this regard, the model is based on the assumption that chain molecules on average are located along the diagonals of a unit cell, Figure 2.14. The energy density function is defined as

$$\Psi = nk_B\theta N\left(\left(\frac{\bar{\lambda}_L}{\bar{\lambda}}\right)\beta + \ln\frac{\beta}{\sinh\beta}\right) \tag{2.7}$$

where $\beta = \mathfrak{L}^{-1}\left(\frac{\bar{\lambda}}{\bar{\lambda}_L}\right)$, $\bar{\lambda}_L$ is the locking stretch, $\bar{\lambda}$ is the average total stretch ratio, n is the chain density, k_B the Boltzmann constant, θ the temperature and N the number of chain segments per chain.

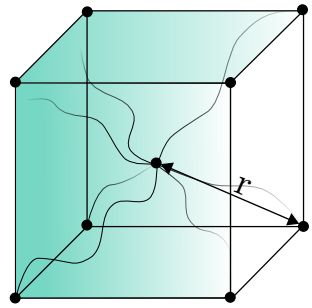

Figure 2.14 Location of the eight chain molecules in the unit cell, adapted from Arruda and Boyce (1993b).

All these models are able to capture the nonlinear elastic behaviour of polymers. However, in Section 2.2, it has been seen that some polymers also exhibit viscous characteristics. In this regard, more complex models have been proposed in the literature to describe the nonlinear response and rate and temperature dependencies.

2.3.1.2 Viscoelastic and viscoplastic hyperelastic models

Among the different viscoelastic and viscoplastic hyperelastic models proposed in the literature, a complete description of two models are presented here: the Arruda-Boyce model and Garcia-Gonzalez et al. (2018a) model.

- **Arruda-Boyce (AB) model**

  Arruda and Boyce (1993a) proposed a viscoplastic model for predicting large strain, rate and temperature effects of glassy polymers. In addition, the model allows for predicting strain softening effects. The model is built on the assumption that there are two resistances to deformation in glassy polymers: an isotropic resistance to chain segment rotation and an anisotropic resistance to molecular alignment. The rheological representation is shown in Figure 2.15, where the kinematics of the model is based on the decomposition of the total deformation gradient into elastic and plastic components, $\mathbf{F} = \mathbf{F^e}\mathbf{F^p}$. Therefore, the material response can be interpreted as two networks acting in series: one elastic network (e) and one elastoplastic network (p).

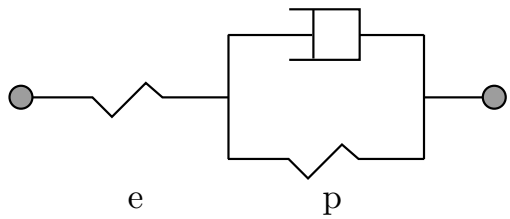

Figure 2.15 Rheological scheme of the AB model.

Following the decomposition of the deformation gradient, the Cauchy stress can be calculated from the linear elastic spring as

$$\boldsymbol{\sigma} = \frac{1}{J^e}\left(2\mu^e \mathbf{E^e} + \lambda^e tr(\mathbf{E^e})\mathbf{I}\right) \tag{2.8}$$

where $\mathbf{E^e} = tr(\mathbf{V^e})$ is the logarithmic true strain, $\mathbf{V^e}$ is the left stretch tensor of the elastic component of the deformation gradient $\mathbf{F^e} = \mathbf{V^e}\mathbf{R^e}$, and μ^e and λ^e are Lamé's constants.

On the other hand, the plastic rate flow is given by

$$\dot{\gamma}_p = \dot{\gamma}_0 \exp\left[-\frac{As}{k_B\theta}\left(1 - \left(\frac{\tau}{s}\right)^{5/6}\right)\right] \tag{2.9}$$

where $\dot{\gamma}_0$ and As are material constants, θ is the absolute temperature, k_B is Boltzmann's constant and τ the effective equivalent shear stress. In addition, the strain softening is modelled through the evolution of the athermal shear strength s as

$$\dot{s} = h\left(1 - \frac{s}{s_{ss}}\right)\dot{\gamma}_p \tag{2.10}$$

where h is the softening slope and s_{ss} is a preferred state of the shear stress.

The stress driving the plastic flow is obtained as the difference between the total stress $\boldsymbol{\sigma}$ and the convected back stress $\boldsymbol{\sigma^p}$

$$\boldsymbol{\sigma^*} = \boldsymbol{\sigma} - \frac{1}{J^e}\mathbf{F^e}\boldsymbol{\sigma^p}\mathbf{F^p}^T \tag{2.11}$$

The deviatoric back stress can be expressed by the incompressible form of the eight-chain model

$$\boldsymbol{\sigma^p} = \frac{\mu^p}{\bar{\lambda}^p}\mathfrak{L}^{-1}\left(\frac{\bar{\lambda}^p/\bar{\lambda}^p_{lock}}{1/\bar{\lambda}^p_{lock}}\right) dev\left(\mathbf{B^p}\right) \tag{2.12}$$

where μ^p and $\bar{\lambda}^p_{lock}$ are material constants, physically motivated, $\mathbf{B^p} = \mathbf{F^p}\mathbf{F^p}^T$ and $\bar{\lambda}^p = (tr(\mathbf{B^p})/3)^{1/2}$ is the effective chain stretch.

Finally, the rate of plastic deformation is given by

$$\mathbf{D^p} = \dot{\gamma}_p \frac{dev[\boldsymbol{\sigma^*}]}{\tau} \tag{2.13}$$

while the plastic spin is taken to be zero and where the effective equivalent stress is $\tau = \sqrt{\frac{1}{2}dev[\boldsymbol{\sigma^*}] : dev[\boldsymbol{\sigma^*}]}$.

- **Garcia-Gonzalez et al. (2018a) model**

  Recently, Garcia-Gonzalez et al. (2018a) have developed a constitutive model for semi-crystalline polymers that combines viscoelastic and viscoplastic responses. In addition, this model takes into account material hardening due to strain rate sensitivity, temperature evolution during the deformation process due to heat generation induced by plastic dissipation, thermal softening and thermal expansion effects.

  The constitutive model is composed of three resistances to deformation (each one conforming a constitutive branch), see Figure 2.16. The intermolecular resistance represents an intermolecular barrier to deformation and accounts for rate-dependent viscoplasticity. Molecular orientation arising from the polymeric network (network resistance) is defined as purely elastic. Additionally, a viscoelastic resistance is introduced to accounts for rate dependences during the recoverable deformation region (viscoelasticity). Note that these viscous contributions lead to local temperature increments resulting in thermal softening and favouring deformation instabilities.

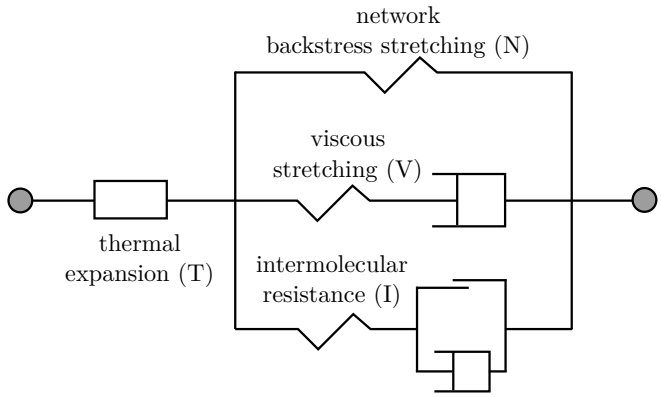

Figure 2.16 Rheological scheme of the Garcia-Gonzalez et al. (2018a) model.

According to the kinematics shown in Figure 2.17, the deformation gradient $\mathbf{F} = \mathbf{F}^{\mathbf{M}}\mathbf{F}^{\boldsymbol{\theta}}$ can be decomposed into thermal $\mathbf{F}^{\boldsymbol{\theta}}$ and mechanical $\mathbf{F}^{\mathbf{M}}$ parts. Moreover, the mechanical part is equivalent for the three constitutive branches on decomposed as

$$\mathbf{F}^{\mathbf{M}} = \mathbf{F}^{\mathbf{e}}_{\mathbf{I}}\mathbf{F}^{\mathbf{p}}_{\mathbf{I}} = \mathbf{F}^{\mathbf{e}}_{\mathbf{V}}\mathbf{F}^{\boldsymbol{\nu}}_{\mathbf{V}} = \mathbf{F}^{\mathbf{e}}_{\mathbf{N}} \tag{2.14}$$

where $\mathbf{F}^{\mathbf{e}}_{\mathbf{I}}$ and $\mathbf{F}^{\mathbf{p}}_{\mathbf{I}}$ are the elastic and plastic components of the intermolecular resistance; $\mathbf{F}^{\mathbf{e}}_{\mathbf{V}}$ and $\mathbf{F}^{\boldsymbol{\nu}}_{\mathbf{V}}$ are the elastic and viscous components of the viscoelastic resistance, and; $\mathbf{F}^{\mathbf{e}}_{\mathbf{N}}$ the pure elastic part of the network resistance.

The velocity gradient $\mathbf{l}$ can be written in terms of the kinematics as

$$\begin{aligned}\mathbf{l} = \dot{\mathbf{F}}\mathbf{F}^{-1} = \mathbf{l}_{\mathbf{V}}^{\mathbf{e}} + \mathbf{F}_{\mathbf{V}}^{\mathbf{e}}\tilde{\mathbf{L}}_{\mathbf{V}}^{\boldsymbol{\nu}}\mathbf{F}_{\mathbf{V}}^{-\mathbf{e}} + \mathbf{F}_{\mathbf{V}}^{\mathbf{e}}\mathbf{F}_{\mathbf{V}}^{\nu}\bar{\mathbf{L}}^{\boldsymbol{\theta}}\mathbf{F}_{\mathbf{V}}^{-\nu}\mathbf{F}_{\mathbf{V}}^{-\mathbf{e}} = \\ \mathbf{l}_{\mathbf{I}}^{\mathbf{e}} + \mathbf{F}_{\mathbf{I}}^{\mathbf{e}}\bar{\bar{\mathbf{L}}}_{\mathbf{I}}^{\mathbf{p}}\mathbf{F}_{\mathbf{I}}^{-\mathbf{e}} + \mathbf{F}_{\mathbf{I}}^{\mathbf{e}}\mathbf{F}_{\mathbf{I}}^{\mathbf{p}}\bar{\mathbf{L}}^{\boldsymbol{\theta}}\mathbf{F}_{\mathbf{I}}^{-\mathbf{p}}\mathbf{F}_{\mathbf{I}}^{-\mathbf{e}}\end{aligned} \tag{2.15}$$

where $\mathbf{l}_{\mathbf{V}}^{\mathbf{e}} = \dot{\mathbf{F}}_{\mathbf{V}}^{\mathbf{e}}\mathbf{F}_{\mathbf{V}}^{-\mathbf{e}}$ and $\mathbf{l}_{\mathbf{I}}^{\mathbf{e}} = \dot{\mathbf{F}}_{\mathbf{I}}^{\mathbf{e}}\mathbf{F}_{\mathbf{I}}^{-\mathbf{e}}$ are the viscous elastic and intermolecular elastic components of the velocity gradient in the current configuration Ω, $\tilde{\mathbf{L}}_{\mathbf{V}}^{\boldsymbol{\nu}} = \dot{\mathbf{F}}_{\mathbf{V}}^{\boldsymbol{\nu}}\mathbf{F}_{\mathbf{V}}^{-\boldsymbol{\nu}}$ is the viscous component defined in the viscous dilated relaxed configuration $\tilde{\Omega}$ and $\bar{\bar{\mathbf{L}}}_{\mathbf{I}}^{\mathbf{p}} = \dot{\mathbf{F}}_{\mathbf{I}}^{\mathbf{p}}\mathbf{F}_{\mathbf{I}}^{-\mathbf{p}}$ is the plastic component defined in the dilated relaxed configuration $\bar{\bar{\Omega}}$. Both $\tilde{\mathbf{L}}_{\mathbf{V}}^{\boldsymbol{\nu}}$ and $\bar{\bar{\mathbf{L}}}_{\mathbf{I}}^{\mathbf{p}}$ are equal to their symmetric parts since the configurations $\tilde{\Omega}$ and $\bar{\bar{\Omega}}$ are assumed to be invariant to the rigid body rotations of Ω. The thermal contribution is assumed isotropic so $\mathbf{F}^{\boldsymbol{\theta}}$ is spherical and, therefore, the skew part of $\mathbf{l}$ is zero.

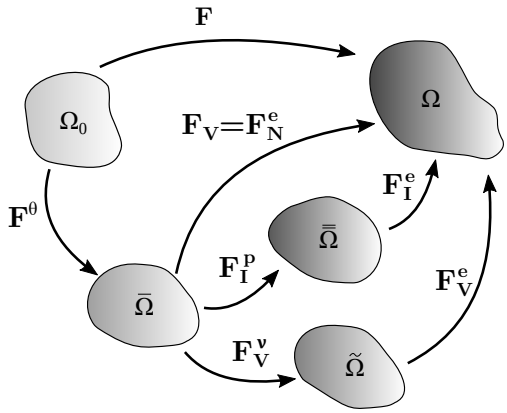

Figure 2.17 Kinematics of the Garcia-Gonzalez et al. (2018a) model.

The thermodynamic consistency is verified from the derivation of the Clausius-Duhem inequality expressed in the dilated configuration $\bar{\Omega}$ since this configuration is common to the three branches. This development permits to obtain the relationship between the stress tensor and the Helmholtz free energy function. Taking into account these considerations, the intermolecular contribution to the Cauchy stress is defined by a neo-Hookean model as

$$\boldsymbol{\sigma}_{\mathbf{I}} = \frac{\lambda_0(\theta)\ln\left(J_I^e\right)\mathbf{I}}{J_I} + \frac{\mu_0(\theta)}{J_I}\left(\mathbf{F}_{\mathbf{I}}^{\mathbf{e}}\mathbf{F}_{\mathbf{I}}^{\mathbf{e}^T} - \mathbf{I}\right) \tag{2.16}$$

where λ_0 and μ_0 are the Lamé parameters that depend linearly on temperature. The plastic contribution is activated when a yield criterion is satisfied. This criterion includes pressure and temperature dependencies. The plastic deformation is defined

by a flow equation expressed as $\bar{\bar{\mathbf{L}}}^{\mathbf{P}}_{\mathbf{I}} = \dot{\bar{\bar{\gamma}}}^{p}_{I}\bar{\bar{\mathbf{r}}}_{\mathbf{I}}$, where $\bar{\bar{\mathbf{r}}}_{\mathbf{I}}$ is the gradient of the plastic potential and $\dot{\bar{\bar{\gamma}}}^{p}_{I}$ is the viscoplastic multiplier that includes strain rate dependency.

The Cauchy stress associated with the viscous resistance is defined as

$$\boldsymbol{\sigma}_{\mathbf{V}} = \frac{C_V}{3J_V}\frac{\bar{\lambda}_{VL}}{\bar{\lambda}_V}\mathfrak{L}^{-1}\left(\frac{\bar{\lambda}_V}{\bar{\lambda}_{VL}}\right)\left(\mathbf{B}^{*}_{\mathbf{N}} - \bar{\lambda}^2\mathbf{I}\right) \tag{2.17}$$

where C_V and $\bar{\lambda}_{VL}$ are material parameters and $\bar{\lambda}_V$ is the average viscous stretch ratio. The viscoelastic flow rule is $\tilde{\mathbf{L}}^{\boldsymbol{\nu}}_{\mathbf{V}} = \dot{\bar{\gamma}}^{\nu}_{V}\tilde{\mathbf{N}}_{\mathbf{V}}$, where $\dot{\bar{\gamma}}^{\nu}_{V}$ is the viscoplastic multiplier and $\tilde{\mathbf{N}}_{\mathbf{V}}$ gives the direction of the viscoelastic flow and represents the pullback of the vector $\mathbf{N}_{\mathbf{V}}$ in the $\tilde{\Omega}$ configuration, where $\mathbf{N}_{\mathbf{V}} = \frac{\boldsymbol{\sigma}^{\mathbf{dev}}_{\mathbf{V}}}{\tau_V}$ with $\tau_V = \sqrt{tr(\boldsymbol{\sigma}^{\mathbf{dev}}_{\mathbf{V}}\boldsymbol{\sigma}^{\mathbf{dev}}_{\mathbf{V}})}$.

Finally, the hyperelastic entropic resistance is defined by a modification of the original eight-chain model as

$$\boldsymbol{\sigma}_{\mathbf{N}} = \frac{(C_R + C_\theta\,(\theta - \theta_{ref}))}{3J_N}\frac{\bar{\lambda}_L}{\bar{\lambda}}\mathfrak{L}^{-1}\left(\frac{\bar{\lambda}}{\bar{\lambda}_L}\right)\left(\mathbf{B}^{*}_{\mathbf{N}} - \bar{\lambda}^2\mathbf{I}\right) \tag{2.18}$$

where C_R is the initial elastic modulus of the network resistance, C_θ is a material parameter controlling the elastic modulus dependence on temperature and $\bar{\lambda}_L$ is the locking stretch.

Moreover, the expression for temperature evolution is obtained following the methodology previously used by Garcia-Gonzalez et al. (2017) as a function of inelastic dissipations, thermoelastic contributions, heat conduction and thermal sources.

2.3.2 FDM thermoplastic modelling

Regarding the constitutive modelling of 3D printed polymers, only a few models have been proposed in the literature. Despite the fact that polymers present large deformations, the constitutive models proposed in the literature are formulated for infinitesimal deformations. In addition, although some of them exhibit a ductile elasto-plastic response, most of the previous approaches have only considered elasticity (Ahn et al., 2003; Alaimo et al., 2017; Domingo-Espin et al., 2015; Somireddy et al., 2018; Zou et al., 2016).

Domingo-Espin et al. (2015) proposed a constitutive orthotropic model using the Hooke's law $\boldsymbol{\sigma} = \mathbb{C} : \boldsymbol{\varepsilon}$ for the prediction of FDM polycarbonate components. Due to the consideration of orthotropy with three perpendicular planes of symmetry, the elasticity tensor $\mathbb{C}$ only depends on nine components.

Zou et al. (2016) studied experimentally the mechanical performance of FDM ABS components. In addition, the generalized Hook's law was also used to predict the mechanical behaviour of FDM ABS. In that case, two modelling approaches were used:

one considering isotropic elasticity and other considering transversely isotropic elasticity. A better description of the mechanical response of FDM ABS was obtained with the transversely isotropic approach. In this model, the elastic constants of the elasticity tensor were formulated as a function of the printing angle. Moreover, assuming a linear distribution of the yielding stress, the authors proposed a mathematical expression for the prediction of the tensile strength as

$$\sigma(\theta) = \sigma(0^\circ) + \left(\frac{\sigma(90^\circ) - \sigma(0^\circ)}{90}\right)\theta \tag{2.19}$$

where $\sigma(0^\circ)$ and $\sigma(90^\circ)$ are the tensile strength for transverse and longitudinal raster orientations, and θ is an angle determining the raster orientation.

Alaimo et al. (2017) considered FDM 3D printed objects as composite laminates consisting of orthotropic laminas where each lamina corresponds to a printed layer. In the mechanical model proposed, the elastic behaviour was also modelled by Hooke's law formulated for an orthotropic material. In addition, yielding was modelled using the Tsai-Hill failure criterion, where the yielding surface is quadratic with respect to the stress components and is expressed as

$$\begin{aligned}(G+H)\sigma_{11}^2 + (F+H)\sigma_{22}^2 + (F+G)\sigma_{33}^2 - 2H\sigma_{11}\sigma_{22} - 2G\sigma_{11}\sigma_{33} - 2F\sigma_{22}\sigma_{33} \\ +2L\sigma_{23}^2 + 2M\sigma_{13}^2 + 2N\sigma_{12}^2 = 1\end{aligned} \tag{2.20}$$

where $\sigma_{ij}(i,j=1,2,3)$ are components of the Cauchy stress tensor with respect to a material vector basis that coincides with the principal axes of orthotropy and F, G, H, L, M and N coefficients are Hill's strength parameters that depend on the yielding values for ductile materials and on the ultimate failure value for brittle materials

$$\begin{aligned}
2F &= \left(\frac{1}{(\sigma_{22}^y)^2} + \frac{1}{(\sigma_{33}^y)^2} - \frac{1}{(\sigma_{11}^y)^2}\right); \qquad 2L = \frac{1}{(\sigma_{23}^y)^2} \\
2G &= \left(\frac{1}{(\sigma_{11}^y)^2} + \frac{1}{(\sigma_{33}^y)^2} - \frac{1}{(\sigma_{22}^y)^2}\right); \qquad 2M = \frac{1}{(\sigma_{13}^y)^2} \\
2H &= \left(\frac{1}{(\sigma_{11}^y)^2} + \frac{1}{(\sigma_{22}^y)^2} - \frac{1}{(\sigma_{33}^y)^2}\right); \qquad 2N = \frac{1}{(\sigma_{12}^y)^2}
\end{aligned} \tag{2.21}$$

where $\sigma_{ij}^y(i,j=1,2,3)$ are the yield stress or ultimate strength in the corresponded direction. Due to all terms are quadratic in stress, identical response is obtained in tension and compression.

Previously, Ahn et al. (2003) had been used the Classical Laminate Theory to model the response of FDM components. Tsai-Wu failure was used for the tensile strength prediction, which is generally defined as

$$F_i\sigma_i + F_{ij}\sigma_i\sigma_j = 1 \tag{2.22}$$

where $i, j = 1...6$, σ_i are the tensor stress components expressed in Voigth notation and, F_i and F_{ij} components are experimentally determined material strength parameters. For plane-stress conditions, this criterion is reduced to

$$F_1\sigma_{11} + F_2\sigma_{22} + F_{11}\sigma_{11}^2 + F_{22}\sigma_{22}^2 + F_{66}\sigma_{66}^2 + 2F_{12}\sigma_{11}\sigma_{22} = 1 \tag{2.23}$$

where the coefficients are defined as

$$\begin{aligned} F_1 &= \frac{1}{\sigma_{11}^t} - \frac{1}{\sigma_{11}^c}; \qquad F_1 = \frac{2}{\sigma_{22}^t} - \frac{1}{\sigma_{22}^c}; \qquad F_{11} = \frac{1}{\sigma_{11}^t\sigma_{11}^c} \\ F_{22} &= \frac{1}{\sigma_{22}^t\sigma_{22}^c}; \qquad F_{66} = \frac{1}{\sigma_{12}^2}; \qquad F_{12} \simeq -\frac{1}{2}(\sigma_{11}\sigma_{22})^{1/2} \end{aligned} \tag{2.24}$$

More recently, the anisotropic yield criterion proposed by Hill (1948)

$$F\left(\sigma_{22} - \sigma_{33}\right)^2 + G\left(\sigma_{33} - \sigma_{11}\right)^2 + H\left(\sigma_{11} - \sigma_{22}\right)^2 + 2L\sigma_{23}^2 + 2M\sigma_{13}^2 + 2N\sigma_{12}^2 = 1 \tag{2.25}$$

was used by Song et al. (2017) to model the ductile orthotropic plastic response of 3D printed polymers loaded in the XY plane as

$$F\sigma_{22}^2 + G\sigma_{11}^2 + H\left(\sigma_{11} - \sigma_{22}\right)^2 = 1 \tag{2.26}$$

Despite the efforts made until the date to model the mechanical behaviour of 3D printed polymers, no constitutive model accounting for the principal characteristics of both elastic and inelastic responses of such materials has been found in the literature.

2.3.3 Anisotropic and porous-based hyperelastic models

Apart from large strain response and pressure, strain rate and temperature dependencies, 3D printed thermoplastics present elastic and plastic anisotropic responses as well as porous nature due to the manufacturing process.

2.3.3.1 Anisotropic hyperelastic models

One of the most common approaches in anisotropic hyperelasticity is the use of two additional invariants, I_4 and I_5 (Spencer, 1972). The definition of these invariants is based on the assumption of a preferred fibre orientation defined by the vector $\mathbf{a}_0$. Thus, these are defined as

$$\begin{aligned} I_4 &= \mathbf{a}_0\mathbf{C}\mathbf{a}_0 = \lambda_F^2 \\ I_5 &= \mathbf{a}_0\mathbf{C}^2\mathbf{a}_0 \end{aligned} \tag{2.27}$$

where $\mathbf{C}$ is the right Cauchy-Green deformation tensor and λ_F is the stretch in the fibre direction. In this regard, some anisotropic constitutive models have been developed.

Holzapfel et al. (2000) developed a model for the prediction of the anisotropic behaviour of arterial tissue. The model is formulated based on the decomposition of the energy density function into a component for the matrix response, modelled by the neo-Hookean model, and an anisotropic component associated with up to three different families of fibres. To this end, the energy density function is defined as

$$\Psi(I_1^*, I_4^*, J) = \frac{\mu}{2}\left(I_1^* - 3\right) + \frac{k_1}{2k_2}\sum_{i=1}^{3}\left[e^{k_2 < E_i >^2} - 1\right] + \frac{k}{2}\left(J-1\right)^2 \tag{2.28}$$

where $E_i = d\left(I_1^* - 3\right) + (1-3d)\left(I_{4i}^* - 1\right)$ is the energy term, being d the dispersion, $I_4^* = \left(\mathbf{F^*a}_0\right)\left(\mathbf{F^*a}_0\right)$ and $< E_i >$ is a ramp function defined as

$$< E_i >= \frac{E_i + \mid E_i \mid}{2} \tag{2.29}$$

In this energy density function, $d = 0$ if fibres are perfectly aligned, and $d = 1/3$ if fibres are randomly oriented giving an isotropic response.

Recently, Garcia-Gonzalez et al. (2018b) have developed a continuum constitutive framework for the mechanical modelling of soft tissues that incorporates strain rate and temperature dependencies as well as the transverse isotropy arising from fibres embedded into a soft matrix. In this framework, the Helmholtz free energy function per unit volume in the reference configuration Ω_0 is decoupled into matrix and fibres contributions $\Psi_0 = \Psi_{0M} + \Psi_{0F}$. In this model, the fourth strain invariant is included to model the anisotropic contribution as proposed by Gasser et al. (2006)

$$\Psi_{0F}(\mathbf{C_F^e}, \mathbf{A}_0, \theta) = \begin{cases} \dfrac{k_1(\theta)}{2k_2}\left\{\exp\left[k_2\left(I_{4F}^* - 1\right)^2\right] - 1\right\} & \text{if } I_{4F}^* \leq 0 \\ 0 & otherwise \end{cases} \tag{2.30}$$

2.3.3.2 Porous hyperelastic models

Regarding the modelling of porous polymers, Blatz and Ko (1962) proposed a phenomenological model for porous elastomers motivated by an experimental work on polyurethane foam rubber with an approximate volume fraction of 50% and 40 μm in diameter. Due to the presence of porous, these materials are compressible. Therefore the generalized Blatz-Ko material is described as a function of invariants I_1, I_2, I_3 as

$$\Psi\left(I_1, I_2, I_3\right) = \frac{\mu f_0}{2}\left(I_1 - 1 - \frac{1}{\nu} + \frac{1-2\nu}{\nu} I_3^{-\frac{\nu}{1-2\nu}}\right) + \frac{\mu}{2}(f_0 - 1)\left(\frac{I_2}{I_3} - 1 - \frac{1}{\nu} + \frac{1-2\nu}{\nu} I_3^{\frac{\nu}{1-2\nu}}\right) \tag{2.31}$$

where μ and ν are the shear modulus and Poisson's ratio, and $f_0 \in [0, 1]$ is a constant related to the volume fraction of voids.

In the same way, other authors have proposed constitutive models for porous materials. Lopez-Pamies and Castañeda (2007) provided a homogenization-based constitutive model for a random and isotropic distribution of initially spherical porous in rubbers. In addition, Guo et al. (2008) developed a hyperelastic constitutive model for porous materials with aligned continuous cylindrical pores that is presented below.

- **Guo et al. (2008) model**

  Guo et al. (2008) developed a hyperelastic constitutive model for neo-Hookean composites with aligned continuous cylindrical pores (see Figure 2.18). Although the matrix is incompressible, these materials present a compressible transversely isotropic behaviour due to the existence of voids. The deformation gradient is decomposed multiplicatively into three parts: an isochoric uniaxial deformation along the preferred direction (direction of the cylindrical voids in the undeformed configuration), an equi-biaxial deformation on the transverse plane (introduced to archive the desired volume change), and a subsequent shear deformation (which is further decomposed into an along-fibre and transverse shear deformation).

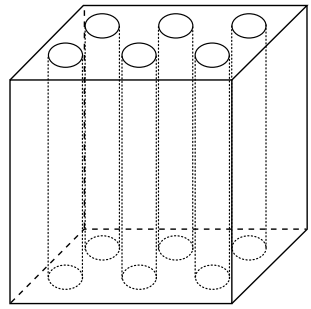

Figure 2.18 Composite with aligned continuous cylindrical pores, adapted from Guo et al. (2008).

  The coordinate system is chosen so that $\boldsymbol{e_1}$ is aligned with the preferred direction, $\boldsymbol{e_2}$ is perpendicular to $\boldsymbol{e_1}$ and $\boldsymbol{e_3}$ is determined by the right-hand rule as $\boldsymbol{e_3} = \boldsymbol{e_1} \times \boldsymbol{e_2}$. Applying a general deformation gradient $\mathbf{F}$, the rotation tensor $\mathbf{R}_1$ rotates the deformed preferred direction $\mathbf{F}\mathbf{a}_0$ to the original direction, while $\mathbf{R}_2$ rotates the deformed $\boldsymbol{e_2}$ vector $\mathbf{R}_1\mathbf{F}\boldsymbol{e_2}$ back to the original plane $\boldsymbol{e_1} - \boldsymbol{e_2}$. Then, the new equivalent deformation gradient tensor obtained is $\mathbf{F}^* = \mathbf{R}_2\mathbf{R}_1\mathbf{F}$. Nevertheless, since $\mathbf{R}_1$ and $\mathbf{R}_2$ are both rigid body rotation tensors, the deformation represented by $\mathbf{F}$ is essentially identical to $\mathbf{F}^*$. Therefore, the deformation gradient $\mathbf{F}^*$ is defined as

$$\mathbf{F}^* = \mathbf{F}^*_\mathbf{s}\mathbf{F}^*_\mathbf{b}\mathbf{F}^*_\mathbf{p} \begin{bmatrix} \lambda_F & F^*_{12} & F^*_{13} \\ 0 & \sqrt{\frac{J}{\lambda_F}} & F^*_{23} \\ 0 & 0 & \sqrt{\frac{J}{\lambda_F}} \end{bmatrix} \tag{2.32}$$

where $\mathbf{F}^*_\mathbf{p}$ is the isochoric uniaxial deformation along the preferred direction, $\mathbf{F}^*_\mathbf{b}$ the equi-biaxial deformation and $\mathbf{F}^*_\mathbf{s}$ the shear deformation (see Figure 2.19). Both the isochoric uniaxial deformation along the preferred direction $\mathbf{F}^*_\mathbf{p}$ and the equi-biaxial deformation $\mathbf{F}^*_\mathbf{b}$ are diagonal matrices that are defined as

$$\begin{aligned} \mathbf{F}^*_\mathbf{p} &= diag\begin{bmatrix} \lambda_F & \lambda_F^{-1/2} & \lambda_F^{-1/2} \end{bmatrix} \\ \mathbf{F}^*_\mathbf{b} &= diag\begin{bmatrix} 1 & \sqrt{J} & \sqrt{J} \end{bmatrix} \end{aligned} \tag{2.33}$$

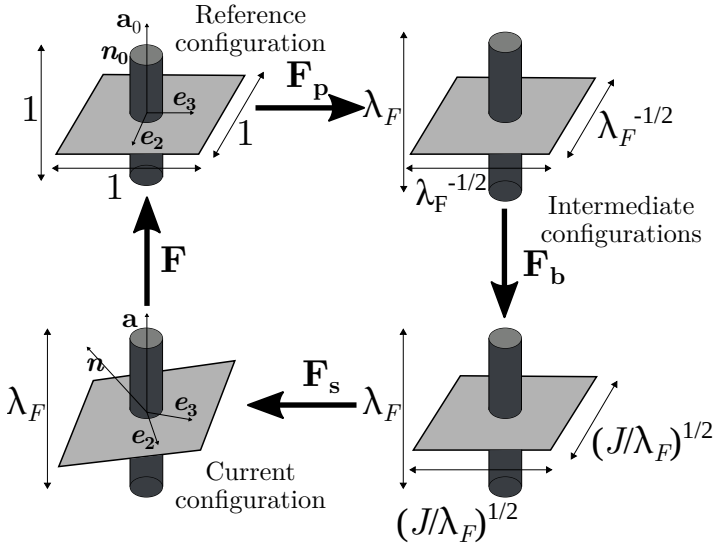

Figure 2.19 Multiplicative decomposition of the deformation gradient, adapted from Guo et al. (2008).

Based on this multiplicative decomposition of the deformation gradient and the cylindrical composite element model, the strain energy neo-Hookean function Equation (2.5) can be transformed as

$$\begin{aligned} \Psi(I_1, I_3, I_4) = \Psi_p + \Psi_b + \Psi_s = \frac{\mu_m v_m}{2}\left(I_4 + 2I_4^{-1/2} - 3\right) \\ + \frac{\mu_m}{2}(J-1)I_4^{-1/2}\ln\left(\frac{J - v_m}{Jv_f}\right) + \frac{\mu_m v_m}{2(1+vf)}\left(I_1 - I_4 - 2\sqrt{\frac{I_3}{I_4}}\right) \end{aligned} \tag{2.34}$$

where v_m and v_f are the initial volume fractions of the matrix and the voids ($v_m + v_f = 1$), respectively, μ_m is the shear modulus of the matrix and I_1, I_3 and I_4 the first, third and fourth invariants.

2.3.3.3 Yield criteria and flow rules for porous material

Classic theories assume plastic incompressibility and no effect on the yield of the hydrostatic stress. However, theories describing porous materials suggest that the hydrostatic component of stress can cause macroscopic dilatation and affect plastic yield. In this regard, Gurson (1977) developed a yield function for porous materials based on an upper bound approach, where the matrix is idealized as incompressible and as a rigid perfectly plastic obeying a von Mises criterion. The solution is presented for two different void geometries: long circular cylinder and sphere. Thus, the yield function considering a cylindrical cell with a circular cylinder void is given by

$$f = \frac{{\sigma_{eqv}}^2}{{\sigma_0}^2} + 2f\cosh\left(\frac{\sqrt{3}}{2}\frac{\sigma_{kk}}{\sigma_0}\right) - (1 + f^2) = 0 \tag{2.35}$$

where f is the void volume fraction, σ_{eqv} is the macroscopic equivalent stress, σ_0 is the microscopic equivalent tensile yield stress and σ_{kk} is the macroscopic dilatational stress in the transverse plane. Note that if f is zero, the yield function takes the von Mises yield function. Moreover, the plastic flow follows an associated flow rule defined as

$$d\boldsymbol{\epsilon_p} = d\gamma\frac{\partial f}{\partial \boldsymbol{\sigma}} \tag{2.36}$$

Later, Gurson's model was modified by Tvergaard (1981, 1987) and Tvergaard and Needleman (1984) by introducing two scalar parameters (q_1 and q_2) as

$$f = \frac{{\sigma_{eqv}}^2}{{\sigma_0}^2} + 2f^* q_1\cosh\left(q_2\frac{\sqrt{3}}{2}\frac{\sigma_{kk}}{\sigma_0}\right) - (1 + (q_1 f^*)^2) = 0 \tag{2.37}$$

3 Experimental characterisation and analytical modelling of FDM thermoplastics

This chapter investigates the influence of the printing parameters on the mesostructure and mechanical performance of FDM components. In the previous chapter, we have seen that several authors have studied the influence of printing parameters on both structural and mechanical properties of 3D printed polymers. However, there is still an absence of studies that allow for finding a relationship between mechanical properties and the mesostructure resulting from the manufacturing process. In this chapter, an experimental characterisation in terms of mesostructure and mechanical performance is developed. The influence of layer height and raster orientation, two of the most relevant printing parameters, as well as the number of layers that composes the sample is studied. To this end, the outline of the chapter is as follows: Section 3.1 provides the details of material and manufacturing process of the specimens; in Section 3.2, a characterisation of the mesostructure is developed by analysing the cross-sectional area, comparing the main differences in terms of void density and cross-sectional geometry; in Section 3.3, a complete mechanical characterisation is undertaken to determine the key deformation and failure mechanisms governing the deformation process during tensile tests at different strain rate conditions. Based on the experimental results, analytical expressions are proposed for the prediction of the void density and the resulting mechanical properties in Sections 3.4 and 3.5, respectively. Finally, the conclusions of the chapter are presented in Section 3.6.

3.1 Material and processing

The aim of this chapter is to study the correlation between printing parameters and the mesostructure and mechanical properties of FDM polymeric components. To this end, both mesostructural and mechanical characterisation are conducted on specimens made of ABS, one of the most common materials used for FDM (Wang et al., 2017).

The first step is the definition of the geometry of the specimens. ASTM D638-14 (2014) and ISO 527-1 (2012) standards, which are technically equivalent test methods, define the methods to determine the tensile properties of polymers. Both standards recommend the use of a dog-bone geometry to ensure that the material breaks in the narrow section and, therefore, the failure is not affected by the grips. However, as previously observed by other authors (Letcher et al., 2015; Rankouhi et al., 2016), dog-bone geometry causes premature failure due to stress concentration in the radius of the fillet in 3D printed samples. To alleviate this issue, thin rectangular specimens with a size of 164 mm × 50 mm are used instead. Different combinations of number of layers and layer height are used. Therefore, the thickness of the specimens is defined by these parameters.

A Hephestos 2 bq 3D printer with a heated bed is used to manufacture all the specimens (BQ, 2019). Its extruder has a nozzle with a diameter of 0.4 mm and is fed by filament with a diameter of 1.75 mm. This 3D printer permits the manufacturing of FDM components with a maximum extrusion temperature of 250 °C. The ABS filament is supplied by Smart Materials 3D (Smart materials 3D, 2019) in the form of filament spool. Moreover, Ultimaker Cura (Ultimaker Cura, 2019) is used as a slicer software to prepare all the G-codes files.

3D printing permits to control a huge number of parameters. In this thesis, three different layer heights (0.1, 0.2 and 0.3 mm), two rasters orientations (longitudinal and transverse) and different number of layers (these will be specific for each experimental characterisation) are considered. The layer heights correspond to the 25%, 50% and 75% of the nozzle's diameter, within the range recommended for a good printing quality. In addition, all the specimens are made with unidirectional layers, which is contrary to the normal practice of alternate layers perpendicular to each other. This is done to have a better control over the effects of the parameters studied. The remaining parameters are held at the recommended or default values, see Table 3.1.

Table 3.1 Printing parameters used for the manufacturing of the ABS specimens used in experimental characterisations.

Printing parameter	Value
Infill density	100%
Line width	0.4 mm
Air gap	0 mm
Infill pattern	Lines
Extrusion temperature	240 °C
Build plate temperature	100 °C

Moreover, only a single contour is deposited along the component edge in all the specimens, with a width of 0.1 mm. This configuration is chosen to avoid the influence of the contours on the mechanical properties. In this regard, Croccolo et al. (2013)

developed an experimental study where an increase in the tensile stiffness and strength properties of up to 16.8% and 24.3% were observed, respectively, when the number of contours increases from 1 to 10.

Finally, each sample is printed individually at the exact same position on the 3D printer platform to avoid differences associated with thermal gradients (Sun et al., 2008).

3.2 Mesostructural characterisation

The final mesostructure and void density of FDM specimens are strongly influenced by the printing parameters. In order to study their influence, an analysis of ABS samples, manufactured with different printing parameters, is performed by means of micrographs of the cross-section using a Scanning Electron Microscope (SEM). Two sets of specimens are used:

- The first group consists of two-layer specimens. These specimens are manufactured with two different layer heights (0.2 and 0.3 mm) and two raster orientations (longitudinal and transversal). Due to the length of the specimen is greater than the width, different temperature distributions within the filaments that compose the components is expected. In this regard, the filament temperature is higher when an adjacent filament is deposited for transverse specimens than for longitudinal due to the path that the extruder has to do is shorter. This can lead to differences in the development of the bond between filaments. Therefore, the main objective of this study is to understand the influence of the raster orientation in the mesostructure.

- The second group consists of specimens with a specific total thickness. Two total thicknesses are used: 1.2 mm and 1.8 mm. These specimens are manufactured with three different layer heights (0.1, 0.2 and 0.3 mm) and a longitudinal raster orientation. Some studies have shown that the void density in the lower region of the part is smaller than in the upper region due to differences in the temperature profile (Sun et al., 2008). This observation indicates that the bond formed between filaments is larger in the first layers. Therefore, the main objective of this analysis is to determine the influence of the number of layers.

Moreover, the influence of the layer height in the mesostructure is analysed in both sets. The different configurations tested are summarised in Table 3.2.

Table 3.2 Configuration of samples employed for the mesostructural characterisation.

	Raster orientation	Layer height		
		0.1 mm	0.2 mm	0.3 mm
Two-layer specimens	Longitudinal		✓	✓
	Transversal		✓	✓
1.2 mm thickness	Longitudinal	✓	✓	✓
1.8 mm thickness	Longitudinal		✓	✓

3.2.1 Experimental setup

Test samples of dimensions 13 mm × 13 mm are cut from the middle of the specimens. After the cut, the samples are sanded using 1200 grit silicon carbide paper and polished with 9 μm diamond paste. Micrographs of the cross-sections are taken using a SEM.

A SEM is an electron microscope that uses a focused beam of electrons to create a magnified image of a sample (MyScope, 2019). The electron beam is scanned following a regular pattern across the surface of the sample of interest (MyScope, 2019). The electrons in the beam interact with atoms in the sample, producing signals giving information about the surface topography and composition of the material. The samples need to be electrically conductive to form the image. Therefore, non-conductive samples need to be coated with a thin layer of metal, such as gold, or carbon. On the other hand, it is possible to obtain images of a non-conductive sample, without the need for coating, operating under low vacuum operational mode. This mode allows to leak into the chamber a small amount of air that is ionized forming a cloud of positive charge around the sample (MyScope, 2019).

Due to ABS is a non-conductive material, the micrographs are obtained operating under low vacuum mode.

3.2.1.1 Postprocessing of micrographs

Once the micrographs are ready, *Image J software* is used to measure the void density. This is a public domain Java image processing and analysis program used to analyse, process and edit images (ImageJ, 2019). Among the huge number of operations that this software allows to apply over the initial image, it can calculate areas and measure distances of user-defined selections. In this regard, 'Analyze particles' command counts and measures objects in binary or thresholded images over the selected area (ImageJ, 2019). Therefore, it is necessary to previously transform the images obtained from the microscope into a thresholded image. The 'Threshold' tool permits to divide a greyscale image into two classes of pixels, obtained the area of interest and background. For that, it is necessary to set the lower and upper threshold values. However, due to the similar colour of the voids and filaments, in some images, the threshold tool is not able

to segment the image correctly. Therefore, the images need to be manually processed before segmentation, defining the area of each void and filling it with background colour, see Figure 3.1.

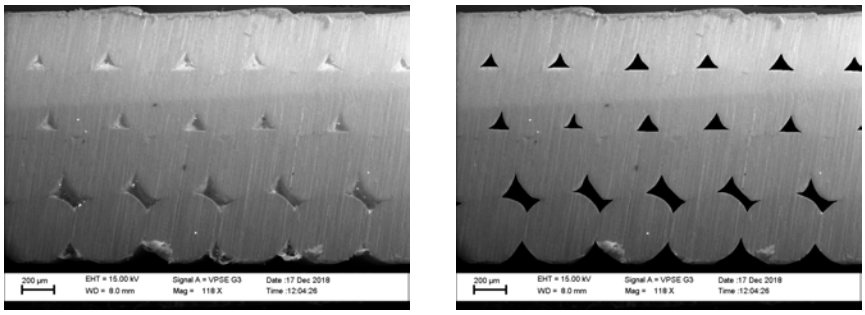

(a) *(b)*

Figure 3.1 Digital image processing using Image J to define the area of interest and background: (a) raw image; (b) processed image.

Once the image is ready, the total area of voids can be measured using 'Analyze particles' tool. Before using this command, it is necessary to set a known scale. To this end, we draw a line, using the straight-line selection tool, over the scale obtained from the micrograph and introduce the value of the known distance as is shown in Figure 3.2.

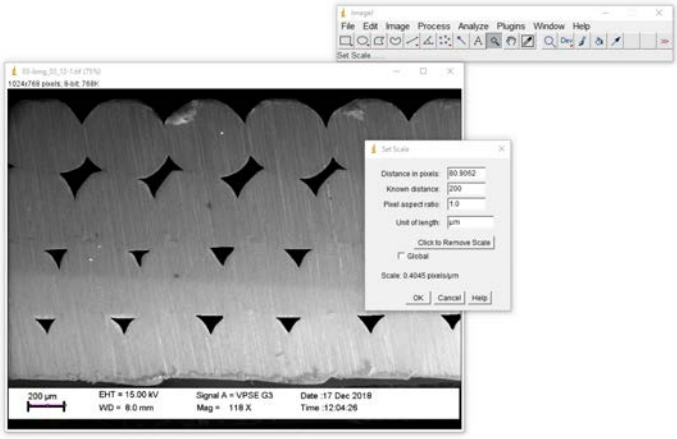

Figure 3.2 Step 1: Set scale.

Then, we select the area of interest and duplicate it. Lastly, we can transform the image into binary using the 'Threshold' tool. In this way, the raw grey-scale image is segmented into voids and the real area of material, see Figure 3.3.

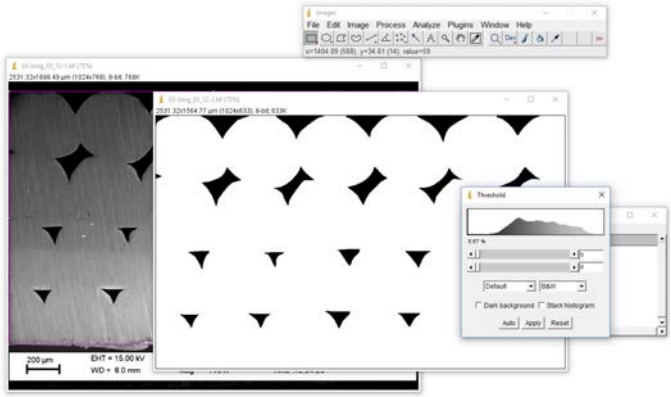

Figure 3.3 Step 3: Threshold.

Finally, 'Analyze particles' tool finds the voids and measures their area, see Figure 3.4. It works by scanning the image or selection until finding the edge of an object. Since the filaments length is the same as the voids length, the void density, measured as the total area of voids into the cross-sectional area, is equivalent to porosity.

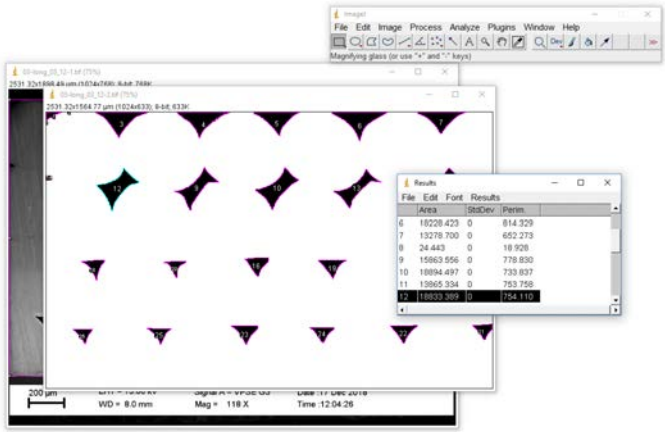

Figure 3.4 Step 4: Analyze particles.

3.2.2 Results and discussion

The results obtained in terms of void density of the first set of samples are presented in Table 3.3. The results show that the void density increases with the layer height. Comparing the void density for the two raster orientation, the void density of transverse specimens is greater. These results are contrary to the expected since the path of the extruder is shorter for the transverse specimen and, therefore, higher temperature filament profiles are expected which can lead to the development of large neck of the bond

between filaments. However, transverse specimens are not completely aligned due to manufacturing defects, see Figure 3.5. This skewed mesostructure causes the appearance of small voids at the contact point between the top and bottom filaments leading to a slight increase in void density. Therefore, the percentage of voids expected will be approximately the same independently of the raster orientation for the geometry used in this study.

Table 3.3 Void density of two-layer specimens.

Raster orientation	Layer height	
	0.2 mm	0.3 mm
Longitudinal	2.07%	4.75%
Transversal	3.24%	6.12%

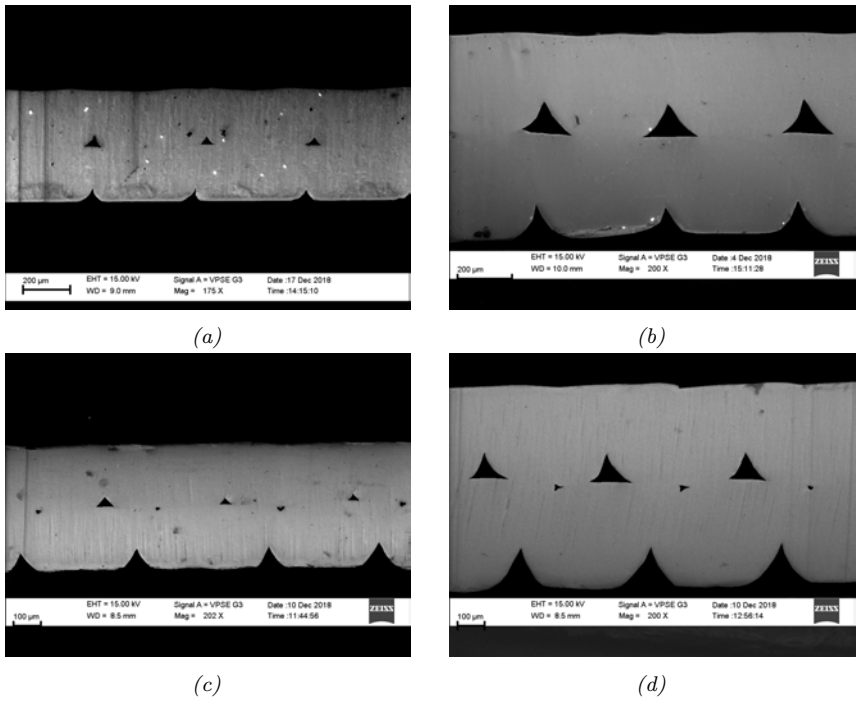

(a) *(b)* *(c)* *(d)*

Figure 3.5 Microphotograph of the cross-sectional area of two layers specimens: (a) longitudinal with layer heights of 0.2 mm and (b) 0.3 mm; (c) transversal with layer heights of 0.2 mm and (d) 0.3mm.

On the other hand, Table 3.4 presents the results for specimens with thicknesses of 1.2 mm and 1.8 mm. Comparing the void density of the first ones, the higher void density is reached with a layer height of 0.2 mm. However, the bottom layers of these specimens present defects or no bonding at the sides, see Figure 3.6. These defects have

been observed by other authors and are thought to be due to problems associated with the 3D printer levelling, between the support and the extrusion head (Rodriguez et al., 2000). Therefore, a second measurement is made excluding approximately 0.4 mm of the bottom thickness of the specimens, to avoid defects due to possible errors in the levelling. The new results are shown in Table 3.4 with an asterisk, where a decrease is observed in the void density for all the layer height, being the decrease of the specimen with a layer height of 0.2 mm the most relevant (from 8.67% to 2.49%). Moreover, comparing results of the two-layer specimens to the specimens with a thickness of 1.2 mm, the values of void density are similar for each layer height.

Table 3.4 Void density of longitudinal specimens with more than two layers of material.

Specimen thickness	Layer height		
	0.1 mm	0.2 mm	0.3 mm
1.2 mm	1.89%	8.67%	5.67%
	1.1%*	2.49%*	4.14%*
1.8 mm		0.59%	8.32%

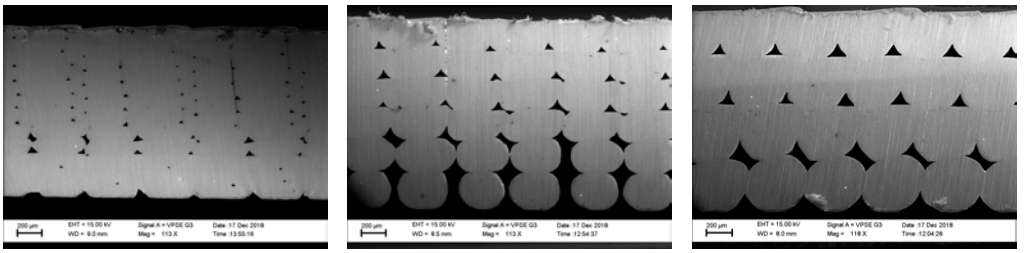

(a) *(b)* *(c)*

Figure 3.6 Microphotograph of the cross-sectional area of specimens with a total thickness of 1.2 mm: (a) layer height of 0.1 mm, (b) 0.2 mm and (c) 0.3 mm.

The results for the specimens with a thickness of 1.8 mm are also analysed. Observing the micrographs shown in Figure 3.7, it can be observed that the neck of the bond at the top is smaller than the bottom layers. This effect has been observed by other authors and is associated with differences in temperature between the top and the bottom (Sun et al., 2008). Moreover, the results are in agreement with the values obtained by other authors. Rankouhi et al. (2016), measured the void density of ABS specimen with a thickness of 2 mm and manufactured with two different layer heights. While a ratio of 0.3% was obtained with a 0.2 mm layer height, this value increased up to 5.26% with a 0.4 layer height.

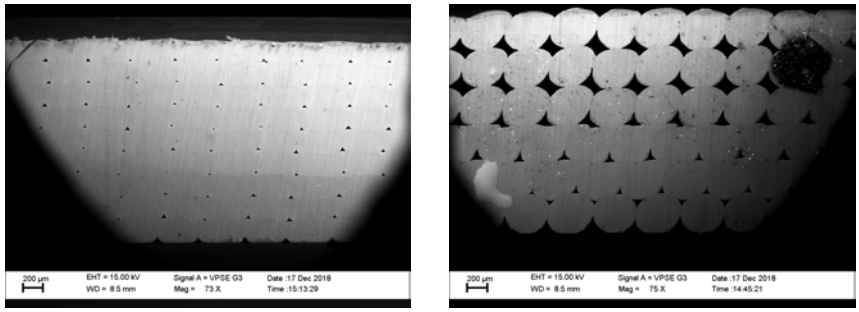

(a) *(b)*

Figure 3.7 Microphotograph of the cross-sectional area of specimens with a total thickness of 1.8 mm: (a) layer height of 0.2 mm and (b) 0.3 mm.

Finally, from the results of this structural characterisation, it can be concluded that the void density is highly influenced by geometrical printing parameters such as the layer height more than the raster orientation.

3.3 Mechanical characterisation

The mechanical behaviour of components manufactured by FDM is determined by the material and printing parameters. In this section, the influence of layer height (0.1, 0.2 and 0.3 mm), raster orientation (longitudinal and transversal) and number of layers (from one to three) on the mechanical behaviour of FDM ABS components is studied by means of mechanical properties (Young's modulus, yield strength), stress-strain response and failure mechanisms. The combinations of the three parameters give a total of eighteen different specimen-type groups. Tensile tests are conducted under quasi-static conditions at two loading rates of 1 mm/min and 10 mm/min. Moreover, a load-unload tensile test is carried out to analyse the hysteresis and viscoelastic-viscoplastic response of FDM ABS components.

3.3.1 Experimental setup

A universal machine Servosis ME 401/1 with a 10 kN load cell is used to perform the tensile tests. Due to the particular shape and size of the specimens, a new device for holding the test specimen is designed. This device, composed of two grips, is designed specifically for flat specimens and tensile loads, Figure 3.8. The planes of the grips can be found in Appendix B. The upper grip is fixed to the crosshead while the inferior is the movable member is driven by the hydraulic system. Moreover, in order to minimize both slippage and uneven stress distribution, a serrated surface is used in both grips.

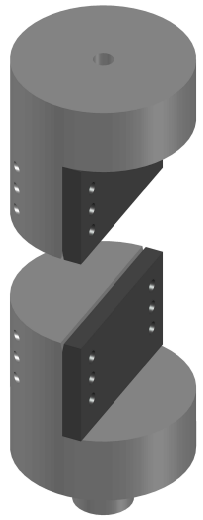

Figure 3.8 Tensile grips.

The samples are manually clamped by a maximum of six screws per grip. Due to the clamping is applied manually, it is so important to ensure the same screwing force in each screw to avoid a non-uniform distribution of the load. Therefore, a dynamometer key is employed to ensure the same screwing force in each screw. Furthermore, due to the small thickness of the specimens, loading tabs are bonded to the specimens to avoid squashing or premature fracture at the jaws. Tabs with dimensions of 50 mm $\times$ 50 mm and manufactured by 3D printing, with one layer of material and a layer height of 0.3 mm, are used. These tabs are cut in the area near the grips to obtain a better load distribution, as shown in Figure 3.9. A common glue stick is used to bond the tabs to the specimen.

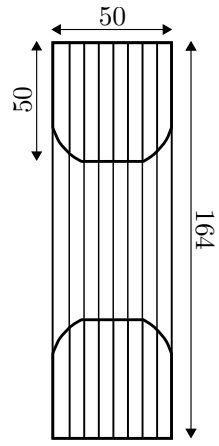

Figure 3.9 Specimen and tabs dimensions (mm).

Two loading rates of 1 mm/min and 10 mm/min (corresponding to a strain rate of $3 \cdot 10^{-4} s^{-1}$ and $3 \cdot 10^{-3} s^{-1}$) are used to analyse the influence of strain rate on mechanical properties. Finally, to ensure repeatability, four samples are used for each testing condition.

3.3.2 Results and discussion

3.3.2.1 Mechanical dependencies and stress-strain response

The results in terms of Young's modulus and maximum stress are shown in Tables 3.5 and 3.6. The maximum stress corresponds to the yield stress for longitudinal specimens and to the ultimate tensile strength for transversal specimens. These results are obtained considering the apparent cross-section and neglecting the voids.

Table 3.5 Mechanical properties of specimens with a longitudinal and transversal raster orientations at a strain rate of $3 \cdot 10^{-4} s^{-1}$.

Specimen		Longitudinal				Transversal			
Number of layers	Layer height (mm)	Elastic modulus (MPa)		Maximum stress (MPa)		Elastic modulus (MPa)		Maximum stress (MPa)	
		Mean	SD	Mean	SD	Mean	SD	Mean	SD
1	0.1	2229.1	41.4	45.3	0.8	2104.9	54.1	18.6	1.6
	0.2	2088.1	26.6	38.9	0.2	1965.6	18.4	15.7	2.3
	0.3	1966.5	39.4	38.1	0.3	1629.2	35.0	18.5	0.8
2	0.1	2056.5	85.3	43.6	0.3	1984.7	59.9	20.2	2.7
	0.2	1874.5	17.1	38.8	0.3	1765.5	64.3	17.9	0.2
	0.3	1821.3	22.9	38.0	0.7	1554.5	45.2	19.6	1.9
3	0.1	1866.0	51.7	42.2	0.1	1974.0	30.3	23.2	3.9
	0.2	1793.7	31.7	38.0	0.4	1806.2	29.0	22.2	0.7
	0.3	1802.7	40.5	36.6	0.1	1556.4	41.2	20.1	0.3

Table 3.6 Mechanical properties of specimens with a longitudinal and transversal raster orientations at a strain rate of $3 \cdot 10^{-3} s^{-1}$.

Specimen		Longitudinal				Transversal			
Number of layers	Layer height (mm)	Elastic modulus (MPa)		Maximum stress (MPa)		Elastic modulus (MPa)		Maximum stress (MPa)	
		Mean	SD	Mean	SD	Mean	SD	Mean	SD
1	0.1	2317.6	54.7	48.9	0.6	2017.8	19.4	23.0	0.9
	0.2	2063.2	14.0	43.3	0.3	1916.4	40.3	16.4	1.3
	0.3	2012.2	21.3	40.8	0.4	1629.9	15.8	22.8	0.1
2	0.1	2098.0	39.0	45.2	0.6	2039.1	56.4	21.2	5.5
	0.2	1971.6	26.0	42.3	0.4	1865.3	56.4	20.4	1.2
	0.3	1918.3	44.6	41.1	0.3	1645.8	60.4	20.1	2.0
3	0.1	1880.9	97.6	45.6	0.5	1983.8	39.6	28.4	2.2
	0.2	1921.8	13.8	41.9	0.2	1872.5	38.3	22.9	0.8
	0.3	1922.7	65.8	39.4	0.7	1621.1	22.1	23.5	0.6

The values of standard deviation show good repeatability in the results. However, some scatter is observed in the maximum stress for transverse specimens. These values correspond with the ultimate tensile strength, which is highly influenced by the defects of the components.

The effect of the strain rate is studied at $3 \cdot 10^{-4} s^{-1}$ and $3 \cdot 10^{-3} s^{-1}$. A slight increase, by up to 7%, is observed in the Young's modulus as strain rate increases. Moreover, a more noticeable increase in the yield stress is observed reaching by up to 11% for longitudinal specimens and by up to 24% for transversal. On the other hand, comparing the mechanical response for both raster orientations, higher Young's modulus and maximum stress are observed for longitudinal specimens. In this regard, the Young's modulus and maximum stress decrease by up to 18% and 60%, respectively, for a transversal raster. These tendencies are in accordance with the previous studies found in the literature (Rodríguez et al., 2001; Song et al., 2017; Vairis et al., 2016). The influence of strain rate and raster orientation can be also observed in Figure 3.10, where the stress-strain response of specimens with a layer height of 0.1 mm is compared.

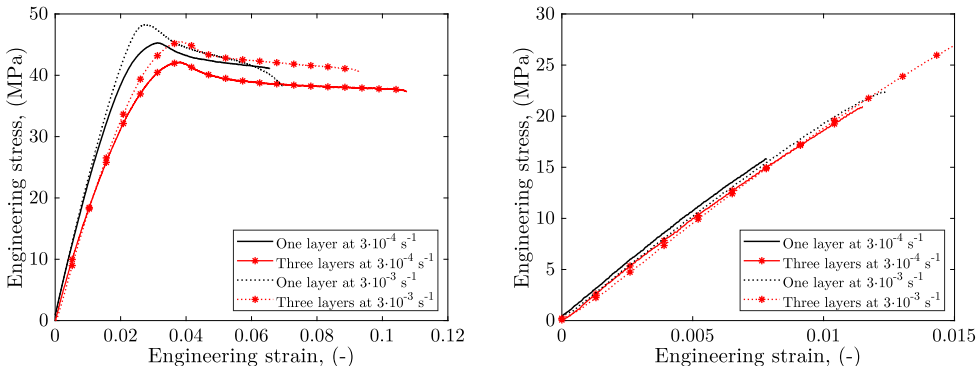

Figure 3.10 Comparison of stress-strain response of 0.1 mm FDM ABS specimens: (a) longitudinal and (b) transversal orientations.

The dependence with the layer height for both strain rates shows that the Young's modulus and maximum stress decrease by up to 11% and 14%, respectively, being this effect more significant when the layer height decreases from 0.1 mm to 0.2 mm than from 0.2 to 0.3 mm, see Figure 3.11a. These differences increase by up to 18% and 40% for transversal specimens. These tendencies are explained by the previous results shown in Table 3.4, where an increase in void density is observed with layer height. In the same way, the Young's modulus and maximum stress decrease by up to 10% and 7% when a new layer is added, for longitudinal specimens, see Figure 3.11b. On the contrary, the maximum stress increases by up to 34% when the number of layers increases for transversal specimens. These differences in mechanical response are explained by the

fact that when the number of layers increases, so does the number of bonding interfaces. In this regard, a steady limit is expected for a given number of layers, from which the mechanical response would not be altered. The definition of such limit needs of further studies and is out of the scope of this work.

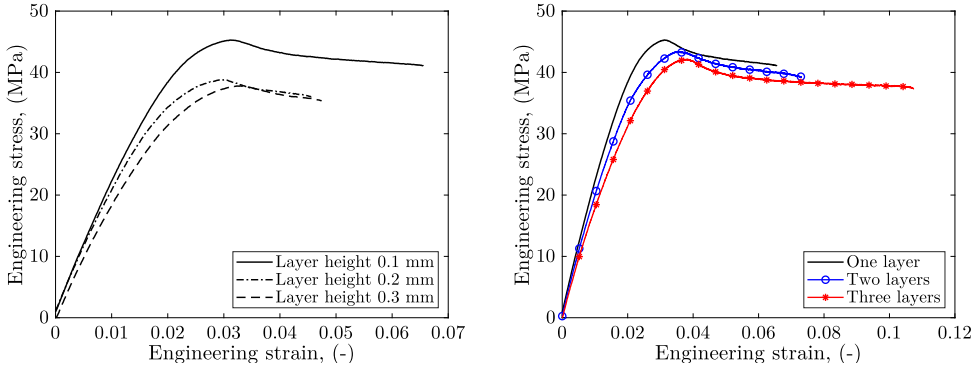

Figure 3.11 Comparison of stress-strain response of longitudinal FDM ABS specimens at a strain rate of $3 \cdot 10^{-4} s^{-1}$: (a) one layer and three different layer height and (b) 0.1 mm layer height and three different number of layers.

In addition, comparing results of specimens with the same thickness (i.e., one-0.3 mm-layer specimens vs. three-0.1 mm-layer specimens or two-0.3 mm-layer specimens vs. three-0.2 mm-layer specimens), better mechanical performance is obtained with a smaller layer height due to lower porosity as is shown in Figure 3.12. However, similar mechanical properties are obtained for the case of specimens with a total thickness of 0.6 mm and a longitudinal raster orientation, as shown in Figure 3.12b.

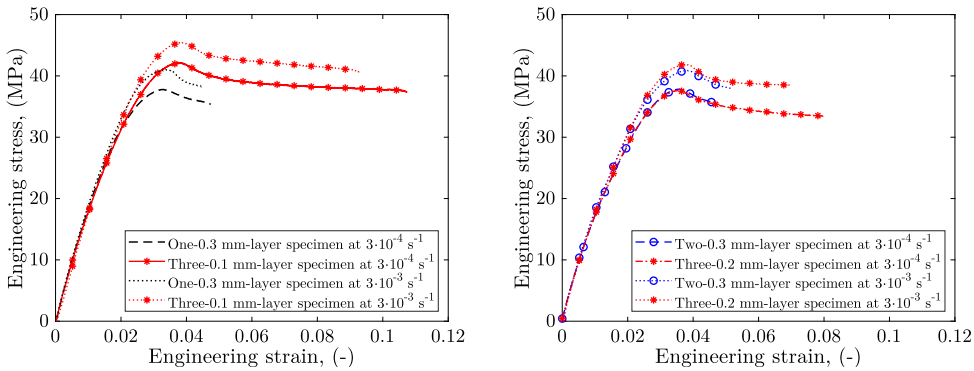

Figure 3.12 Comparison of stress-strain response of longitudinal FDM ABS specimens with the same total thickness: (a) total thickness of 0.3 mm and (b) total thickness of 0.6 mm.

Finally, the load-unload tensile behaviour carried out on one-0.1 mm-layer longitudinal specimen is shown in Figure 3.13. This test is conducted at a loading rate of 1 mm/min ($3{\cdot}10^{-4}s^{-1}$). During loading, an initial elastic and linear region (1) followed by a non-linear region until yielding (2) and a strain softening region (3) are observed. The viscous nature of the FDM ABS is determined by the response during unloading (4), where the unloading follows a different path than the loading showing hysteresis. Moreover, such viscous mechanisms are also present at different strain rates, providing a hardening associated with strain rate dependency. Permanent deformation is observed after complete unloading, indicating a major role played by viscoplastic mechanisms during the deformation process.

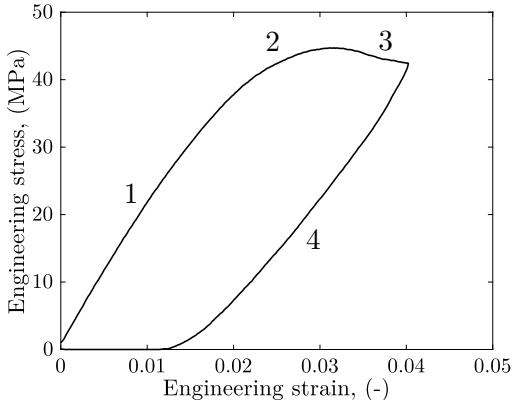

Figure 3.13 Load-unload tensile test on a one-0.1 mm-layer longitudinal specimen at a strain rate of $3 \cdot 10^{-4}s^{-1}$.

3.3.2.2 Deformation and failure mechanisms

As for mechanical properties such as Young's modulus and maximum stress, the deformation mechanisms and failure modes observed during deformation and fracture also depend on the printing parameters, especially on the raster orientations. Longitudinal specimens present an elastic linear region followed by necking and, finally, a plastic flow at constant stress. During the deformation process of longitudinal specimens, shear zones appear on each filament and propagate obliquely before yielding. In addition, crazes formation and growth are observed. Crazing develops when excessive stress is applied to a polymer, leading to microvoid formation normal to the load direction (Greenhalgh, 2009), see Figure 3.14. These crazing and shear banding continue propagating along the whole gauge length. From the microvoids, cracks start to propagate slowly at first but rapidly when the cross-section is reduced. Finally, the fracture occurs normal to the load direction and in stress whitened areas (see Figure 3.14). The fracture surface is analysed with an optical microscope, where micro-shearing is observed on each filament, see Figures 3.15a and 3.15b.

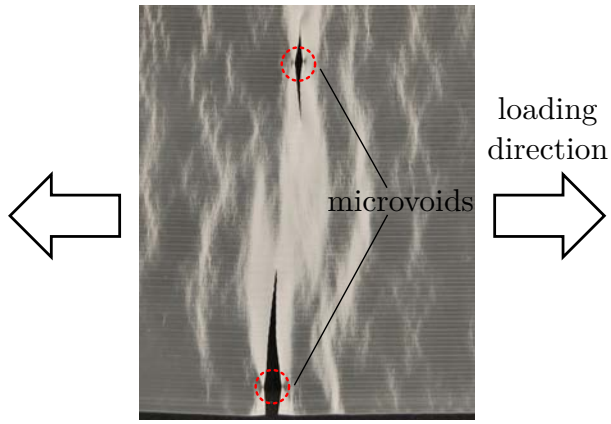

Figure 3.14 Shear bands and crazing on a longitudinal one-0.1mm-layer specimen tested at a strain rate of $3 \cdot 10^{-4} s^{-1}$.

On the other hand, transverse specimens exhibit an elastic linear behaviour with a brittle fracture. This fracture occurs along the filament-to-filament interface as shown by comparing Figures 3.15c and 3.15d. This is explained by the fact that, in transverse specimens, the loads are taken by the bond between filaments and not by the filaments themselves.

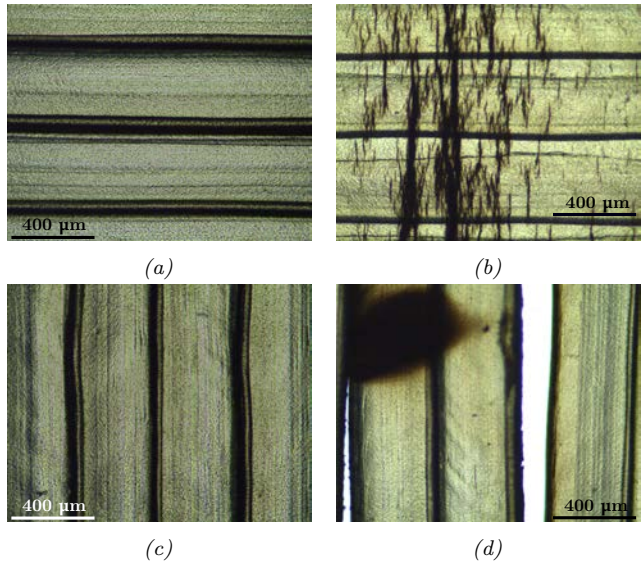

(a) *(b)*

(c) *(d)*

Figure 3.15 Microphotograph of surface of a one-0.1 mm-layer specimen tested at a strain rate of $3 \cdot 10^{-4} s^{-1}$*: (a) longitudinal before testing and (b) after testing; (c) transversal before testing and (d) after testing.*

3.4 Analytical modelling for void density

3.4.1 Modelling formulation

From the results of the mesotructural characterisation, it can be concluded that FDM components are structures formed by polymeric filaments partially bonded and voids. The mesostructure of FDM structures is defined by the geometry of the filaments and the bond between filaments, which are highly influenced by the printing parameters. These define the void density that at the same time, has a great influence on the final mechanical properties of FDM structures.

Taking into account these considerations, Li et al. (2002) proposed a theoretical equation to predict the void density as a function of the filament geometry of cross-section, which was idealised as an ellipse. Following a similar approach, in this section, an analytical equation for the prediction of the void density is proposed by means of the final geometry of the filaments. For that, assuming that the geometry of the filaments and the bond between them is equal within all the structure, only two filaments are considered as the smallest repeating unit of the structure as shown in Figure 3.16a. From the description of the printing process in Section 2.1.1 and experimental observations, the filament cross-section is ideally modelled as two half-discs and a rectangle, as a first approximation. Due to the void length is considered equal to the filament length, the void density is defined as the ratio of the area of voids to the cross-sectional area

$$\rho_{voids} = \frac{voids\ area}{total\ cross\text{-}sectional\ area} \tag{3.1}$$

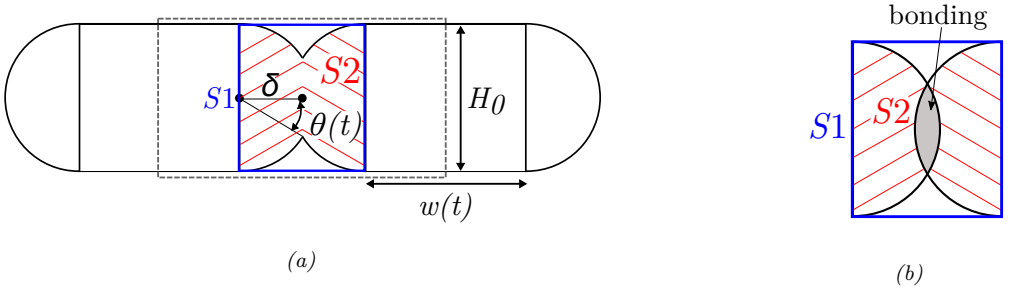

Figure 3.16 Final cross-sectional geometry of filament.

Assuming symmetric geometry, only half of each filament is considered (dashed line in Figure 3.16a), where $\theta(t)$ is the angle of intersection between both filaments (see Figure 3.16a) and δ is equal to $\frac{H_0}{2}cos(\theta(t))$. As such, the *total cross-sectional area* can be calculated as

$$total\ cross\text{-}sectional\ area = H_0 w(t) + {H_0}^2 cos(\theta(t)) \tag{3.2}$$

On the other hand, the *voids area* is defined as the subtraction of shaded area $S2$ from $S1$ (blue rectangle) (see Figure 3.16b). $S1$ defined as

$$S1 = {H_0}^2 cos(\theta(t)) \tag{3.3}$$

In turn, the $S2$ area is the subtraction of the grey area, in which bonding is supposed to take place, from the initial area of the half-disc. The grey area for each filament can be calculated as the area of a circular segment that is equal to $\frac{R^2}{2}(2\theta(t) - \sin(2\theta(t))$ where $R = \frac{H_0}{2}$. Therefore, $S2$ is obtained as

$$S2 = \pi \left(\frac{H_0}{2}\right)^2 - \left(\frac{H_0}{2}\right)^2 (2\theta(t) - sin(2\theta(t))) \tag{3.4}$$

Thus, the void density can be calculated as a function of the final geometry as

$$\rho_{voids} = \frac{{H_0}^2 cos(\theta(t)) - \left[\pi \left(\frac{H_0}{2}\right)^2 - \left(\frac{H_0}{2}\right)^2 (2\theta(t) - sin(2\theta(t)))\right]}{H_0 w(t) + {H_0}^2 cos(\theta(t))} \tag{3.5}$$

3.4.2 Validation

In order to validate the previously proposed expression, Equation (3.5) is used to predict the void density of longitudinal two-layer specimens (0.2 and 0.3 mm layer heights) taking as an input the previous experimental measurements. The intersection angle is calculated by trigonometry as $\theta(t) = \arcsin\left(\textit{Bond length}/H_0\right)$. Table 3.7 summarises the average of the experimental measurements obtained from two-layer longitudinal specimens (see Figures 3.5a and 3.5b) and the analytical predictions. The column 'width' collects the value of the parameter w (see Figure 3.16a).

Table 3.7 Comparison of void density results obtained by digitalized image analysis and analytical calculations.

Printing parameters		Experimental measurements				Analytical calculation
Layer height (μm)	Width line (μm)	Layer height (μm)	Width (w) (μm)	Bond length (μm)	Void density (%)	Void density (%)
200	400	237.4	366.0	190.3	2.07	1.77
300	400	374.4	268.5	259.2	4.75	4.78

Good agreement, errors of 14.5% and 0.6%, respectively, between theoretical predictions and the experimental results is observed. Thus, it can be concluded that despite the simplifications assumed, the analytical expression is able to predict the density of voids with good precision.

3.5 Analytical modelling for mechanical properties

3.5.1 Modelling formulation

The main challenge in FDM is the prediction of the mechanical properties as a function of the printing parameters. In this regard, parametric approaches have been used for the identification of the mechanical properties of FDM components from the printing parameters. Sood and coworkers (Sood et al., 2010, 2012) carried out mechanical tests based on central composite design from which empirical models were developed relating mechanical properties (tensile strength, compressive strength, flexural strength, and impact strength) and printing parameters (layer thickness, orientation, raster angle, raster width and air gap). Moreover, Liu et al. (2017) presented an experimental research approach based on the Taguchi method to study the influence of printing parameters on the mechanical properties of FDM components (tensile strength, flexural strength and impact strength). From the experimental results, they used the gray relational analysis to propose a set of optimal printing parameters. However, these models do not link mechanical properties with physical variables and are only able to predict the influence of the printing parameters used in those studies.

On the other hand, numerous relationships have been proposed in the literature to determine the dependence of mechanical properties on porosity. These equations are usually classified into linear, power or exponential mechanical properties-porosity relationships (Choren et al., 2013). However, from the results obtained in the experimental characterisation, it is observed that the number of layers of the components plays also a crucial role in the determination of the final properties.

In this section, analytical expressions for the elastic modulus and maximum stress are proposed as a function of two structural parameters: the number of layers (Z) and void density (ρ_{voids}). For the sake of convenience, the void density is expressed per unit instead of %. According to the experimental results, an additive expression, with an exponential and a linear term, is proposed for longitudinal raster orientation as

$$\begin{aligned} E_{long} &= E_{01}\left(e^{[(1-\rho_{voids})^{C_E Z}]} - \rho_{voids}\right) + E_{02}\left(1-\rho_{voids}\right) \\ \sigma_{long} &= \sigma_{01}\left(e^{[C_{1\sigma}(1-\rho_{voids})^{C_{2\sigma} Z}]} - \rho_{voids}\right) + \sigma_{02}\left(1-\rho_{voids}\right) \end{aligned} \tag{3.6}$$

where E_{01}, E_{02}, σ_{01}, σ_{02} are material parameters that define the extreme values of the Young's modulus and maximum stress. The parameters C_E and $C_{2\sigma}$ control the sensitivity of the mechanical properties with the number of layers. $C_{1\sigma}$ controls the increasing or decreasing trend of the maximum stress with the number of layers and void density, which is different depending on the raster orientation. Note that these theoretical expressions are consistent for extreme values of void density. Indeed, if the

void density is equal to zero (perfect bonding), the Young's modulus and maximum stress are $E_{long} = E_{01}e + E_{02}$ and $\sigma_{long} = \sigma_{01}e + \sigma_{02}$, respectively. These values correspond to the values specified in the datasheet of the ABS filament used for the experimental work. Conversely, if the void density is 1 (100%), the value of the properties is zero. Regarding the number of layers, if this parameter tends to infinity the mechanical properties are $E_{long} = (E_{01} + E_{02})(1 - \rho_{voids})$ and $\sigma_{long} = (\sigma_{01} + \sigma_{02})(1 - \rho_{voids})$, respectively.

Regarding the properties for transversal raster orientation, they can be obtained as a multiple of the longitudinal ones by making use of empirical factors $\zeta_{1,2}$ such that

$$\begin{aligned} E_{trans} &= \zeta_1 E_{long} \\ \sigma_{trans} &= \zeta_2 \sigma_{long} \end{aligned} \tag{3.7}$$

3.5.2 Validation

The material parameters are calibrated using an optimisation algorithm, an unconstrained derivate-free method (*fminsearch* function of MATLAB), by taking as reference the experimental results at a strain rate of $3 \cdot 10^{-4} s^{-1}$. The optimised parameters are shown in Table 3.8.

Table 3.8 Model parameters for the analytical modelling of mechanical properties.

C_E	$C_{1\sigma Long}$	$C_{1\sigma Trans}$	$C_{2\sigma}$	E_{01} (MPa)	E_{02} (MPa)	σ_{01} (MPa)	σ_{02} (MPa)	ζ_1	ζ_2
23	1	-1	21	318	1497	6	31	0.94	0.45

The predictions from the analytical expression for the different raster orientation are compared with the experimental results in Figures 3.17 and 3.18. Good agreement between experimental data and analytical predictions is obtained with an error by up to 6% for longitudinal specimens and by up to 8% and 18% for the elastic modulus and maximum stress, respectively, for transversal.

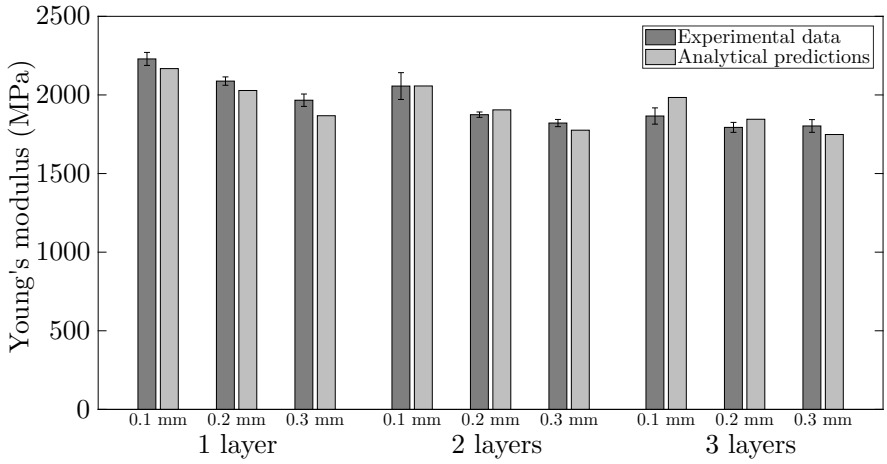

(a)

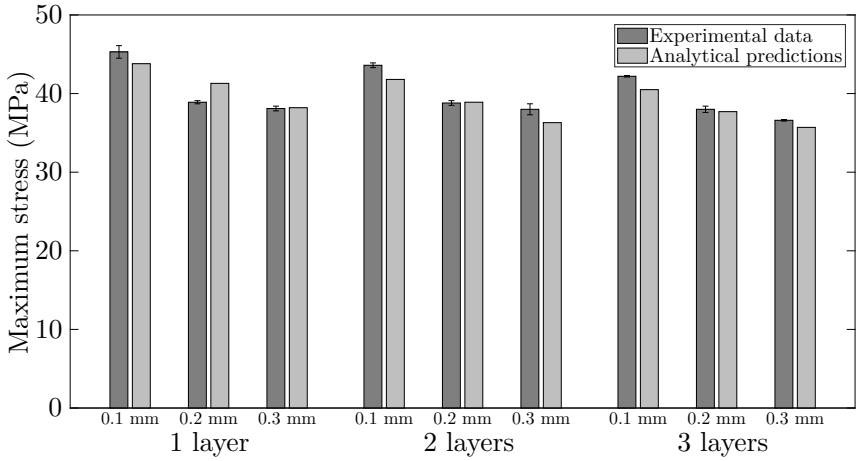

(b)

Figure 3.17 Comparison between experimental mechanical properties (with error bars) and analytical predictions for longitudinal specimens.

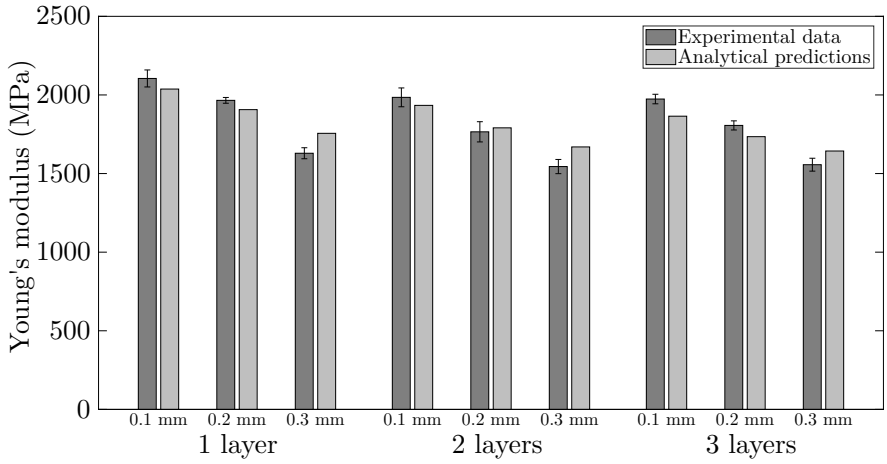

(a)

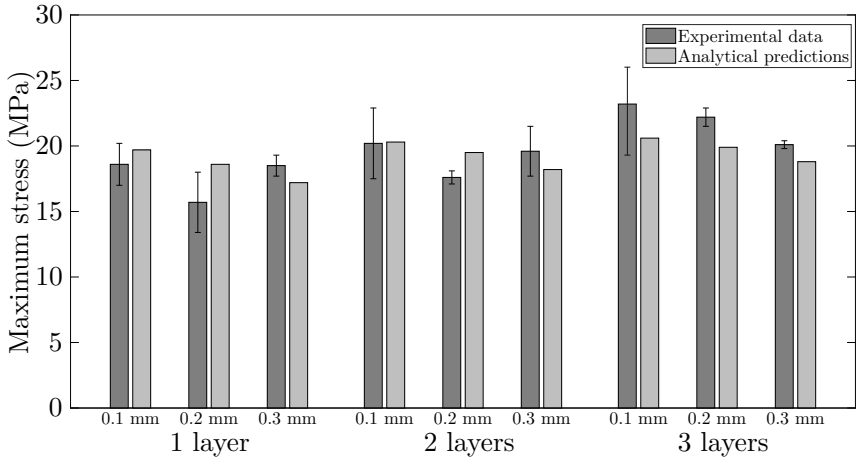

(b)

Figure 3.18 Comparison between experimental mechanical properties (with error bars) and analytical predictions for transversal specimens.

3.6 Conclusions

In this chapter, the influence of printing parameters on the mesostructure and mechanical performance of FDM components is studied. To this end, an experimental mesostructural and mechanical characterisations are carried out on ABS components studying the influence of: layer height, raster orientation and number of layers. While the influences of the layer height and raster orientation have been widely studied in the literature, the influence of the number of layers, which produces a change in the number of bonding interfaces, has hardly been studied.

Higher elastic modulus and maximum stress are observed for lower layer heights and a longitudinal raster orientation. This improvement is accompanied by a decrease in the void density as layer height decreases. Otherwise, increasing the number of layers leads to lower mechanical properties, with the exception of the maximum stress for transverse components. In addition, while longitudinal specimens present an elastoplastic behaviour, where crazing and shear banding mechanics are observed, transverse ones present a brittle behaviour.

Moreover, from previous experimental results, analytical expressions are developed to predict the void density and mechanical properties in terms of elastic modulus and maximum stress, taking manufacturing parameters and filament properties as inputs. These expressions are validated with the experimental data showing both good capability to predict the tendencies observed experimentally.

4 Thermal and sintering models of the manufacturing process

In the previous chapter, the influence of the printing parameters on the mesostructure and the mechanical properties of FDM components has been studied. From the previous results, it is observed that FDM polymers are composed of layers joined together, where each layer is in turn composed of polymeric filaments partially bonded and voids. The void density, fibre-to-fibre bond strength and filament properties determine the mechanical properties of FDM components. Both void density and fibre-to-fibre bond strength are defined by the bonding process that takes places during the manufacturing process. In this regard, it is important to deep in the mechanical and thermal description of the printing process and its implications in the mesostructure. Thus, in this chapter, thermal and sintering models are proposed to describe the thermodynamic of the 3D printing process.

To this end, the outline of the chapter is as follows: Section 4.1 presents an introduction of the bonding process; in Section 4.2, a thermal model is proposed; in Section 4.3, an analysis of the intra-fibre heat transfer is carried out; in Section 4.4, a sintering model is developed; in Section 4.5, the healing process is approached. Finally, the conclusions of the chapter are presented in Section 4.6.

4.1 Introduction

Immediately after the deposition of a filament, it starts to cool from extrusion temperature to environmental temperature (Bahr and Westkamper, 2018), while bonding with the adjacent filaments (Bellehumeur et al., 2004). This phenomenon is a process driven by the thermal energy of the semi-molten material (Bahr and Westkamper, 2018; Bellehumeur et al., 2004; Sun et al., 2008). The formation and quality of the bond depends on both neck growth between filaments and the molecular diffusion reached within it. In this regard, healing refers to the molecular diffusion across the contact area of two materials that are in intimate contact (Yang and Pitchumani, 2002). This phenomenon takes place

as long as the temperature is above T_g and can be described in five steps as (see Figure 4.1): (1) surface rearrangement, (2) surface approach, (3) wetting, (4) diffusion, and (5) randomization (Wool and O'Connor, 1981).

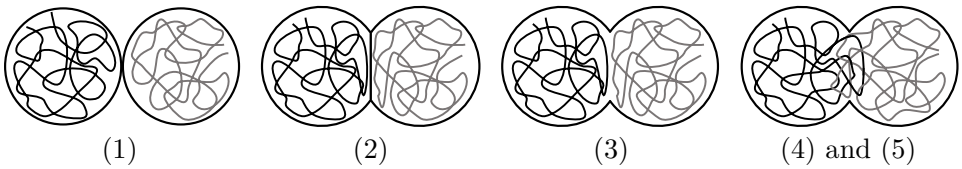

Figure 4.1 Deposition sequence of the two layers structure, adapted from Coogan and Kazmer (2017).

During the first two steps, intimate contact between the polymer surfaces is achieved. After that, wetting occurs instantaneously when the temperature is above T_g (Coogan and Kazmer, 2017). Once wetting has occurred, the polymer chains diffuse across the interface (Coogan and Kazmer, 2017).

On the other hand, sintering is the phenomenon of coalescence of particles and is driven by two temperature-dependent properties: surface tension and viscosity (Bellehumeur et al., 1996; Pokluda et al., 1997). To achieve a complete coalescence between filaments, it is necessary to lower enough the viscosity to enhance the flow of the material. However, the use of high extrusion temperatures, necessary to achieve low viscosities, can induce thermal damage (Rodriguez et al., 2000). Therefore, the bonding between filaments of FDM components is not perfect, leading to the formation of voids between rasters.

As stated, the printing process and all the physical phenomena that take places during it are governed by the temperature. Therefore, the evolution of the temperature of filaments during the printing process plays a crucial role in the determination of the bonding, quality and, therefore, the final properties of FDM componentS.

4.2 Thermal model

The temperature history of filaments during the manufacturing process plays an important role in the determination of the quality of the bonds and the molecular-diffusion reached within them. Once a filament is deposited, a quick solidification is desired to avoid excessive deformation due to gravity or the weight of other filaments deposited above (Costa et al., 2017). Conversely, filaments need to remain at high temperature during enough time to ensure adequate bonding with adjacent filaments.

The temperature evolution of filaments during the 3D printing process depends on the thermal conditions such as environment, platform and extrusion temperatures, as well as other variables such as the print speed and cross-sectional area, which are defined by the printing parameters (layer height and line width). In this regard, Thomas and Rodriguez (2000) carried out a 2D transient heat transfer analysis applied to a filament

deposited on a vertical stack. However, this model assumes a rectangular cross-section and does not account for contacts between filaments. Moreover, other authors have used the lumped-heat-capacity (LC) method to analyse the cooling process of the extruded filament, providing a one-dimensional transient heat transfer model (Bellehumeur et al., 2004; Sun et al., 2008). This model assumes uniform temperature distribution along the cross-section. In addition, since the mass of the platform is considered much higher than that of the filament, the heat transfer with the platform can be considered in the form of convection. However, due to LC model is a 1D model, the effects of heat transfer with adjacent filaments are not taken into account. Recently, Costa et al. (2017) proposed a new analytical solution for the temperature evolution during the printing process in FDM techniques. The boundary conditions considered are the contact between filaments, between the filament and the 3D printer support, and the heat transfer with the environment. Thus, once the filament is deposited, heat exchange occurs by convection with the environment and by conduction with the support and adjacent filaments. Considering a filament segment of length dx, the resulting energy balance can be written as

$$\Delta \mathrm{U} + \mathrm{Q} = 0 \tag{4.1}$$

where Q is understood as the sum of the heat transfer by convection with the environment, the heat transfer by conduction between filaments and the axial heat transfer by conduction within the filament segment, and ΔU is the change in internal energy. Mathematically, it can be written as

$$\begin{aligned} -kA\frac{\partial T_r(x,t)}{\partial x} - h_{conv}(A_r)_{conv}(T_r(x,t) - T_E) - \sum_{i=1}^{n} h_i A_{ri}(T_r(x,t) - T_{ri}(t)) = \\ \rho C_p A \frac{\partial T_r(x,t)}{\partial t} dx - A\left[k\frac{\partial T_r(x,t)}{\partial x} + \frac{\partial\left(\frac{\partial T_r(x,t)}{\partial x}\right)}{\partial x}\right] \end{aligned} \tag{4.2}$$

where the different variables for this equation and others used next are summarized in Table 4.1. For the sake of convenience, in this section and in the following, °C is used as the temperature unit.

Due to the low thermal conductivity of most polymers and the small cross-section of the extruded filaments, the axial heat conduction can be neglected compared to the remaining terms (Costa et al., 2015). Therefore, the Equation (4.2) can be rewritten as

$$\rho C_p A \frac{\partial T_r(x,t)}{\partial t} dx = -\left(h_{conv}(A_r)_{conv}(T_r(x,t) - T_E) + \sum_{i=1}^{n} h_i A_{ri}(T_r(x,t) - T_{ri}(t))\right) \tag{4.3}$$

Table 4.1 Nomenclature of the thermal model.

Nomenclature	
$T_r(x,t)$	Temperature at localisation x and time t of a given filament segment r (°C)
$T_{ri}(t)$	Temperature contact i with the filament segment r at time t (°C)
T_E	Environment temperature (°C)
T_{supp}	Support temperature (°C)
T_{extr}	Extrusion temperature (°C)
$t_r(x)$	Time at which filament segment r is deposited(s)
P	Perimeter of the cross-section area (m)
λ_i	Fraction of P
A	Cross-sectional area (m^2)
$(A_r)_{conv}$	Area exposed to the environment r (m^2)
A_{ri}	Area of contact i for the filament segment r (m^2)
dx	Filament segment length (m)
k	Thermal conductivity coefficient (W/m°C)
h_{conv}	Convective heat transfer coefficient (W/m^{2}°C)
h_i	Heat transfer coefficient of contact i (W/m^{2}°C)
C_p	Specific heat capacity (J/kg°C)
ρ	Density (kg/m^3)
n	Number of physical contacts with adjacent filament segment or support
m	Number of discretised filament segments in the component

The area of filament in contact with a filament segment r or with the support can be expressed as a function of the fraction λ_i of the total perimeter P as

$$A_{ri} = Pa_{ri}\lambda_i dx \tag{4.4}$$

where $i \in \{1, \ldots, n\}$ is each one of the contacts expressed in local numbering as shown in Figure 4.2.

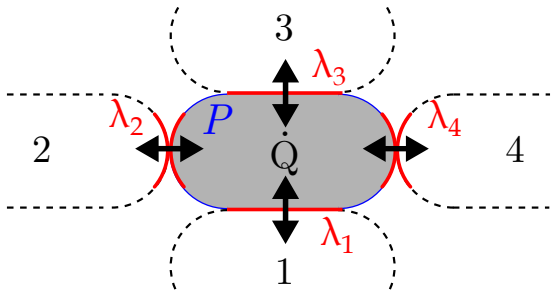

Figure 4.2 Contact areas and heat flows of a single element.

Although the model proposed by Costa et al. (2017) is formulated to be used with different strategies of deposition, in this thesis only aligned strategy is contemplated.

Thus, each filament can have a maximum of four contacts with other filaments and the support. Therefore, assuming $n \leq 4$, where n is the total number of contacts, the variable a_{ri} takes 1 if the filament segment r is in contact with other filament segment or with the support, and 0 otherwise.

Similarly, the area exposed to the environment can be expressed in terms of the total perimeter P as

$$(A_r)_{conv} = P\left(1 - \sum_{i=1}^{n} a_{ri}\lambda_i\right)dx \tag{4.5}$$

Taking Equations (4.4) and (4.5) and using the characteristic polynomial method (Palais and Palais, 2009), the analytical solution for the time evolution of the filament temperature reads

$$T_r(x,t) = C_1 exp\left[\frac{-Pb(a_{r1},...,a_{rn})}{\rho CA}(t - t_r(x))\right] + Q(a_{r1},...,a_{rn}) \tag{4.6}$$

where t is the instant of time of printing process, $t_r(x)$ is the time at which each filament segment is deposited, and C_1 is defined as

$$C_1 = T_{extr} - Q(a_{r1},...,a_{rn}) \tag{4.7}$$

where T_{extr} is the extrusion temperature and $b(a_{r1},...,a_{rn})$ and $Q(a_{r1},...,a_{rn})$ are functions that depend on the existing contacts

$$b(a_{r1},...,a_{rn}) = h_{conv}\left(1 - \sum_{i=1}^{n} a_{ri}\lambda_i\right) + \sum_{i=1}^{n} a_{ri}h_i\lambda_i \tag{4.8}$$

$$Q(a_{r1},...,a_{rn}) = \frac{h_{conv}(1 - \sum_{i=1}^{n} a_{ri}\lambda_i)T_E + \sum_{i=1}^{n} a_{ri}h_i\lambda_i T_{ri}(t)}{b(a_{r1},...,a_{rn})} \tag{4.9}$$

4.2.1 Implementation

In the original work by Costa et al. (2017), the implementation algorithm includes an iterative process to calculate the temperature of two filaments in contact. This is because the temperature in the filament segment depends on the temperature of the segments in contact and belonging to other filaments. Regarding this fact, the formulation is rewritten in order to solve implicitly all temperatures at the same time to avoid the iterative process. To this end, the Equation (4.8) is divided into two terms. The first term K_1 defines the heat transfer by convection with the environment per °C, while the second term K_2 defines the heat transfer by conduction between adjacent filament or

support per °C

$$b(a_{r1},...,a_{rn}) = \underbrace{h_{conv}\left(1-\sum_{i=1}^{n} a_{ri}\lambda_i\right)}_{K_1} + \underbrace{\sum_{i=1}^{n} a_{ri}h_i\lambda_i}_{K_2} \tag{4.10}$$

Combining (4.6), (4.7) and (4.10), the evolution of the temperature can be expressed as

$$\begin{aligned} T_r(x,t) = T_{extr}exp\left[\frac{-P(K_1+K_2)}{\rho CA}(t-t_r(x))\right] \\ +Q(a_{r1},...,a_{rn})exp\left[1-exp\frac{-P(K_1+K_2)}{\rho CA}(t-t_r(x))\right] \end{aligned} \tag{4.11}$$

Organizing dependent and independent terms of filament segments temperature, and considering $\beta = \frac{-P(K_1+K_2)}{\rho CA}$, we obtain

$$\begin{aligned} T_r(x,t) - \frac{\sum_{j=1}^{m} a_{rj}h_j\lambda_j T_{rj}(t)}{K_1+K_2}\left[1-exp\beta(t-t_r(x))\right] = T_{extr}exp\left[\beta(t-t_r(x))\right] \\ + \frac{K_1T_E}{K_1+K_2}\left[1-exp\beta(t-t_r(x))\right] + \frac{a_{r\,supp}\lambda_{supp}h_{supp}T_{supp}}{K_1+K_2}\left[1-exp\beta(t-t_r(x))\right] \end{aligned} \tag{4.12}$$

where m is the total number of filament segments that made the component, T_{supp} is the support temperature, h_{supp} is the heat transfer coefficient between filament segment and support, λ_{supp} is the fraction of the perimeter in contact with the support, and $a_{r\,supp}$ is a variable that takes 1 if there is contact between the filament element and the support, and 0 otherwise. Ultimately, the expression can be written in matrix notation as

$$\mathbf{A}\cdot\mathbf{T_r} = \mathbf{B} \tag{4.13}$$

where $\boldsymbol{A}_{mm}$ are all the temperature dependent terms and $\boldsymbol{B}_{m1}$ are all the temperature independent terms of Equation (4.12).

The thermal model is implemented in MATLAB. Aiming at reducing the simulation time, in every step $\mathbf{A}$ is a square matrix of size (n° deposited elements, n° deposited elements), whereas $\mathbf{T_r}$ and $\mathbf{B}$ are column vectors of size (n° deposited elements). In this way, the matrices will grow each time a new element is deposited. In addition, since each filament segment has a maximum of four contacts with other filament segments, most of the elements of the matrix $\mathbf{A}$ are zero, so it can be considered as a sparse matrix. Therefore, to further reduce the computing time and cost, the matrix $\mathbf{A}$ and $\mathbf{B}$ are stored as sparse matrices (Pissanetzky, 1984).

4.2.2 Results and discussion

In this subsection, the influence of the deposition sequence, number of layers, and extrusion and environmental temperatures on the evolution of filament temperature is evaluated. The set of process and printing parameters is given in Table 4.2. In these cases, the area and perimeter of the cross-section is calculated using the geometry described in Section 2.1.1. The shape of the cross-section and thermal properties are assumed constant throughout the printing process. Moreover, in order to simplify the problem, a constant environment temperature is assumed. However, the temperature of the different regions of the 3D printer changes according to the movement of the extrusion head, whose temperature is much higher than the ambient temperature of the camera (in case of having one) or the room where the 3D printer is placed (Sun et al., 2008). Therefore, the air flow around the specimen during the manufacturing process is far from homogeneous (Sun et al., 2008).

Table 4.2 Printing and material parameters (Bellehumeur et al., 2004; Costa et al., 2017).

Property	Value
Layer height	0.3 mm
Line width	0.4 mm
Printing speed	30 mm/s
Environment temperature (T_E)	50 °C
Printing temperature (T_{ext})	240 °C
Build plate temperature (T_{supp})	100 °C
Fraction of perimeter for contacts (λ_i)	0.15
Convective coefficient (h_{conv})	70 W/m^2°C
Conduction coefficient between filament segment and support (h_{supp})	300 W/m^2°C
Conduction coefficient between filament segments (h_i)	70 W/m^2°C
Specific heat capacity (C_p)	2019.7 J/kg ° C
Density (ρ)	1040 kg/m^3
Glass transition temperature (T_g)	94 °C

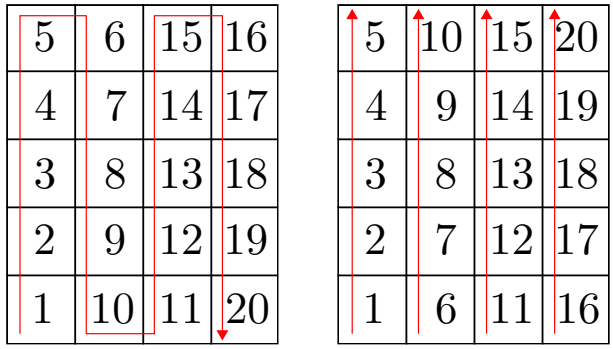

Figure 4.3 Different deposition sequence considered (red arrow indicates the direction of deposition).

Two different deposition sequences are analysed, see Figure 4.3. *Configuration 1* represents the deposition sequence presented by default in most of the slicer software. On the contrary, in *Configuration 2*, there is the same time interval between the deposition of each filament segment and the deposition of the adjacent segment that belongs to another filament. The temperature profiles of the initial and final segments of each filament for both configurations are shown in Figures 4.4 and 4.5. Observing the temperature profiles of segment 1, 6 and 11 using the first deposition sequence (*Configuration 1*), there is an increase of about 11 °C when the adjacent segments 10, 15 and 20 are deposited respectively. On the other hand, observing the segments 5, 10 and 15, due to their adjacent segment (6, 11 and 16, respectively) are deposited just after them, their temperature increase only in 1 °C (marked with a circle in Figure 4.4).

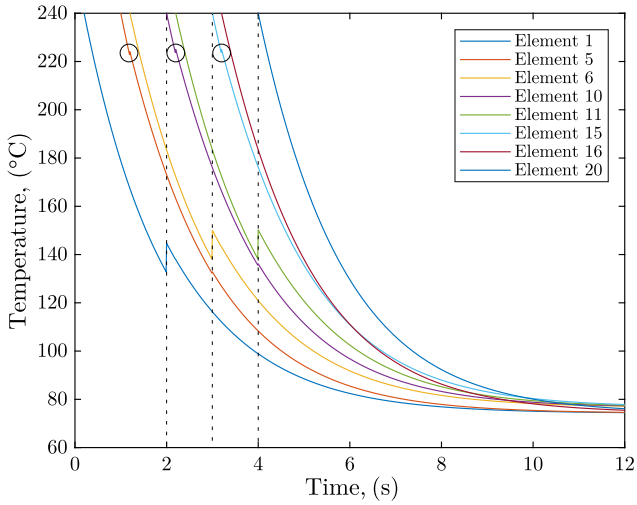

Figure 4.4 Temperature evolution of filaments in Configuration 1, according to Figure 4.3.

On the other hand, all the segments increase their temperature in 7.7 °C when a new filament segment is deposited on its right when the second configuration deposition sequence (*Configuration 2*) is used. Thus, a more uniform temperature profile is obtained with *Configuration 2*.

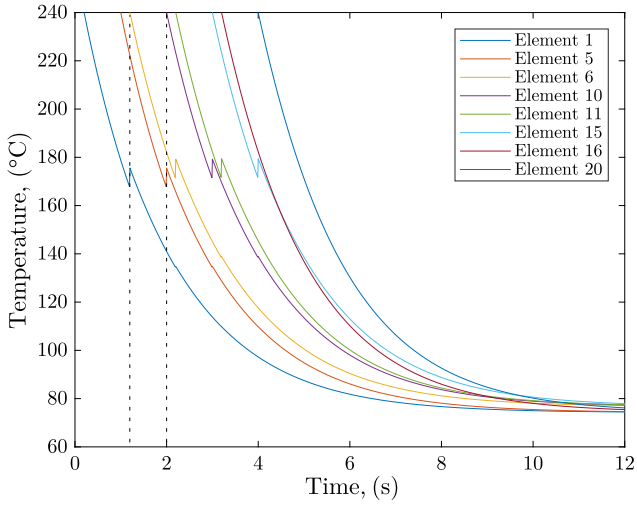

Figure 4.5 Temperature evolution of filaments in Configuration 2, according to Figure 4.3

Moreover, in order to analyse the effects of depositing a filament segment on the top of another, the temperature evolution of a two-layer component is reproduced as shown

in Figure 4.6. The temperature evolution of four adjacent segments, 1, 10, 21 and 30, are shown in Figure 4.7.

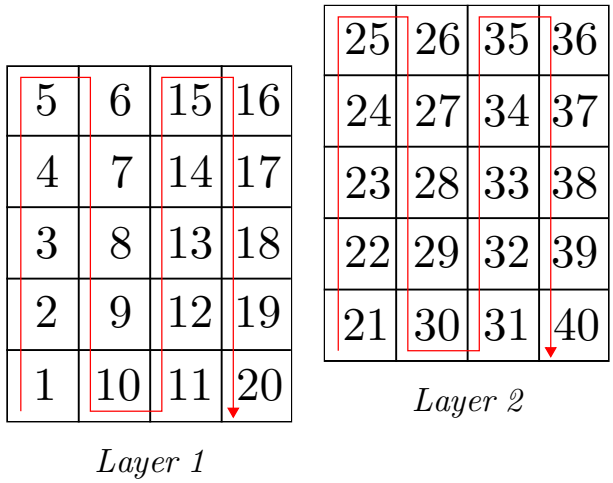

Figure 4.6 Deposition sequence of the two layers component (red arrow indicates the direction of deposition).

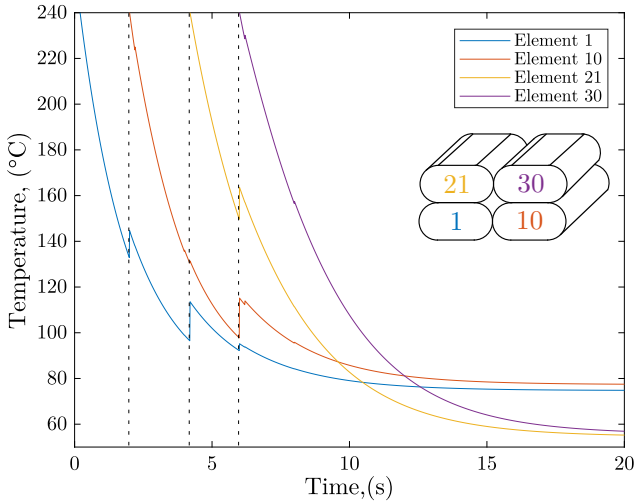

Figure 4.7 Temperature evolution of filaments of two layers specimen, according to Figure 4.6.

Three different peaks are observed in the temperature evolution of the segment 1 with the time, corresponding to the deposition of the other three segments. With the deposition of segment 10, the temperature of segment 1 increases about 11 °C as in the previous example (*Configuration 1*). However, when the element 21 is deposited, which

is the filament element deposited above it, the temperature increases by up to 17 °C. This increase is due to the fact that with the deposition of segment 21, the heat loss by convection decreases while a higher positive heat flow is introduced by conduction to the segment. Moreover, it can be observed that in the temperature evolution of the element 21 there is an increase of about 13 °C in temperature due to the deposition of the adjacent element 30. Furthermore, it must be noted that while the filaments deposited in the second layer tend to a temperature of about 50 °C, the filaments of the first layer tend to a temperature of about 70 °C. This discrepancy is due to the differences in temperature between the support temperature that is 100 °C and the environment temperature around the printing zone that in this case is fixed at 50 °C.

Lastly, some studies have shown the influence of the magnitude $T_{extr} - T_E$ in the void density (Rodriguez et al., 2000). In this regard, Figure 4.8 shows the temperature evolution versus time for two sets of processing temperatures. Large differences between the extrusion and environmental temperatures induce faster rates of cooling before reaching T_g. Although faster cooling rates avoid excessive deformation due to gravity or the weight of other filaments, increasing the period of time in which the filament is above the glass transition temperature improves the bonding process (Rodriguez et al., 2000). On the other hand, a high extrusion temperature is required to lower the viscosity and enhance the flow of material through the extruder. However, as stated in Section 4.1, unfortunately, the temperature needed to achieve low viscosity to improve the extrusion and reach a complete filling of the voids, can induce irreversible thermal damage. Therefore, an equilibrium between T_{extr} and T_E is needed to get the optimal solution for the 3D printing process.

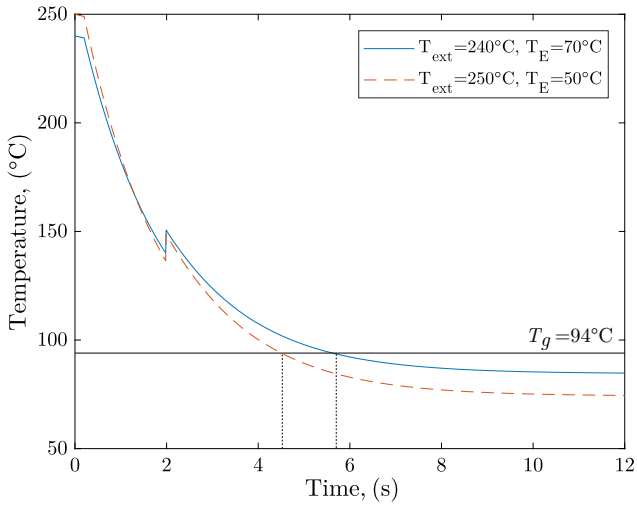

Figure 4.8 Influence of $T_{extr} - T_E$ on the temperature of the filament segment.

4.3 Analysis of the intra-fibre heat transfer

From the analysis of the mesostructure developed in Chapter 3, it is concluded that the top regions of the fibres are flatter than the bottom regions independently of the printing parameters used in this work. In this regard, Rodriguez et al. (2000) also observed an asymmetric shape in the mesostructure of the FMD components manufactured with different air gap, flow rate, and extrusion and environmental temperature conditions; and different deposition strategies: aligned and skewed. Although in the previous section the temperature inside the cross-section is assumed constant and uniform, the asymmetric shape is, in part, due to a highly non-uniform temperature distribution along the section of each fibre. Temperature gradients in the fibre cause a non-uniform viscosity inside the material, which leads to enhance the flow process in those areas where the viscosity is lower. To analyse these effects, a 2D heat transfer model has been proposed and numerically implemented in MATLAB using finite differences.

The finite difference method is a numerical method for solving partial differential equations (PDE) by discrete approximations. The physical domain is discretised in a finite number of points where the discrete solution is computed. Therefore, increasing the number of points improves the accuracy of the numerical solution while requiring higher computational time. These points are referred to as *nodes*, which compose the imaginary *mesh* presented in Figure 4.9, where Δx and Δy are the local distances along the x and y axes between adjacent *nodes*. In addition, Δt is the time step used for the temporal discretisation.

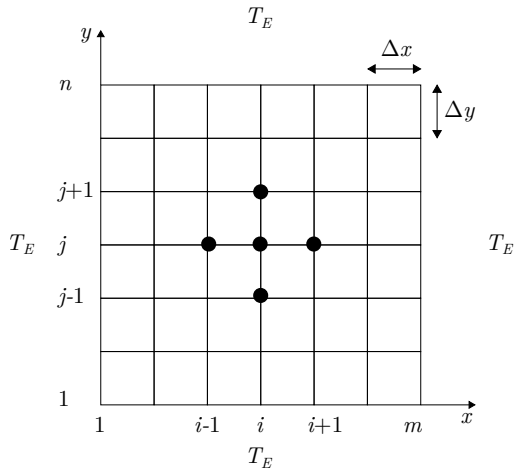

Figure 4.9 Two dimensional finite difference grid.

The heat diffusion equation is expressed as

$$k\nabla^2 T = \rho C_p V \frac{\partial T}{\partial t} + h_{conv}(A)_{conv}(T - T_E) \tag{4.14}$$

where k is the thermal conductivity, ρ is the density, C_p is the specific heat capacity, h_{conv} is the convective heat transfer coefficient, T_E is the environmental temperature, V is the volume and $(A)_{conv}$ is the convection area. No generation of heat flux is considered.

Applying the finite difference method, the differential equations are spatially and temporally discretised in *nodes* and time increments, respectively. Considering a 2D problem, Δz can be assumed as $\Delta z = 1$ and, therefore, $V = \Delta x \Delta y$ is the volume of the grid. In addition, it is considered that $\Delta x = \Delta y$ and, therefore, the area of convection can be expressed as $(A)_{conv} = \Delta x$ for all the cases.

4.3.1 Implementation

For the implementation of the heat diffusion equation, an explicit scheme is used. Therefore, it is computed forward in time using the temperatures from previous time steps. Due to the initial conditions depend on the position of the *node* inside the *mesh*, the equations for three different position (interior *node*, external *node* and corner *node*) are presented, see Figure 4.10.

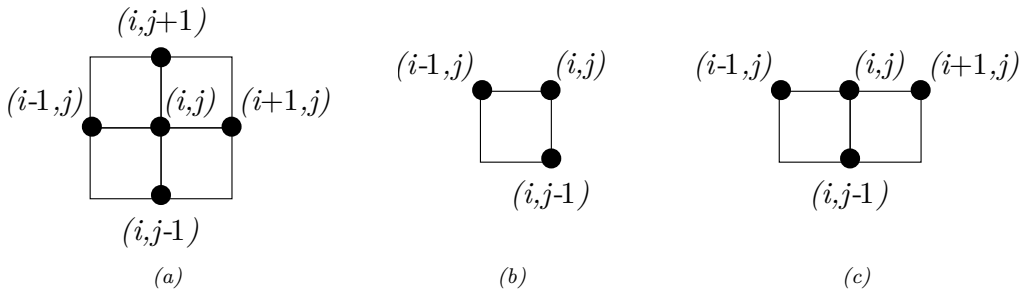

Figure 4.10 Equations considering different nodes: (a) interior node, (b) corner node and (c) exterior node.

Considering an interior *node*, heat exchange by conduction is produced with all the adjacent nodes, and the equation for this first case can be expressed as

$$\frac{T_{i,j}^{t+1} - T_{i,j}^{t}}{\Delta t} = \alpha \frac{T_{i+1,j}^{t} + T_{i-1,j}^{t} - 2T_{i,j}^{t}}{\Delta x^2} + \alpha \frac{T_{i,j+1}^{t} + T_{i,j-1}^{t} - 2T_{i,j}^{t}}{\Delta y^2} \tag{4.15}$$

where $\alpha = \frac{k}{\rho C_p}$ is a constant diffusion coefficient. Organising terms, the temperature in the instant $t + \Delta t$ can be obtained as

$$T_{i,j}^{t+1} = T_{i,j}^{t} + \alpha \Delta t \frac{T_{i+1,j}^{t} + T_{i-1,j}^{t} - 2T_{i,j}^{t}}{\Delta x^2} + \alpha \Delta t \frac{T_{i,j+1}^{t} + T_{i,j-1}^{t} - 2T_{i,j}^{t}}{\Delta y^2} \tag{4.16}$$

If the *node* is a corner *node*, heat exchange by conduction is produced with $(i-1,j)$ and $(i,j-1)$ nodes, while a convective heat flux is generated with the ambient as

$$T_{i,j}^{t+1} = T_{i,j}^{t} + \alpha\Delta t\frac{T_{i-1,j}^{t} - T_{i,j}^{t}}{\Delta x^2} + \alpha\Delta t\frac{T_{i,j-1}^{t} - T_{i,j}^{t}}{\Delta y^2} - \frac{h_{conv}}{\rho C_p}\frac{2\Delta t}{\Delta x}(T_{i,j}^{t} - T_E) \tag{4.17}$$

Moreover, an exterior *node* exchanges heat by conduction with $(i-1,j)$, $(i,j-1)$ and $(i+1,j)$ nodes, and by convection with the ambient. In that case, the equation can be expressed as

$$\begin{aligned} T_{i,j}^{t+1} = T_{i,j}^{t} + \alpha\Delta t\frac{T_{i+1,j}^{t} + T_{i-1,j}^{t} - 2T_{i,j}t}{\Delta x^2} + \alpha\Delta t\frac{T_{i,j-1}^{t} - T_{i,j}^{t}}{\Delta y^2} \\ - \frac{h_{conv}}{\rho C_p}\frac{\Delta t}{\Delta x}(T_{i,j}^{t} - T_E) \end{aligned} \tag{4.18}$$

Finally, to define the temporal step size and spatial mesh step, it is necessary to ensure the stability and the convergence of the simulations. To ensure stability using an explicit finite differences scheme, the next inequality has to be satisfied

$$\alpha\left(\frac{\Delta t}{\Delta x^2} + \frac{\Delta t}{\Delta y^2}\right) \leq \frac{1}{2} \tag{4.19}$$

Due to the consideration of $\Delta x = \Delta y$, the inequality (4.19) can be expressed as

$$\Delta t \leq \frac{\Delta x^2}{4\alpha} \tag{4.20}$$

4.3.2 Results and discussion

In order to analyse the intra-fibre heat transfer, in this section, the cross-section temperature profile is obtained for the filament segments 1, 10, 21 and 30 presented in the previous section (see Figure 4.6). The initial temperature imposed in each segment is presented in Table 4.3. These temperatures coincide with the temperature reached after 6 seconds of the beginning of the manufacturing process, instant in with segment 30 is deposited (see Figure 4.7).

Table 4.3 Initial temperatures of filaments analysed.

Segment	Temperature
1	95.2 °C
10	115.2 °C
21	163.6 °C
30	240 °C

In order to simplify the problem, a square cross-section is assumed with width and height of 0.3 mm. In addition, the heat transfer by conduction with the remaining segments and with the support is neglected. In this regard, the heat transfer by convection is considered only on the left edge of the segments 1 and 21, and the edge of the top of the segments 21 and 30. A thermal conductivity of $k = 0.1768$ W/m°C is used (Rodriguez and et al., 2000). The remaining properties are the same as those given in Table 4.2. Figure 4.11 shows the results of the four segments after 0.18 s. A non-uniform distribution is observed, being the bottom left corner the cooler point, coinciding with the first segment deposited, and reaching the higher temperature in the upper right corner, coinciding with the last segment deposited.

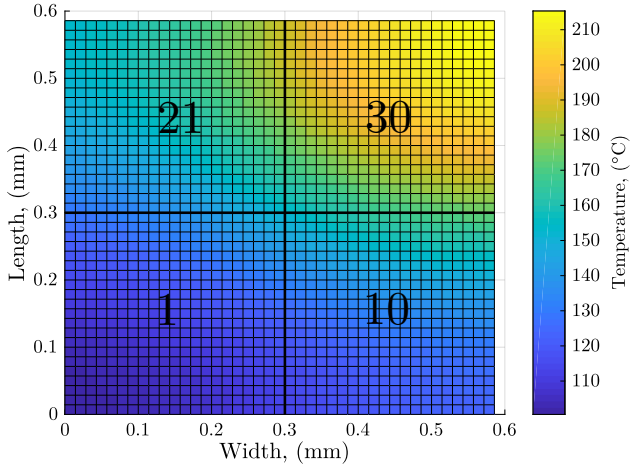

Figure 4.11 Intra-fibre heat transfer analysis at t=0.18 s: temperature profile of segments 1, 10, 21 and 30, according to Figure 4.6.

Furthermore, Figure 4.12 shows the temperature distribution inside the segment 30. Observing this latter, higher temperatures are reached in the upper part of the filaments, being the upper right corner where higher temperatures prevail, the furthest region from the adjacent filaments. This trend is in agreement with the transient heat transfer analysis carried out by Rodriguez et al. (2000) on an elliptical fibre, using the finite element code ABAQUS.

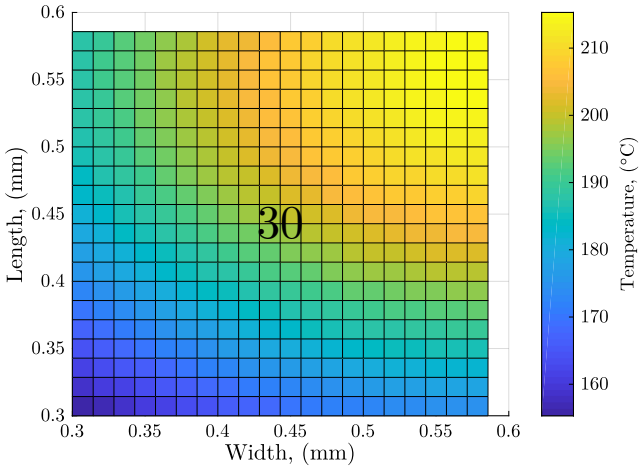

Figure 4.12 Intra-fibre heat transfer analysis at t=0.18 s: segment 30, according to Figure 4.6.

Due to the simplification considered, the temperature in the segment 30 is lower than the obtained in the instant 6.18 s in Figure 4.7. However, the objective of this section is to analyse the asymmetric temperature distribution inside the filament.

This non-uniform temperature distribution together with the way in which the filament is deposited, where the extruder applies a continued downward pressure during 3D printing, is thought to be the reason for the flattening in the top side of the filaments, see Figure 4.13.

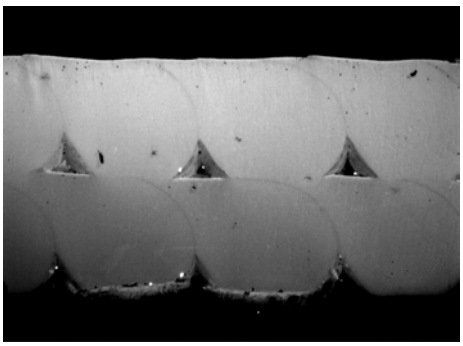

Figure 4.13 Mesostruture for FDM-ABS material with a layer height of 0.3 mm.

4.4 Model of sintering

Sintering is defined as the coalescence of particles under the action of surface tension (Bellehumeur et al., 1996; Pokluda et al., 1997). This phenomenon takes place in polymers at a temperature above the glass transition (Rosenzweig and Narkis, 1981) when the

material is in a viscous or rubbery state. However, experimental observations suggest that most of the neck growth occurs at temperatures above a material-characteristic temperature known as critical sintering temperature (about 200 °C for the ABS) (Bahr and Westkamper, 2018; Bellehumeur et al., 2004).

In the case of amorphous polymers, such as ABS, experimental studies have led to the conclusion that sintering mechanism of these polymers is essentially a Newtonian viscous flow where surface tension is the major driving force (Rosenzweig and Narkis, 1981). In this regard, some authors have proposed different analytical models to describe the sintering process of polymers (Frenkel, 1945; Hopper, 1984; Pokluda et al., 1997). The first analytical approach describing the sintering process was proposed by Frenkel (1945). This model is based on Newtonian viscous flow under the action of surface tension of two identical spheres. However, this model does not satisfy the continuity equation. In this regard, Eshelby (1949) proposed a corrected model based on this latter, which is known as Frenkel/Eshelby model, and where the velocity field satisfies the condition of incompressibility. Despite that, both models are able to describe only the early stages of neck growth and are not adequate to describe the complete process. Later, Hopper (1984) analysed the coalescence of two equal viscous cylinders by creeping viscous plane flow, and proposed that the evolution of the neck growth of such cylinders can be described using a one parameter family of inverse ellipses of constant area. Lastly, Pokluda et al. (1997) developed a modification of Frenkel's sintering model which describes the complete sintering process of two spherical particles based on the work balance of surface tension and viscous dissipation. In this model, the evolution of the angle of intersection of the two particles $\theta(t)$ with time is obtained as

$$\frac{d\theta(t)}{dt} = \frac{\Gamma}{a_0\eta}\frac{2^{-5/3}cos(\theta(t))sen(\theta(t))\left(2-cos(\theta(t))\right)^{1/3}}{\left(1-cos(\theta(t))\right)\left(1+cos(\theta(t))\right)^{1/3}} \tag{4.21}$$

where a_0 is the initial radius, Γ is the surface tension and η is the viscosity. This model does not take into account the evolution of the particle shape with time, unlike Frenkel's model; however, the variation of the particle radius is considered. Although this model has been used to describe the sintering process during FDM processes (Bellehumeur et al., 2004; Sun et al., 2008), this approach presents important limitations related to the geometry of the filament cross-section. Therefore, in this section, a new model based on the methodology proposed by Pokluda et al. (1997) but considering more realistic geometry, as shown in Figure 2.4, is developed.

As stated previously, Pokluda et al. (1997) model is based on the work balance of surface tension and viscous dissipation. All other forces, including gravity, are neglected. Taking into account the observations made previously, the cross-section can be decomposed into two half-discs and a rectangle. The layer height (H_0) and length (L_0) of each filament are assumed constant during the sintering process, see Figure 4.14.

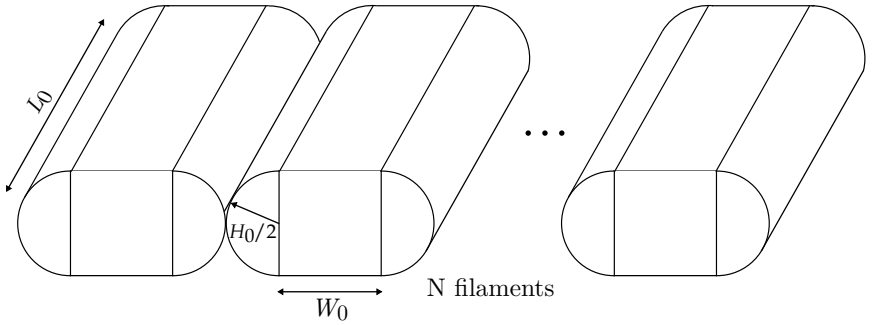

Figure 4.14 Filament sequence of one layer.

As a first approach, the proposed model is idealised as two isolated filaments. Note that, for filaments that are in the centre of the component, the left filament would have undergone a previous sintering process. Although its initial geometry would be different, this aspect is not considered here for simplicity. At initial time $t = 0$, the cross-sectional geometry is composed of two half-discs with a radius equal to $\frac{H_0}{2}$ and a rectangle with an initial width w_0, see Figure 4.15. At this point in time, there is only one contact point between filaments. With the evolution of the process, the centres of the contacting half-discs, move towards the initial contact point O leading to the overlap of both half-discs, where $\theta(t)$ is the angle of the intersection and $X(t)$ the radius of neck. The sintering process is completed when all the mass of the half-discs is transferred to the rectangle part, being $\theta(t)$ equal to $\frac{\pi}{2}$ in that instant.

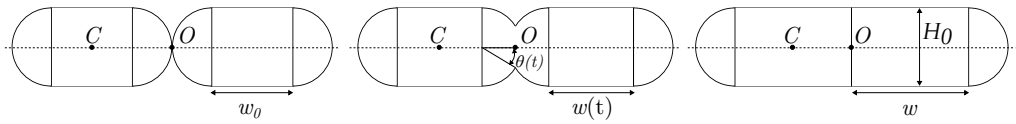

Figure 4.15 Sintering process.

A proper definition of the problem requires to satisfy the conservation of mass during the sintering process. Due to the H_0 and L_0 are assumed constant, the width of the rectangle part, $w(t)$, is assumed to evolve with time. These assumptions are motivated by experimental observations from the mesostructural characterisation developed in Section 3.2. Therefore, assuming constant density, the evolution of $w(t)$ can be obtained from the initial parameters with

$$2\left(\pi\left(\frac{H_0}{2}\right)^2 + H_0 w_0\right) L_0 = 2\left(\pi\left(\frac{H_0}{2}\right)^2 + H_0 w(t) - \frac{(H_0/2)^2}{2}(2\theta(t) - \sin(2\theta(t))\right) L_0 \tag{4.22}$$

$$w(t) = w_0 + \frac{H_0\theta(t)}{4} - \frac{H_0 \sin(2\theta(t))}{8} \tag{4.23}$$

In that case, the part in which sintering takes place is a semicircular segment as shown in Figure 4.16, where its area (A) and perimeter (S) are calculated as

$$\mathrm{A} = \frac{R^2}{2}(2\theta(t) - \sin(2\theta(t))) = \frac{(H_0/2)^2}{2}(2\theta(t) - \sin(2\theta(t))) \tag{4.24}$$

$$\mathrm{S} = R2\theta(t) = \frac{H_0}{2}2\theta(t) \tag{4.25}$$

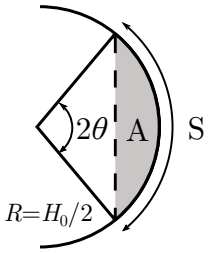

Figure 4.16 Area and length of a circular segment.

Similarly, the total external surface of both filaments is expressed as

$$S(t) = 4w(t)L_0 + 4H_0w(t) + 4\pi\left(\frac{H_0}{2}\right)^2 + 4\pi\frac{H_0}{2}L_0 - \left[4\frac{(H_0/2)^2}{2}(2\theta(t) - \sin(2\theta(t)) + 4\theta(t)\frac{H_0}{2}L_0\right] \tag{4.26}$$

Thus, considering Equation (4.23), the total surface of both filaments varies with $\theta(t)$ as

$$S(t) = 4(L_0 + H_0)w_0 + \left(2\pi - \theta(t) - \frac{1}{2}\sin(2\theta(t))\right)L_0H_0 + \pi{H_0}^2 \tag{4.27}$$

The evolution of the angle of the intersection is obtained from a work balance of surface tension and viscous dissipation, where all the other forces are neglected.

The work of surface tension is defined as

$$W_s = -\Gamma(T_r)\frac{dS}{dt} \tag{4.28}$$

where $\Gamma(T_r)$ is the temperature-dependent coefficient of surface tension. Using the definition of Equation (4.27), the work of surface tension is obtained as

$$W_s = \Gamma H_0L_0\left(cos(2\theta) + 1\right)\frac{d\theta}{dt} \tag{4.29}$$

In continuum mechanics, a Newtonian fluid is a fluid in which the viscous stresses are linearly proportional to the rate of change of its deformation over time and, therefore, the

viscosity η of the fluid does not depend on the stress state and velocity of the flow. The strain rate tensor, which describes how the deformation of a fluid element changes with time, is defined as the gradient of the velocity vector field $\nabla\dot{\mathbf{u}}$. For an incompressible Newtonian fluid, the viscous stress can be related to the strain rate as

$$\boldsymbol{\tau} = \eta(\nabla\dot{\mathbf{u}} + \nabla\dot{\mathbf{u}}^T) \tag{4.30}$$

Then, the work of viscous forces for a Newtonian fluid is expressed as

$$W_v = \iiint_V \nabla\dot{\mathbf{u}} : \boldsymbol{\tau} dV \tag{4.31}$$

where V is the volume of the system. An extensional fluid is a fluid in which the velocity vector can be expressed in the form

$$\dot{u}_x = \dot{e}_1\vec{x}; \dot{u}_y = \dot{e}_2\vec{y}; \dot{u}_z = \dot{e}_3\vec{z} \tag{4.32}$$

in a fixed Cartesian coordinate system (x, y, z), where $\dot{u}_x$, $\dot{u}_y$ and $\dot{u}_z$ are the components of the velocity vector and $\dot{e}_1$, $\dot{e}_2$ and $\dot{e}_2$ are the principal rates of strain (Petrie, 1999). Assuming an extensional flow, the gradient of velocity can be expressed as

$$\nabla\dot{\mathbf{u}} = \begin{bmatrix} \dot{e}_1 & 0 & 0 \\ 0 & \dot{e}_2 & 0 \\ 0 & 0 & \dot{e}_3 \end{bmatrix} \tag{4.33}$$

Note that the deformations in height and length are negligible with respect to deformations in width. Therefore, $\dot{e}_1 \ggg \dot{e}_2$ and $\dot{e}_1 \ggg \dot{e}_3$, with $\dot{e}_1$ representing the equivalent width strain rate. Then, the work of viscous forces reads as

$$W_v = \iiint_V 2\eta(T_r)\dot{e}_1^2 dV \tag{4.34}$$

where the strain rate can be approximated by

$$\dot{e}_1 \approx \frac{\dot{u}_x(C)_t - \dot{u}_x(O)_t}{\overline{OC}_0} = \frac{\frac{d}{dt}\left[\frac{H_0}{2}\cos(\theta(t)) + \frac{w_0}{2} + \frac{H_0\theta(t)}{8} - \frac{H_0\sin(2\theta(t))}{16}\right]}{\frac{H_0}{2} + \frac{w_0}{2}} = \frac{-\frac{H_0}{2}\sin(\theta(t)) + \frac{H_0}{8} - \frac{H_0\cos(2\theta(t))}{8}}{\frac{H_0}{2} + \frac{w_0}{2}}\frac{d\theta(t)}{dt} \tag{4.35}$$

Consequently, the dissipated energy leads to

$$W_v = 4\eta(T_r)\left(\pi\left(\frac{H_0}{2}\right)^2 + H_0 w_0\right) L_0 \left(\frac{-\frac{H_0}{2}\sin(\theta(t)) + \frac{H_0}{8} - \frac{H_0\cos(2\theta(t))}{8}}{\frac{H_0}{2} + \frac{w_0}{2}}\right)^2 \frac{d^2\theta(t)}{dt^2} \tag{4.36}$$

The evolution of $\theta(t)$ is obtained by equating the work of surface tension to the viscous dissipation. This derivation of $\theta(t)$ assumes that the variation of the angle of the intersection with time is always positive, so that

$$\frac{d\theta(t)}{dt} = \frac{\Gamma(T_r)H_0}{4\eta(T_r)} \frac{(cos(2\theta(t))+1)}{\left(\pi\left(\frac{H_0}{2}\right)^2+H_0 w_0\right)\left(\frac{-\frac{H_0}{2}\sin(\theta(t))+\frac{H_0}{8}-\frac{H_0\cos(2\theta(t))}{8}}{\frac{H_0}{2}+\frac{w_0}{2}}\right)^2} = \frac{\Gamma(T_r)H_0}{4\eta(T_r)} \frac{2cos(\theta(t))^2}{\left(\pi\left(\frac{H_0}{2}\right)^2+H_0 w_0\right)\left(\frac{-\frac{H_0}{2}\sin(\theta(t))+\frac{H_0}{8}-\frac{H_0\cos(2\theta(t))}{8}}{\frac{H_0}{2}+\frac{w_0}{2}}\right)^2} \quad (4.37)$$

where T_r is the temperature of the filament that evolves with time. Once the evolution of sintering angle is known, the evolution of the neck radius $y(t)$ with time can be obtained as

$$y(t) = \frac{H_0}{2}\sin(\theta(t)) \quad (4.38)$$

4.4.1 Implementation

To obtain a solution for $\theta(t)$, it is necessary to solve numerically the ordinary differential Equation (4.37). MATLAB has different ordinary differential equation solver functions. ODE45 function is based on the integration method Runge-Kutta (RKF45); however, this integration method uses a variable step size and does not allow for the use of a fixed step size. Since both surface tension and viscosity are temperature-dependent properties and, therefore, depend on the temperature profile obtained from the thermal model, the step size of the sintering model must be the same as the used in the thermal model. Therefore, an algorithm using the RKF45 method has been implemented in MATLAB. This is an adaptive method proposed by Fehlberg (1970) that permits to obtain an error estimation and, therefore, is used to control the step size. To this end, two RK methods of different orders to go from (x_n, y_n) to (x_{n+1}, y_{n+1}) are used (Kreyszig, 2010). The difference between the computed y values at x_{n+1} gives an error estimation. Moreover, the two formulas need only six function evaluations per step.

The fifth-order RKF method is given by

$$y_{n+1} = y_n + \gamma_1 k_1 + ... + \gamma_6 k_6 \quad (4.39)$$

with the coefficient vector $\gamma = \left[\frac{16}{135} \quad 0 \quad \frac{6656}{12825} \quad \frac{28561}{56430} \quad -\frac{9}{50} \quad \frac{2}{55}\right]$. On the other hand, the fourth-order RK method is given by

$$y_{n+1}{}^* = y_n + \gamma_1{}^* k_1 + ... + \gamma_5{}^* k_5 \quad (4.40)$$

with the coefficient vector $\gamma^* = \left[\frac{25}{216} \quad 0 \quad \frac{1408}{2565} \quad \frac{2197}{4104} \quad -\frac{1}{5}\right]$.

Taking into account both methods, the error estimation is

$$\epsilon_{n+1} \approx y_{n+1} - {y_{n+1}}^* = \frac{1}{360}k_1 - \frac{128}{4275}k_3 - \frac{2197}{75240}k_4 + \frac{1}{50}k_5 + \frac{2}{55}k_6 \tag{4.41}$$

which permits to find the step size for which the convergence of the solution is obtained. The different function evaluations k_i, which are common to both methods, are

$$\begin{aligned} k_1 &= hf(x_n, y_n) \\ k_2 &= hf(x_n + \frac{1}{4}h, y_n + \frac{1}{4}k_1) \\ k_3 &= hf(x_n + \frac{3}{8}h, y_n + \frac{3}{32}k_1 + \frac{9}{32}k_2) \\ k_4 &= hf(x_n + \frac{12}{13}h, y_n + \frac{1932}{2197}k_1 - \frac{7200}{2197}k_2 + \frac{7296}{2197}k_3) \\ k_5 &= hf(x_n + h, y_n + \frac{439}{216}k_1 - 8k_2 + \frac{3680}{513}k_3 - \frac{845}{4140}k_4) \\ k_6 &= hf(x_n + \frac{1}{2}h, y_n - \frac{8}{27}k_1 + 2k_2 - \frac{3544}{2565}k_3 + \frac{81859}{4140}k_4 - \frac{11}{40}k_5) \end{aligned} \tag{4.42}$$

4.4.2 Results and discussion

In this section, the prediction of the evolution of the neck radius is obtained with the new proposed model. Sintering is a temperature-dependent process since both viscosity and surface tension values depend on temperature. During the sintering process of FDM components, these parameters vary as the temperature of the filaments. However, for this example, isothermal conditions are assumed at a temperature of 240 °C. The value of the different parameters are summarised in Table 4.4. In addition, the predictions in terms of the angle of intersection and diameter of the neck are compared with the predictions from the model proposed by Pokluda et al. (1997) for $a_0 = H_0/2$, see Figure 4.17.

Table 4.4 Material properties for ABS and 3D printing parameters (Bellehumeur et al., 2004).

Property	Value
Layer height	0.3 mm
Line width	0.4 mm
Viscosity at 240 °C (η_0)	5100 Pa·s
Surface tension at 240 °C (Γ_0)	0.029 N/m

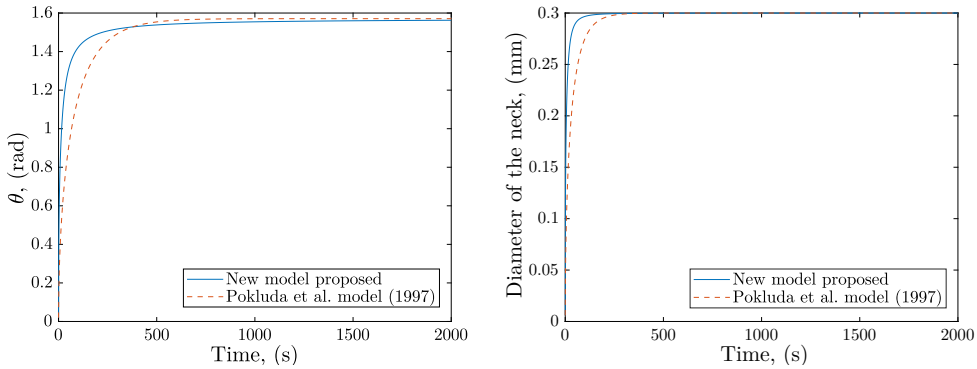

(a) *(b)*

Figure 4.17 Comparison between new sintering model developed in this thesis and Pokluda et al. (1997) model predictions: (a) evolution of angle of the intersection and (b) evolution of the diameter of the neck.

Comparing both models, shorter times are needed with the model proposed by Pokluda et al. (1997) to reach complete sintering. However, the evolution of the angle of intersection and, therefore, the diameter of the neck, is faster in the first stages of the sintering process for the model proposed in this dissertation. Due to the deposited filament reaches a temperature below T_g in a shorter period of time, Pokluda et al. (1997) model can overestimate the sintering neck for FDM processes. Finally, the evolution of the width of the rectangle part of the filament cross-section is obtained through Equation (4.23). Considering that, after complete sintering, the mass of one of the half-disc goes to the rectangle part, it can be proved that the final volume is equal to the initial one, indicating the consistency of the model.

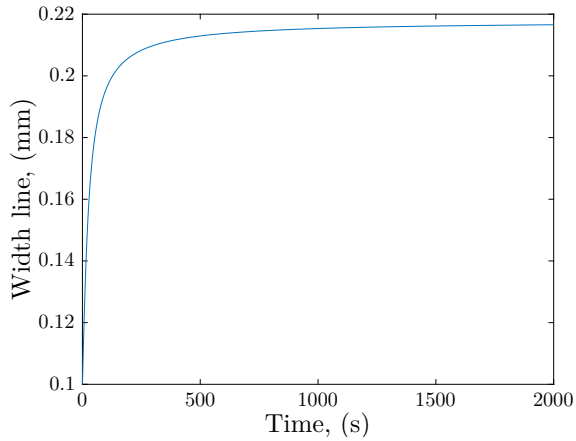

Figure 4.18 Evolution of width (w) during sintering process.

4.5 Healing process during 3D printing

Polymer healing refers to the intermolecular diffusion across the interface of two thermoplastics in intimate contact. Temperatures above glass transition for amorphous polymers, or the melting point for semi-crystalline polymers, are needed to decrease the viscosity and enhance the movement of polymer molecules (Yang and Pitchumani, 2002). Therefore, healing is a temperature-dependent process.

The reptation theory has been widely used to describe the healing process under isothermal conditions of amorphous polymers (de Gennes, 1971). Taking an individual linear polymer chain with an initial length L confined in a tube, the chain moves in a Brownian motion manner. This tube describes the topological constraint of the lateral motion of the chain due to the engagement with neighbouring chains (Butler et al., 1998). After a given period of time, the chain ends escaping from the tube, form minor chains with a length l. This length of the minor chain increases until reaching L at the reptation time when the ultimate bond strength σ_∞ is achieved (Yang and Pitchumani, 2002), see Figure 4.19.

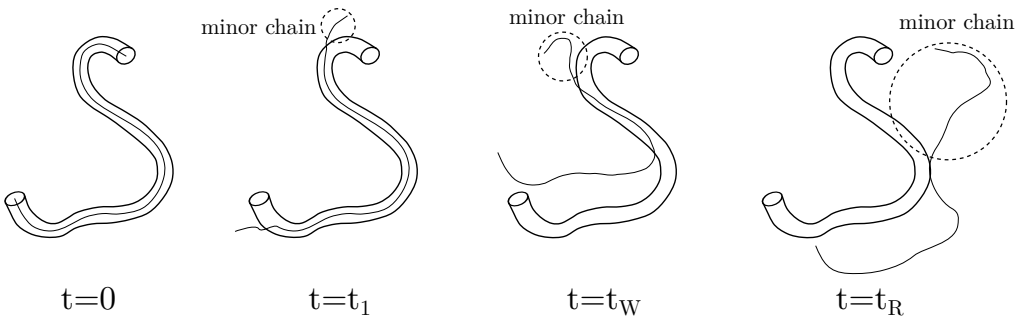

Figure 4.19 Reptation movement, adapted from Yang and Pitchumani (2002)

If instead of an individual chain, we consider all the chains, after the reptation time the interpenetration and entanglement of all of them would be reached (Yang and Pitchumani, 2002). In that instant, the molecular configuration at the interface is identical to that of the bulk polymer and, therefore, the same mechanical properties as well. Thus, the degree of healing achieved can be defined as the ratio of the instantaneous interfacial bond strength (σ) to the ultimate bond strength (σ_∞) as

$$D_h(t) = \frac{\sigma}{\sigma_\infty} = \frac{\chi}{\chi_\infty} = \left(\frac{l}{L}\right)^{1/2} \tag{4.43}$$

where χ is the interpenetration distance with which the chains move across the interface and is related to the minor chain length as $\chi \sim \sqrt{l}$ (Yang and Pitchumani, 2002).

Moreover, under isothermal conditions, the evolution of l can be expressed as

$$\frac{l}{L} = \left(\frac{t}{t_R}\right)^{1/2} \tag{4.44}$$

Nevertheless, Equation (4.43) is only valid for low molecular weights (Wool and O'Connor, 1981; Wool et al., 1989). For the range $M > 8M_C$, where M_C is the critical entanglement molecular weight, the maximum bond strength is achieved at $t_W < t_\infty$, being t_W the welding time (Yang and Pitchumani, 2002). Therefore, the degree of healing can be expressed in a more general way as

$$D_h(t) = \frac{\sigma}{\sigma_\infty} = \frac{\chi}{\chi_W} = \left(\frac{l}{L_W}\right)^{1/2} = \left(\frac{t}{t_W}\right)^{1/4} \tag{4.45}$$

Based on the polymer reptation principle presented above and considering the influence of time and temperature, Yang and Pitchumani (2002) proposed a new model for non-isothermal conditions, where the evolution of healing is expressed as

$$D_h(t) = \left[\int_0^t \frac{1}{t_w(T)}\,\mathrm{d}t\right]^{1/4} \tag{4.46}$$

where t_w is the welding time that can be obtained starting from experimental results and fitted using an Arrhenius relationship with temperature. Note that these previous equations describe the process of intermolecular diffusion by assuming that complete intimate contact is already achieved at the interface (Yang and Pitchumani, 2002).

4.5.1 Implementation

The healing model for non-isothermal conditions proposed by (Yang and Pitchumani, 2002) is implemented in MATLAB in order to solve explicitly de degree of healing in each instant as

$$D_{(i+1)} = \left({D_{(i)}}^4 + \frac{1}{tw}(t_{(i+1)} - t_{(i)})\right)^{(1/4)} \tag{4.47}$$

4.5.2 Results and discussion

In this subsection, the evolution of the degree of healing with time is analysed for ABS. Rodriguez et al. (1999) obtained the relationship of the welding time for ABS from experimental tests, where FDM components were subjected to an annealing process under isothermal conditions to increase the bond strength, as

$$t_w = 1.08 \times 10^{-47} \exp\left(\frac{Q_d}{RT}\right) \tag{4.48}$$

where Q_d is the energy of activation (388.7 kJ/mol), R is the universal gas constant and T is the interface temperature. However, it should be noted that the Equation (4.48) was obtained for a specific material, ABS P400, and under a range of temperatures from 118 °C to 134 °C. Assuming a constant interface temperature of 130 °C, the degree of healing versus time is shown in Figure 4.20.

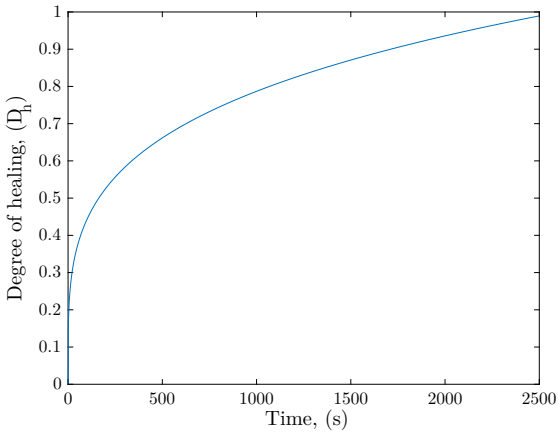

Figure 4.20 Evolution of degree of healing versus time.

After 2500 s, the maximum degree of healing is achieved. However, it is necessary to know the activation energy value for a wide temperature range in order to apply this model to FDM process.

4.6 Conclusions

In this chapter, a complete analysis of the thermodynamics of the 3D printing process is presented. From the mesostructural analysis developed in Section 3.2, it was observed that FMD components are formed by polymeric filaments bonded. The quality of the bond, in terms of neck growth and molecular diffusion, determines the void density as well as the mechanical properties of the bond and, therefore, the final mechanical response of the FDM component. Regarding the bonding phenomenon, this is driven by the thermal energy of the semi-molten material.

Due to the importance of the temperature in the printing process, a new model for the prediction of the evolution of the filament temperature is implemented, based on the one proposed by Costa et al. (2017). Different deposition strategies are analysed where little differences are observed between them, considering that a non relevant factor. Moreover, results for two-layer components show that filaments from the first layer maintain a higher temperature for a longer period than the subsequent layers. This fact is due to the difference in temperature between the platform and the environment.

Moreover, from the micrographs of the cross-section, it has been observed that top regions of the filaments are flatter than the bottom regions. Thus, an analysis of the intra-fibre heat transfer has been developed using the finite difference method. The results show an asymmetric distribution of the temperature inside the filament, which is the responsible of this flatting at the top of the filaments.

On the other hand, from the analytical expression for the estimation of the void density, the need arises for the development of models that allow for estimating the final geometry of the filaments after the bonding process. In this regard, starting from the sintering model proposed by Pokluda et al. (1997), in which the sintering of two spherical particles is described, a new sintering model is proposed with a geometry in accordance with the geometry observed in FDM. This model predicts a faster evolution of the angle of intersection in the first stages of the sintering process compared with the Pokluda et al. (1997) model.

Finally, the degree of molecular diffusion has been analysed through the healing model for non-isothermal conditions proposed by (Yang and Pitchumani, 2002). However, there is an absence of data in terms of energy activation for polymers employed in FDM for a wide range of temperatures, which requires the development of new studies to complete a molecular diffusion analysis in FDM.

5 Modelling of the manufacturing process and prediction of mechanical properties

As stated previously, AM technologies provide new opportunities for the manufacturing of components with customisable geometries and mechanical properties. In this doctoral thesis, this issue is approached for a specific AM technique, FDM. Previous chapters have revealed that FDM allows for customisable mechanical properties by mainly controlling the void density and filaments orientation. In order to deepen in this issue, analytical expressions are proposed in Chapter 3 providing tools for the prediction of void density and posterior mechanical properties.

On the other hand, in Chapter 4, a thermodynamic analysis of the 3D printing process is approached. In that chapter, a new sintering model is developed to simulate the bond formation process between filaments, providing the final geometry of the mesostructure. As sintering is a temperature dependent process, one of its inputs is the evolution of the filament temperature during the 3D printing process. In this regard, a thermal model to predict the temperature evolution of filaments is proposed.

In this chapter, the thermal and sintering models and the analytical expressions are combined providing a methodology that allows for the prediction of the final properties of FDM polymers. To this end, the outline of the chapter is a follows: in Section 5.1, the proposed methodology is introduced; in Section 5.2, this methodology is used to predict the mechanical properties of specimens with the same geometry and printing parameters as those used experimentally. Moreover, with the aim of showing the potential of the methodology in the optimisation of FDM components, a parametric study by using end-to-end simulations is carried out, analysing the effects of different manufacturing parameters. Finally, the conclusions of the chapter are presented in Section 5.3.

5.1 Introduction

The analytical expressions proposed for the prediction of the mechanical properties (Equations (3.6) and (3.7)) are fed by the material properties, provided by the filament

supplier, and the void density, which can be taken from the analytical expression for the void density prediction (Equation (3.5)). On the other hand, this latter expression is fed by the final geometry of the filaments after bonding process. In order to avoid the need for experimental measurements, the sintering model developed in Chapter 4 can be used to predict the final geometry of the filaments. Moreover, the sintering model needs to take as input the evolution of filament temperature during the complete printing process. In this regard, the combination of the thermal and sintering models provides a new two-stage model for the bonding simulation.

This two-stage thermal and sintering model together with the analytical expressions allows to create a methodology for the prediction of the mechanical properties and mesostructure of FDM polymers as shown in Figure 5.1. Thus, it is possible to estimate the final properties of taking only as input data: printing parameters and material properties.

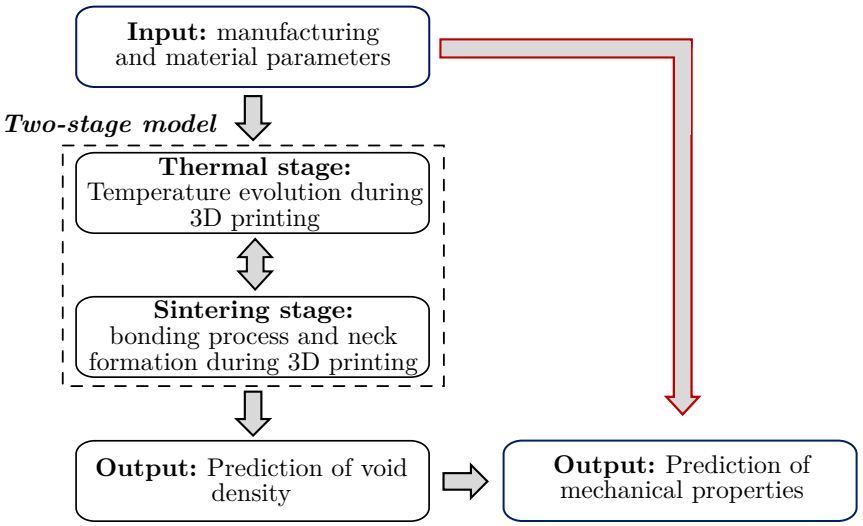

Figure 5.1 Procedure to predict the mechanical properties of FDM components.

5.1.1 Thermal-sintering coupling

As observed in Figure 5.1, the thermal and sintering stages are fully coupled as follows: (*i*) the thermal part of the model calculates the temperature of the filaments ($T_r(t)$) taking into account the contacts between them and with the support; (*ii*) this calculated temperature is used by the sintering part of the model to compute the sintering necks between filament segments ($y(t)$); (*iii*) the computed sintering necks are used to determine the updated contacts between filaments and support ($\lambda_i(t)$) in the thermal part of the model.

Note that adjacent filaments are at different temperatures. For the sintering process, the temperature of the filament being deposited can be considered to play the major role

over the adjacent filament. Thus, the perimeter of the filament segments deposited is calculated as

$$P(x,t) = 2w(t)+\pi H_0+H_0\sin(\theta(x,t))+H_0\sin(\theta(contact_4,t))-H_0\theta(x,t)-H_0\theta(contact_4,t) \tag{5.1}$$

where $\theta(x,t)$ is the angle of sintering considering the temperature evolution of the filaments, and $\theta(contact_4,t)$ is the angle of sintering considering the temperature evolution of the adjacent filaments 4, according to Figure 4.2.

Following the same figure, the fraction contact parameter λ_i can be expressed as

$$\lambda_{1,3} = \frac{w(x,t)}{P(x,t)} \tag{5.2a}$$

$$\lambda_2 = \frac{H_0\sin(\theta(x,t))}{P(x,t)} \tag{5.2b}$$

$$\lambda_4 = \frac{H_0\sin(\theta(contact_4,t))}{P(x,t)} \tag{5.2c}$$

One simplification of the model considers the fraction contact perimeter as a constant, allowing to significantly reduce computational costs. These values can be estimated from the full model predictions and agree well with experimental observations (SEM images). With the aim of evaluating the suitability of this simplification, we perform a comparative study of the simulations provided by this approach and the results provided by the full model. The results of the comparison are shown in Figure 5.2 and Table 5.1. Although the comparison between temperature evolution shows slight differences, note that the sintering process takes place at temperatures above T_g, being the early stage of the cooling process where most of the bonding occurs. We can observe differences lower than 2% between both approaches in terms of angle of intersection. Therefore, we assume this simplification hereafter to avoid unnecessary high computational cost.

Table 5.1 Comparison between both approaches.

Model	Layer height (mm)	Angle of the intersection (θ)
$\lambda_i = const$	0.1	1.0852
$\lambda_i(t)$	0.1	1.0758
$\lambda_i = const$	0.2	0.9352
$\lambda_i(t)$	0.2	0.9434
$\lambda_i = const$	0.3	0.7358
$\lambda_i(t)$	0.3	0.7501

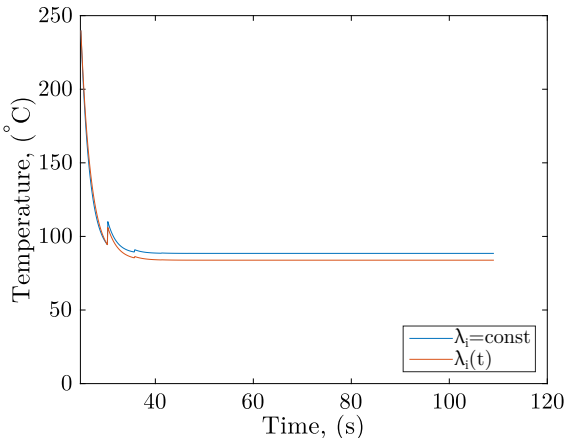

Figure 5.2 Comparison between temperature evolution with both approaches for a layer height of 0.3 mm.

5.2 Results and discussion

Once the methodology for the prediction of the mesostructural and mechanical properties has been proposed, this is used to analyse its suitability to predict the mechanical properties in this section. Therefore, first we predict the mechanical properties of components with the same characteristics that those used in the experimental characterisation Section 3.3, comparing the predictions with experimental results. Moreover, a parametric study is carried out to show the potential to find the optimal printing parameters that give specific mechanical properties depending on the final application.

5.2.1 Prediction of the mesostructural and mechanical properties through an end-to-end simulation

In this section, the complete methodology proposed above is used to predict the final characteristics of longitudinal specimens with the same dimensions as those used in the experimental characterization. These are made with one, two and three layers of materials and three different layer heights: 0.1, 0.2 and 0.3 mm. To this end, first, specific material and printing parameters are taken as inputs for the thermal model, in turn providing the temperature evolution of each filament. Although the room temperature is set to 30 °C, the heated bed and the extruder lead to a higher envelope temperature around the specimen. Therefore, a temperature of 75 °C is set according to experimental records from the printing area (not reported). The fractions of perimeter λ_i are estimated using microscope images for each layer height. In the case of a layer height of 0.1 mm, fractions of perimeter are estimated as $\lambda_{1-3} = 0.3$ and $\lambda_{2-4} = 0.1$. For a layer height of 0.2 mm, $\lambda_{1-3} = 0.25$ and $\lambda_{2-4} = 0.15$. For a layer height of 0.3 mm, $\lambda_i = 0.15$ is

estimated for all contacts. A filament segment length dx of 10 mm is set. The rest of the material and printing parameters are summarised in Table 4.2.

For the prediction of the sintering process, both viscosity and surface tension values must be defined as a function of the temperature. In this regard, Sun et al. (2008) proposed the following expression for the viscosity of the ABS: $\eta = \eta_0 e^{[-b(T_r - T_{ref})]}$, where b is a model parameter. In the same way, the surface tension decreases with the temperature as $\Gamma = \Gamma_0 - \frac{\Delta\Gamma}{\Delta T}(T_r - T_{ref})$ (Sun et al., 2008). However, these properties for the specific ABS tested in this thesis are not available in the literature, but those of ABS P400 are. While the recommended extrusion temperature of the ABS used in this thesis is given by the supplier as 240 °C, the extrusion temperature for the ABS P400 is 270 °C (Sun et al., 2008). These recommended extrusion temperature is determined by an optimal viscosity that favours the polymer flow during the 3D printing process. Considering the viscosity a variable determining the optimal printing conditions (that must be approximately the same for both ABS filaments), a value of 950.5 Pa·s is estimated for the ABS tested at 240 °C (η_0). All the properties are summarised in Table 5.2.

Table 5.2 Material properties of ABS (Sun et al., 2008).

Property	Value
Viscosity at 240 °C (η_0)	5100 Pa·s
Model parameter (b)	0.056
Surface tension at 240 °C (Γ_0)	0.029 N/m
Temperature dependence $\Delta\Gamma/\Delta T$	-3.45·10^{-3} N/m°C
Reference temperature (T_{ref})	240 °C

Table 5.3 compared the predictions in terms of neck radius and void density of two-layer specimens with the experimental data obtained from the mesostructural characterisation. The differences observed between model predictions and experimental measurements can be explained by the assumptions considered. In addition, neither model temperature nor model sintering account for the creep deformation under the effect of gravity or the continued downward pressure from the extruder during the manufacturing process (Sun et al., 2008).

Table 5.3 Comparison of void density prediction and digitised image results.

	Digitised image results		Model predictions	
Layer height (mm)	0.2	0.3	0.2	0.3
Dimensionless neck radius	0.812	0.692	0.728	0.629
Void density (%)	2.07	4.75	3.31	7.56

Moreover, the same procedure is used to predict the void density of different configurations shown in Table 5.4. Lower void densities are obtained when the number of layers increases. This can be explained by the fact that higher temperature gradients are produced towards the bottom part when the number of layers increases. This results in a larger neck between filaments of the first layer.

Table 5.4 Experimental results of specimens with a longitudinal raster orientation.

Number of layers	Layer height (mm)	Void density (%)
1	0.1	0.84
	0.2	3.81
	0.3	7.26
2	0.1	0.18
	0.2	2.87
	0.3	6.83
3	0.1	0.21
	0.2	2.52
	0.3	6.61

Finally, the mechanical properties can be predicted from the void density estimations. These results (model predictions) are compared with the experimental data for both raster orientations in Figures 5.3 and 5.4. The results show that the methodology is able to predict the different trends as a function of the void density and layer height with a maximum error of 14% between model predictions and experimental results. The only case of study with a larger error than 14% is the prediction of the elastic modulus for the longitudinal three-0.1 mm-layer specimen. This result can be explained by an overestimation of the void density. Apart from this case, the mechanical properties predictions are in excellent agreement with the experimental results.

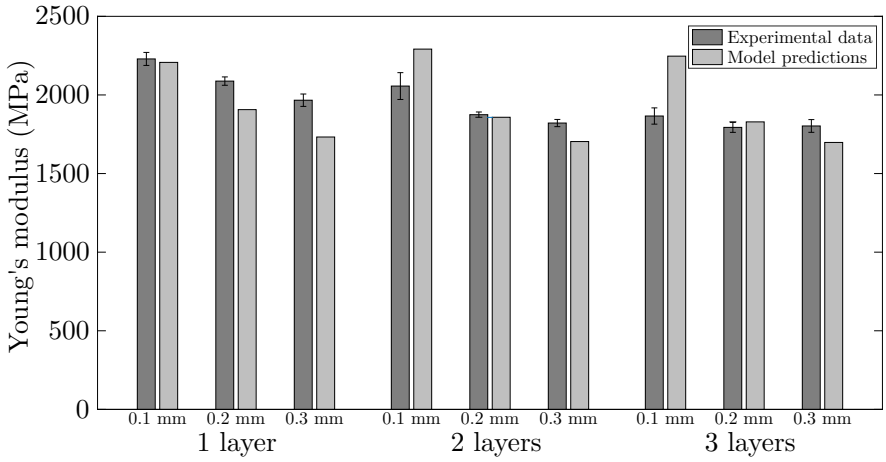

(a)

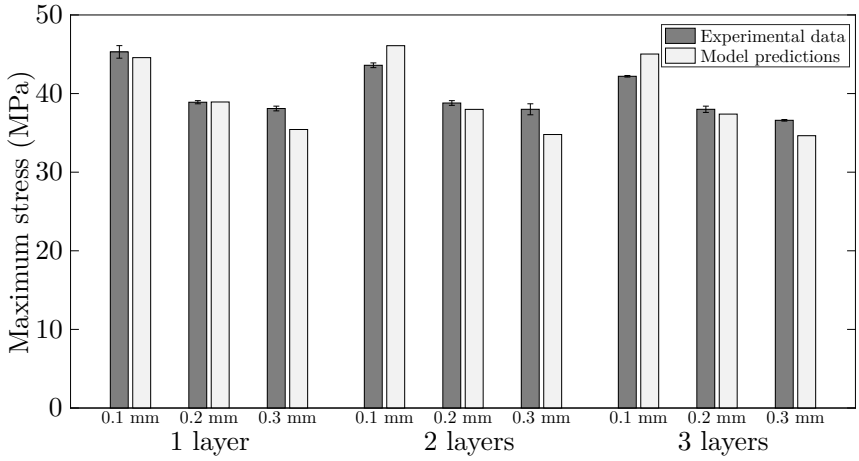

(b)

Figure 5.3 Comparison between experimental mechanical properties (with error bars) and predictions for longitudinal specimens.

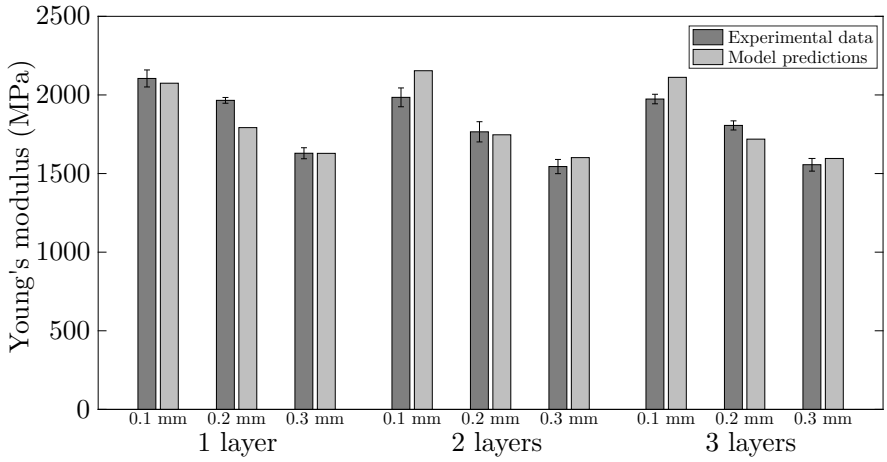

(a)

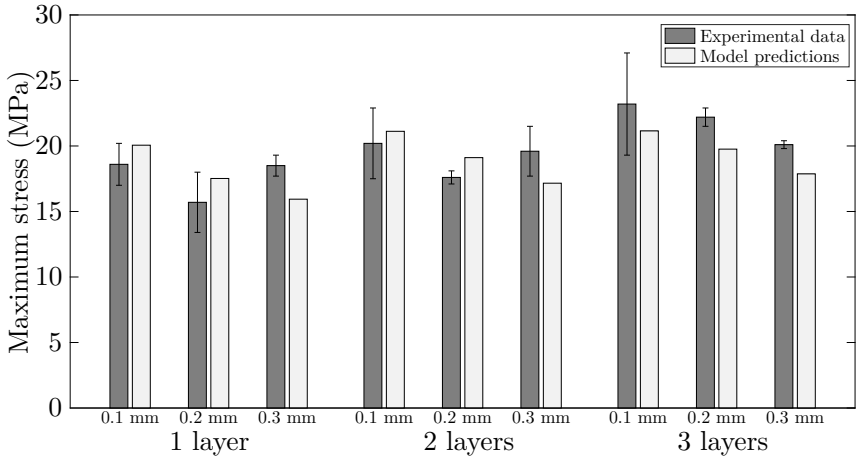

(b)

Figure 5.4 Comparison between experimental mechanical properties (with error bars) and predictions for transversal specimens.

5.2.2 Parametric study of the influence of printing and process parameters

The procedure proposed in this chapter provided a powerful tool to find the optimal parameters that give specific mechanical properties depending on the final requirements. It is consequently possible to find the optimal parameters to obtain a specific set of mechanical properties depending on the final application. This can be done by making use of a parametric study of the influence of printing and process parameters on the mesostructural and mechanical properties of the printed component. Therefore, in this subsection, a parametric study is presented where the influence of some printing and

process parameters is analysed: layer height, printing speed, environment and support temperature.

The reference parameters are chosen to be the ones used in the previous subsection for longitudinal two-0.3 mm-layer specimens. The results in terms of void density are shown in Figure 5.5.

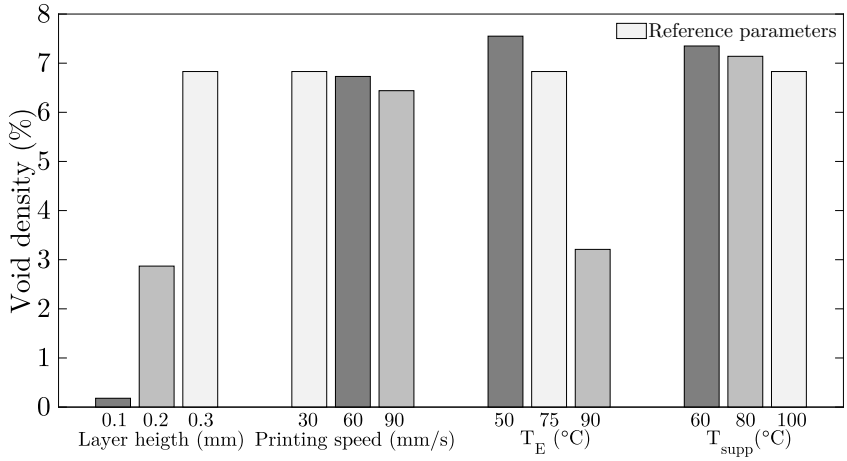

Figure 5.5 Influence of printing and process parameters in the void density.

Observing these predictions, the parameter with the greatest influence is the layer height, decreasing the void density by more than 97% when the layer height goes from 0.3 to 0.1 mm. In addition, higher environmental or support temperatures lead to lower void densities. In this regard, note that for an environmental temperature of 90 °C, near the support temperature (100 °C), the void density decreases by up to 53%. Finally, when the printing speed is increased, the percentage of void density slightly decreases. However, although the manufacturing times and void density decrease, a loss of dimensional accuracy and surface quality is expected when the printing speed is increased (Wang et al., 2019).

The results in terms of mechanical properties are shown in Figure 5.6. As all the cases simulated have two layers, higher mechanical properties are obtained for those with lower void density. Thus, considering the reference layer height (0.3 mm), the elastic modulus and the maximum stress, both increase by 9% in average for a decrease of layer height to 0.2 mm, and 33% in average for a decrease of layer height to 0.1 mm. These tendencies are in qualitative agreement with the experimental results (see Table 3.5) where the elastic modulus and maximum stress increase by 3% and 2%, respectively, when the layer height changes from 0.3 mm to 0.2 mm, and by 13% and 14% when the layer height changes from 0.3 mm to 0.1 mm. Moreover, following the same tendency as for the void density, the mechanical properties increase by up to 7% for an environmental temperature of 90 °C.

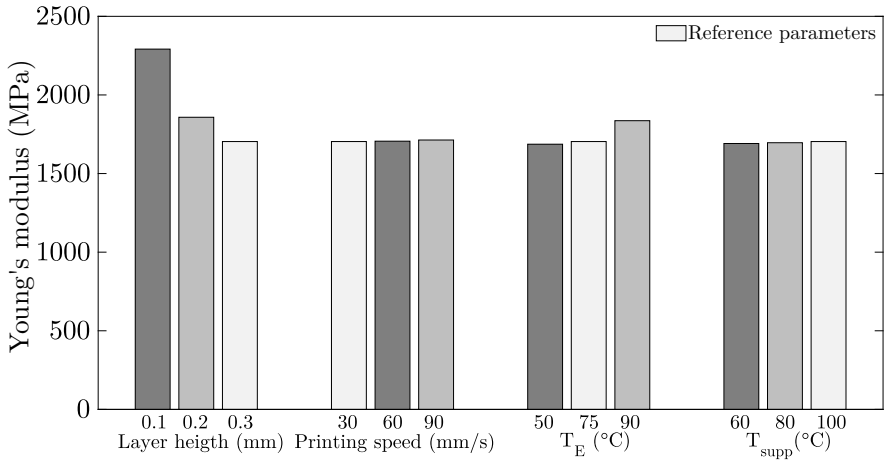

(a)

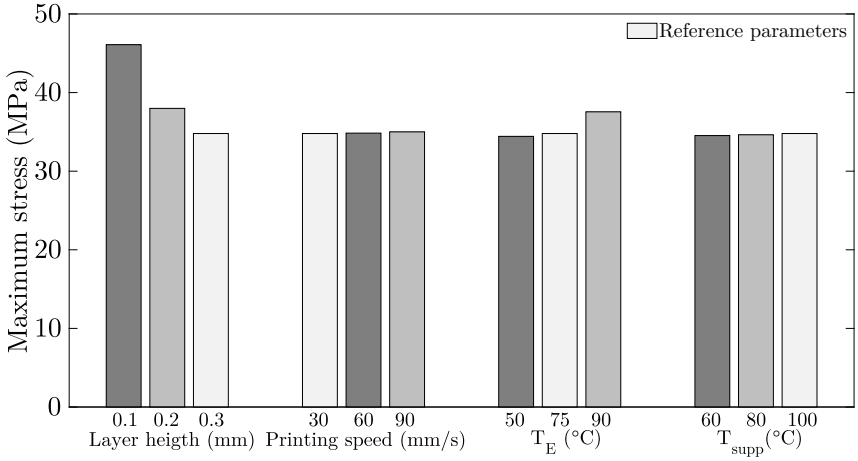

(b)

Figure 5.6 Influence of printing and process parameters in the mechanical properties.

5.3 Conclusions

In this chapter, a new modelling methodology is proposed to predict the mechanical properties and mesostructural characteristics of FDM polymers, taking as inputs the printing and material parameters. Thus, the procedure is formed by four stages. The two first stages are composed by a two-stage thermal and sintering model with which the final geometry of the filaments after bonding is obtained. These outputs feed the third stage, where the analytical expression for the void density prediction is used. Finally, the results of the void density predictions along with the material properties are used to predict the elastic modulus and maximum stress.

The modelling predictions by this procedure are compared with the experimental results obtained in Chapter 3, from the mechanical and mesostructural characterisation. Although results show some differences, especially in terms of void density, the combination of the different tools allows to predict the tendencies as a function of the different printing parameters (layer height, raster orientation and number of layers), with a maximum error of 14% in terms of mechanical properties.

Moreover, a parametric study is conducted with the aim of showing the potential of the proposed modelling approach to optimise FDM components. The influence of four printing or manufacturing parameters is approached: layer height, printing speed, environment and support temperature. The results highlight the layer height and environment temperature as ones of the most relevant manufacturing parameters, being the former the most critical with increments by up to 33% when the layer height changes from 0.3 to 0.1 mm.

6 Anisotropic viscous-hyperelastic constitutive model for FDM polymers

The experimental observations presented in previous chapters have revealed that the mechanical behaviour of FDM polymers is influenced by the 3D printing parameters such as layer height, the number of 3D printed layers or printing temperatures.

These parameters determine the porosity (void density) of the final structure strongly influencing the mechanical performance. Moreover, these components present mechanical anisotropies arising from the 3D printing process due to the filament deposition orientation and porosity distribution. In addition, the nature of thermoplastic polymers is complex and viscoelastic and viscoplastic behaviours play a relevant role in their overall mechanical response. All these considerations together make the constitutive modelling of FDM thermoplastic polymers very challenging.

In this chapter, a hyperlastic constitutive model is developed to describe the mechanical behaviour of FDM thermoplastics. This model is developed for finite deformations within a thermodynamically consistent framework and accounts for: nonlinear response; anisotropic hyperelasticity related to a transversely isotropic distribution of porous; strain rate dependency; and softening 3D printing processing. Some of the previous dependencies can be directly linked to the 3D printing parameters used during the manufacturing process.

The parameters of the constitutive model have been identified for FDM ABS from the experimental data presented in Chapter 3. Moreover, in order to ensure the suitability of the model to reproduce adequately the mechanical behaviour of FDM thermoplastics, this is used to predict the response of FDM ABS manufactured with different printing parameters and under different loading conditions.

The list of symbols used in this chapter is provided in Table 6.1.

Table 6.1 Nomenclature used for the constitutive formulation.

$\Omega_0, \tilde{\Omega}, \bar{\tilde{\Omega}}, \Omega$	Initial, dilated, dilated relaxed and current configurations
Ψ	Helmholtz free-energy function
e_0	Specific internal energy per unit volume in Ω_0
η_0	Specific entropy per unit volume in Ω_0
θ_0	Reference temperature
$\mathbf{Q}$	Heat flux per unit volume in Ω_0
R	Heat source per unit volume in Ω_0
$\mathbf{a}_0$	FDM filament orientation
$\mathbf{I}$	Identity second-order tensor
$\mathbf{F}$	Deformation gradient
$\mathbf{F_E}, \mathbf{F_V}, \mathbf{F_P}$	Elastic, viscoelastic and viscoplastic deformation gradients
$\mathbf{C}$	Right Cauchy-Green strain tensor
$\mathbf{B}$	Left Cauchy-Green strain deformation
I_i	Principal invariants of $\mathbf{C}$
$\mathbf{l}$	Velocity gradient in Ω
$\mathbf{l_E}$	Elastic velocity gradient in Ω
$\bar{\mathbf{L}}_\mathbf{V}$	Viscoelastic velocity gradient in $\bar{\Omega}$
$\bar{\tilde{\mathbf{L}}}_\mathbf{P}$	Viscoplastic velocity gradient in $\bar{\tilde{\Omega}}$
$\mathbf{N_p}$	Direction tensor of the plastic flow
$\boldsymbol{\sigma}$	Cauchy stress tensor
$\boldsymbol{\sigma_E}, \boldsymbol{\sigma_V}, \boldsymbol{\sigma_P}$	Elastic, viscoelastic and viscoplastic Cauchy stress tensor
$\mathbf{P}$	First Piola-Kirchhoff stress tensor
$\mathbf{S}$	Second Piola-Kirchhoff stress tensor
J	Jacobian
ζ	Softening variable
μ_m	Matrix shear modulus
v_m, v_f	Initial matrix and voids volume fractions
n	Shear modulus porosity-sensitivity parameter
ζ_∞	Dimensionless maximum softening
α	Phenomenological softening parameter
ι	Softening saturation parameter
η	Viscosity
q_1, q_2	Material parameters of the yield function
σ_{kk}	Transverse hydrostatic stress
σ_{eqv}	Equivalent von Mises stress
σ_y	Yield stress
σ_s	Saturation stress
H	Hardening/softening parameter
$\bar{\varepsilon}_p$	Equivalent plastic strain
$\dot{\gamma}_p$	Viscoplastic multiplier
$\dot{\varepsilon}_0$	Reference strain rate
C	Rate-sensitivity parameter

6.1 Description of the constitutive model

Appendix A introduces the basic fundamentals of hyperelastic constitutive modelling taken as a basis for this section.

6.1.1 Rheological model

From the experimental results presented in Section 3.3, it can be observed that FDM thermoplastics present a viscoelastic-viscoplastic anisotropic behaviour. Based on these results, the rheological model is composed of a purely elastic anisotropic spring (E) followed by two dashpots, see Figure 6.1. The former (V) accounts for viscoelastic dependencies while the second one (P), which is in parallel with a friction element, accounts for viscoplastic contributions. The friction element represents a yield function controlling the plastic flow activation.

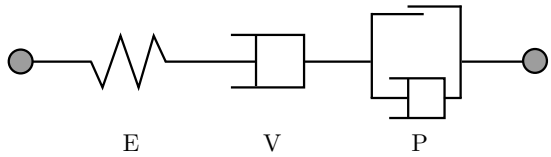

Figure 6.1 Rheological scheme of the proposed constitutive.

According to the rheological model, the stress is equal in the three components and equal to the total stress

$$\boldsymbol{\sigma} = \boldsymbol{\sigma}_{\mathbf{E}} = \boldsymbol{\sigma}_{\mathbf{V}} = \boldsymbol{\sigma}_{\mathbf{P}} \tag{6.1}$$

6.1.2 Kinematics

The finite deformation kinematics is defined by four configurations going from an initial reference configuration Ω_0 to a current configuration Ω, see Figure 6.2. Two additional intermediate configurations have been added. The former refers to as a dilated configuration $\bar{\Omega}$ in which only viscoplastic deformations are accounted for, while the second one refers to as a dilated relaxed configuration $\bar{\bar{\Omega}}$ in which both viscoelastic and viscoplastic deformations are considered. Therefore, the total deformation gradient can be multiplicatively decomposed as

$$\mathbf{F} = \mathbf{F}_{\mathbf{E}}\mathbf{F}_{\mathbf{V}}\mathbf{F}_{\mathbf{P}} \tag{6.2}$$

where $\mathbf{F}_{\mathbf{E}}$ is the elastic component and $\mathbf{F}_{\mathbf{V}}$ and $\mathbf{F}_{\mathbf{P}}$ are the viscoelastic and viscoplastic components, respectively.

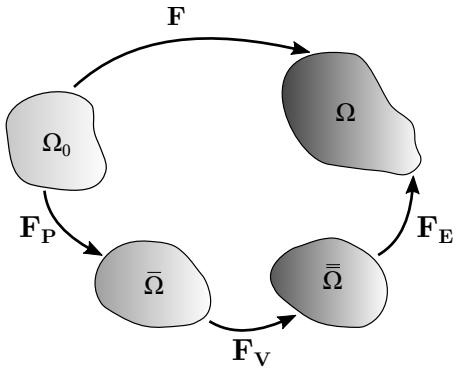

Figure 6.2 Kinematics of the proposed constitutive.

The velocity gradient $\mathbf{l}$ can be written, according to the kinematics of the model, as

$$\mathbf{l} = \mathbf{l_E} + \mathbf{F_E}\bar{\bar{\mathbf{L}}}_{\mathbf{V}}\mathbf{F_E^{-1}} + \mathbf{F_E}\mathbf{F_V}\bar{\mathbf{L}}_{\mathbf{P}}\mathbf{F_V^{-1}}\mathbf{F_E^{-1}} \tag{6.3}$$

where $\mathbf{l_E} = \dot{\mathbf{F}}_{\mathbf{E}}\mathbf{F_E^{-1}}$ is the elastic component of the velocity gradient in Ω, $\bar{\bar{\mathbf{L}}}_{\mathbf{V}} = \dot{\mathbf{F}}_{\mathbf{V}}\mathbf{F_V^{-1}}$ is the viscoelastic component defined in $\bar{\bar{\Omega}}$ and $\bar{\mathbf{L}}_{\mathbf{P}} = \dot{\mathbf{F}}_{\mathbf{P}}\mathbf{F_P^{-1}}$ is the viscoplastic component defined in $\bar{\Omega}$. Both viscoelastic and viscoplastic velocity gradients are equal to the symmetric parts of the corresponding velocity gradients since the configurations $\bar{\Omega}$ and $\bar{\bar{\Omega}}$ are assumed to be invariant to the rigid body rotations of Ω.

6.1.3 Thermodynamics

The constitutive relations of the model have to satisfy the first and second laws of thermodynamics to ensure thermodynamics consistently, which are expressed per unit of reference volume as

$$\dot{e}_0 = \mathbf{P} : \dot{\mathbf{F}} - Div\mathbf{Q} + R \tag{6.4a}$$

$$\dot{\eta_0} \geq -Div\left(\frac{\mathbf{Q}}{\theta_0}\right) + \frac{R}{\theta_0} \tag{6.4b}$$

The constitutive modelling of a hyperelastic material is constructed from the definition of a Helmholtz free-energy function Ψ per unit of reference volume, that can be defined as a function of the internal energy and entropy by

$$\Psi = e_0 - \theta_0\eta_0 \tag{6.5}$$

and expressed in the rate form as

$$\dot{e}_0 = \dot{\Psi} + \dot{\theta}_0\eta_0 + \theta_0\dot{\eta}_0 \tag{6.6}$$

For an isotropic material, Ψ is a scalar function of the deformation gradient $\mathbf{F}$. Moreover, motivated by the kinematics of the model, Ψ is assumed to depend on $\mathbf{F}$, $\mathbf{F_V}$ and $\mathbf{F_P}$, in order to account for viscous effects. Moreover, for transversely isotropic materials, the strain energy function also depends on the preferred direction of the material $\mathbf{a}_0$. From experimental results, it has been observed that the mechanical behaviour of 3D printed polymers is influenced not only by the printing parameters but also by the number of layers, leading to lower stiffness and mechanical performance. In order to include this last dependency, a softening model is proposed. Therefore, the final Helmholtz free-energy function is defined as

$$\Psi = (1-\zeta)\Psi_0(\mathbf{F}, \mathbf{F_V}, \mathbf{F_P}, \mathbf{a}_0) \tag{6.7}$$

where ζ is a softening parameter depending on the number of layers. In addition, the dependencies with the printing parameters such as layer height and raster orientation, are taken into account in the subsequent definition of the energy function.

The rate form of Ψ can be derived using the chain rule as

$$\dot{\Psi} = (1-\zeta)\left[\frac{\partial \Psi_0}{\partial \mathbf{F}} : \dot{\mathbf{F}} + \frac{\partial \Psi_0}{\partial \mathbf{F_V}} : \dot{\mathbf{F}}_\mathbf{V} + \frac{\partial \Psi_0}{\partial \mathbf{F_P}} : \dot{\mathbf{F}}_\mathbf{P}\right] \tag{6.8}$$

Note that ζ depends on the number of layer and remains constant during the deformation process. Combining both laws with Equations (6.6) and (6.8), the Clausius-Duhem inequality is rewritten as

$$\left(\mathbf{P} - (1-\zeta)\frac{\partial \Psi_0}{\partial \mathbf{F}}\right) : \dot{\mathbf{F}} - \left(\frac{\partial \Psi}{\partial \theta_0} + \eta_0\right)\dot{\theta}_0 - (1-\zeta)\frac{\partial \Psi_0}{\partial \mathbf{F_V}} : \dot{\mathbf{F}}_\mathbf{V} - (1-\zeta)\frac{\partial \Psi_0}{\partial \mathbf{F_P}} : \dot{\mathbf{F}}_\mathbf{P} - \frac{\mathbf{Q}Grad\theta_0}{\theta_0} \geq 0 \tag{6.9}$$

This inequality must be satisfied for all thermo-mechanical processes. The terms $\frac{\partial \Psi_0}{\partial \mathbf{F_V}} : \dot{\mathbf{F}}_\mathbf{V}$ and $\frac{\partial \Psi_0}{\partial \mathbf{F_P}} : \dot{\mathbf{F}}_\mathbf{P}$ are related to viscous dissipation and $\mathbf{Q}Grad\theta_0$ corresponds to the thermal conduction (neglected in this work as isothermal conditions are assumed). Therefore, applying Coleman-Noll arguments (Coleman and Noll, 1963; Coleman and Gurtin, 1967), the first Piola-Kirchhoff stress tensor $\mathbf{P}$ and entropy can be derived as

$$\mathbf{P} = (1-\zeta)\frac{\partial \Psi_0}{\partial \mathbf{F}} \tag{6.10a}$$

$$\eta_0 = -\frac{\partial \Psi}{\partial \theta_0} \tag{6.10b}$$

Equation (6.10a) relates the stress with strain energy function and can be also obtained for other alternative stress tensors such as for the second Piola-Kirchhoff $\mathbf{S}$ and Cauchy stress tensors $\boldsymbol{\sigma}$ as

$$\mathbf{S} = (1-\zeta)2\frac{\partial \Psi_0}{\partial \mathbf{C}} \tag{6.11a}$$

$$\boldsymbol{\sigma} = (1-\zeta)\frac{2}{J}\mathbf{F}\frac{\partial \Psi_0}{\partial \mathbf{C}}\mathbf{F}^T \tag{6.11b}$$

6.2 Constitutive equations

6.2.1 Visco-hyperelastic resistance

As stated along this thesis, FDM thermoplastics are orthotropic materials composed by polymeric filaments bonded and voids. In this regard, they can be approached as a matrix reinforced by continuous aligned voids as shown in Figure 2.18. Note that a circular cross-section of the void fibres is considered as a first approach. Thus, the elastic resistance is defined by the strain energy function developed for neo-Hookean composites with aligned continuous cylindrical pores by Guo et al. (2008)

$$\begin{aligned}\Psi_0(\mathbf{C_E}, \mathbf{a}_0) = \Psi_0(I_1^E, I_3^E, I_4^E) = \frac{\mu_m v_m}{2}\left(I_4^E + 2{I_4^E}^{-1/2} - 3\right) \\ + \frac{\mu_m}{2}(J-1){I_4^E}^{-1/2}\ln\left(\frac{J-v_m}{Jv_f}\right) + \frac{\mu_m v_m}{2(1+vf)}\left(I_1^E - I_4^E - 2\sqrt{\frac{I_3^E}{I_4^E}}\right)\end{aligned} \tag{6.12}$$

where v_m and v_f ($v_f = \rho_{voids}$) are the initial volume fractions of matrix and voids ($v_m + v_f = 1$), respectively, and μ_m is the shear modulus of the matrix, $I_1^E = trace(\mathbf{C_E})$, $I_3^E = det(\mathbf{C_E})$ and $I_4^E = \mathbf{a}_0\mathbf{C_E}\mathbf{a}_0$. Note that the energy function from Equation (6.12) is alternatively defined by means of the porous direction $\mathbf{a}_0$ and the elastic right Cauchy-Green deformation tensor $\mathbf{C_E} = \mathbf{F_E}^T\mathbf{F_E}$.

Therefore, the Cauchy stress tensor is obtained as

$$\boldsymbol{\sigma_E} = (1-\zeta)\frac{2}{J^E}\mathbf{F_E}\left[\sum \frac{\partial \Psi_0}{\partial I_i^E}\cdot\frac{\partial I_i^E}{\partial \mathbf{C_E}}\right] : \frac{\partial \mathbf{C_E}}{\partial \mathbf{C}}\mathbf{F_E}^T \tag{6.13}$$

where $\partial\mathbf{C_E}/\partial\mathbf{C}$ is a fourth-order tensor defined as

$$\frac{\partial C_{E_{ij}}}{\partial C_{kl}} = F_{VP_{ki}}F^{-1}_{VP_{lj}} \tag{6.14}$$

Although μ_m is the shear modulus of the material itself, for the components studied in this dissertation, it is proven that the mechanical properties for the components with different layer heights are different, even if considering the real cross-sectional area (without voids). It may arise from differences in the molecular organization of the chains during the printing process due to the amount of material extruded in each condition. This extra difference in shear modulus must be considered on top of the pure effect of porosity and is defined, as a first approach and based on experimental tendencies, by an exponential function as

$$\mu_m = \mu_{m0}(1-v_m)^n \tag{6.15}$$

where μ_{m0} is the shear modulus of the bulk material and n is a material parameter introducing an extra dependency on porosity (Kovácik, 2001).

Finally, the softening variable, which describes the dependency with the number of layers, is given by

$$\zeta = \zeta_\infty[1 - exp(-\alpha/\iota)] \tag{6.16}$$

where ζ_∞ describes the dimensionless maximum softening (i.e the maximum softening of the printed polymer with respect to the bulk material that is observed because of increasing the number of layers), and α is a phenomenological variable that describes the material softening and is defined as $\alpha = (Z - 1)$, with Z being the number of layers. In addition, ι is referred to as the softening saturation parameter, which is the number of layers from which the softening does not increase.

For the definition of the viscoelastic component of the velocity gradient in Ω, the expression used by Garcia-Gonzalez (2019) is taken

$$\mathbf{L_p} = \frac{1}{\sqrt{2}\eta}\boldsymbol{\sigma} \tag{6.17}$$

where η is the viscosity, which is assumed constant for all the cases.

6.2.2 Viscoplastic resistance

In the rheological model, the viscoplastic dashpot is defined in parallel to a friction element. This friction element governs the activation of the plastic flow by a yield function dependent on void fraction. The materials used for FDM are glassy or semi-crystalline polymers and, therefore, the plastic yielding mainly occurs by shear deformation mechanisms (e.g shear transformation zones (Samadi-Dooki et al., 2016; Voyiadjis and Samadi-Dooki, 2016)). In addition, the experimental results show shear bands suggesting the dominance of shear mechanisms during the plastic deformation, see Figures 3.14 and 3.15. The modelling of shear yielding in porous materials has been previously addressed in the literature by Gurson based criteria, even for polymeric materials showing a good predictive capability (Jeridi et al., 2015; Oral et al., 2012). As in this thesis, only the study of thin layers of FDM polymers subjected to tensile conditions is approached, although the hydrostatic stress usually has a relevant influence on the yielding, this dependency is not included in the yielding of the bulk material here. Therefore, the yield function proposed by Gurson (1977) for long circular cylindrical voids and modified by Tvergaard (1981, 1987) is chosen as

$$f = \frac{{\sigma_{eqv}}^2}{{\sigma_0}^2} + 2v_m q_1 \cosh\left(q_2 \frac{\sqrt{3}}{2}\frac{\sigma_{kk}}{\sigma_0}\right) - (1 + (q_1 v_m)^2) = 0 \tag{6.18}$$

where q_1 and q_2 are material parameters that control the dependency with the porosity, σ_{kk} is the transverse hydrostatic stress to filament (or porous) direction, which is equal

to $\sigma_{kk} = \sigma_{22} + \sigma_{33}$ if $\mathbf{a}_0 = [100]$, σ_{eqv} is the equivalent von Mises stress and σ_0 follows an isotropic softening Voce law as

$$\sigma_0 = (1 - \zeta)\left(\sigma_y - (\sigma_s - \sigma_y)\left[1 - \exp(-H\bar{\varepsilon}_p)\right]\right) \tag{6.19}$$

where σ_y is the yield stress, σ_s is the saturation stress, H is the softening parameter and $\bar{\varepsilon}_p$ is the equivalent plastic strain. Since the yield stress is influenced by the number of layers, Eq.(6.19) also includes a softening variable.

The viscoplastic part of the velocity gradient in Ω is defined by an associated viscoplastic flow rule as

$$\mathbf{L_p} = \dot{\gamma_p}\mathbf{N_p} \tag{6.20}$$

where $\dot{\gamma_p}$ is a viscoplastic multiplier providing the magnitude of the plastic flow and $\mathbf{N_p}$ is a tensor that provides its direction. This last tensor is obtained by deriving the yield function with respect to the Cauchy stress as

$$\mathbf{N_p} = \frac{\partial f}{\partial \boldsymbol{\sigma}} \tag{6.21}$$

Finally, the rate of flow is taken to follow a thermally activated process of Arrhenius type (Boyce et al., 2000) that was rewritten by Polanco-Loria et al. (2010) as

$$\dot{\gamma_p} = \begin{cases} 0 & \text{if f}\leq 0 \\ \dot{\varepsilon}_0 \exp\left[\dfrac{1}{C}\left(\dfrac{\sigma_{eqv}}{\sigma_T} - 1\right) - 1\right] & \text{if f}>0 \end{cases} \tag{6.22}$$

where $\dot{\varepsilon}_0$ and C are rate-sensitivity parameters and σ_T derives from Equation (6.18) as

$$\sigma_T = \left(2{\sigma_0}^2 f q_1 \cosh\left(q_2 \frac{\sqrt{3}}{2}\frac{\sigma_{kk}}{\sigma_0}\right) - {\sigma_0}^2(1 + (q_1 f)^2)\right)^{(1/2)} \tag{6.23}$$

6.2.3 Numerical implementation of the model

The model previously described is numerically implemented in MATLAB to reproduce the uniaxial tensile stress-strain response. Apart from the numerical implementation of the constitutive equations, these numerical cases require the additional implementation of a Newton-Raphson integration algorithm to calculate the progressive compressible deformation of the structure during the application of the load. To this end, the following residual is defined as

$$Residual_{long} = \begin{bmatrix} \sigma_{22} \\ \sigma_{33} \end{bmatrix} \approx 0 \tag{6.24a}$$

$$Residual_{trans} = \begin{bmatrix} \sigma_{11} \\ \sigma_{33} \end{bmatrix} \approx 0 \tag{6.24b}$$

where Equation (6.24a) represents the cases when the load is applied longitudinally to the filaments' direction (X direction) and Equation (6.24b) represents the cases when the load is applied transversally to the filaments' direction (Y or Z direction). σ_{11}, σ_{22} and σ_{33} are the Cauchy stress components in the X, Y and Z directions, respectively. The stiffness or iteration matrix can be expressed by means of the stretch components as:

$$K_{long} = \begin{bmatrix} \frac{\partial \sigma_{22}}{\partial \lambda_2} & \frac{\partial \sigma_{22}}{\partial \lambda_3} \\ \frac{\partial \sigma_{33}}{\partial \lambda_2} & \frac{\partial \sigma_{33}}{\partial \lambda_3} \end{bmatrix} \tag{6.25a}$$

$$K_{long} = \begin{bmatrix} \frac{\partial \sigma_{11}}{\partial \lambda_1} & \frac{\partial \sigma_{11}}{\partial \lambda_3} \\ \frac{\partial \sigma_{33}}{\partial \lambda_1} & \frac{\partial \sigma_{33}}{\partial \lambda_3} \end{bmatrix} \tag{6.25b}$$

The final numerical scheme to solve the set of equations is shown in Figure 6.3

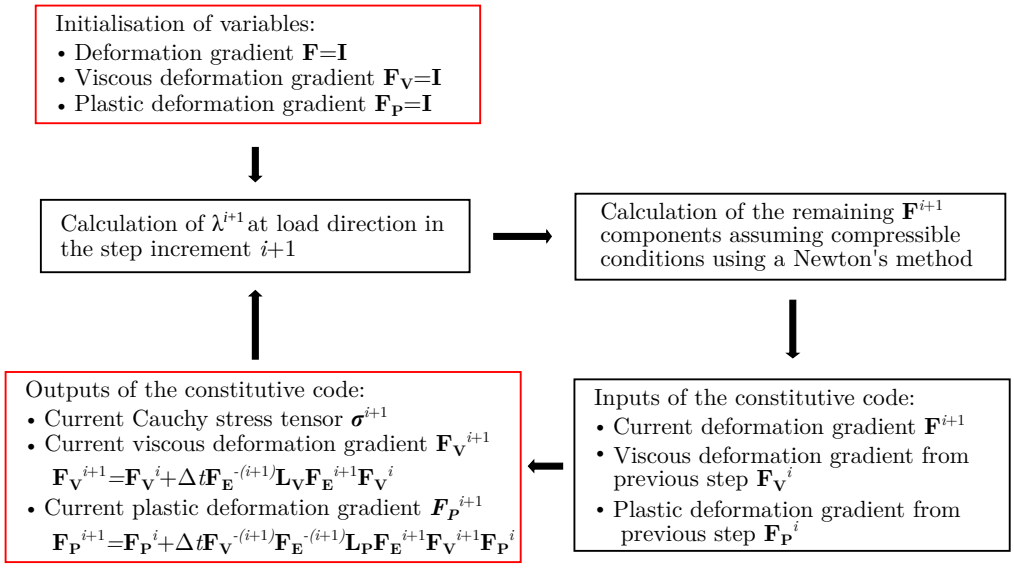

Figure 6.3 Numerical implementation scheme.

6.2.4 Identification of model parameters for FDM ABS

In this section, the identification of the parameters of the previously proposed constitutive model is presented for FDM ABS.

The void density values used for each layer height are shown in Table 6.2. These values are the average of the experimental results obtained in Section 3.2.

Table 6.2 Void densities used in the model.

Layer height (mm)	Void density (%)
0.1	1.1
0.2	2.28
0.3	4.45

Taking as a reference the result obtained for longitudinal one-0.1 mm-layer components at $3 \cdot 10^{-4} s^{-1}$ and considering $\mathbf{a}_0 = \begin{bmatrix} 1 & 0 & 0 \end{bmatrix}$, the model parameters are identified based on their correspondence with the mechanical response following four blocks:

i. Visco-hyperelastic responses

The model parameters μ_{m0} and n determine the hyperelastic response of the material. Moreover, the parameter η governs the linear viscoelastic response and is calibrated against experimental results at different strain rates.

ii. Yield stress

The parameters σ_y, σ_s and H define the yielding process. Moreover, q_1 and q_2 are phenomenological parameters to capture the dependency of the yield stress with void density. Because of plasticity is only reached when the load is applied along the filaments' direction ($\sigma_{kk} = 0$), the value of q_2 is not identified.

iii. Viscoplastic response

$\dot{\varepsilon}_0$ and C are associated with the nonlinear viscoplastic dashpot. The former is set at the lower strain rate used for the experimental tests, while the second one controls the strain rate dependency on yielding.

iv. Softening model

Although the elastic response is modelled as a porous hyperelastic function, the experimental results have shown that the stiffness of specimens manufactured by FDM is not only a function of the void density but also of the number of layers. This is explained by the fact that when the number of layers increases so does the number of interactions. Therefore, an overall softening of the material associated with the 3D printed process has been included to reproduce the dependence of the shear modulus and yield stress with the number of layers. The maximum softening value ζ_∞ is set equal for all the cases. However, the rate with which this value is reached is different for shear modulus ι_μ and yield stress ι_{σ_0}, and for longitudinal (L) and transverse (T) components.

The calibrated parameters for FDM ABS are provided in Table 6.3.

Table 6.3 Material parameters for FDM ABS.

Elastic response		Viscoelastic response	softening model			
μ_{m0} (MPa)	n	η (MPa·s)	ζ_∞	ι_{μ_L}	ι_{μ_T}	ι_{σ_0}
780	4.7	$4.5 \cdot 10^5$	0.7	0.7	7	14
Viscoplastic response						
σ_y (MPa)	σ_s (MPa)	H	q_1	q_2	$\dot{\varepsilon}_0$ (s^{-1})	C
34.5	37.5	110	4.2	-	$3 \cdot 10^{-4}$	0.028

6.3 Results and discussion

This section analyses the suitability of the model to predict the mechanical behaviour of FDM polymers for different printing and loading conditions. To this end, model predictions are compared with the original experiments to analyse the predictive capability on:

i. FDM ABS specimens manufactured with different layer heights (0.1, 0.2 and 0.3 mm).

ii. FDM ABS specimens manufactured with different raster orientation (longitudinal and transverse).

iii. FDM ABS specimens manufactured with different number of layers (from one to three).

iv. FDM ABS specimens tested at different strain rates ($3 \cdot 10^{-4} s^{-1}$ and $3 \cdot 10^{-3} s^{-1}$).

v. FDM ABS specimens tested at load-unload uniaxial tension at a strain rate of $3 \cdot 10^{-4} s^{-1}$.

The ability of the model to predict the elastic nonlinear and yielding behaviour of FDM ABS depending on different void densities is presented in Figure 6.4. This figure compares model predictions and experimental data for one-layer specimens with three different layer heights at $3 \cdot 10^{-4} s^{-1}$. The model is able to capture the anisotropic response and the dependence on porosity. Good agreement between the model predictions and experimental data is found in terms of elastic slope and yielding; however, the model presents a higher error to predict the yield stress for 0.2 mm-layer specimens. This is due to the particular behaviour of these 0.2 mm-layer specimens where their maximum stress is similar to the one obtained for 0.3 mm -layer specimens.

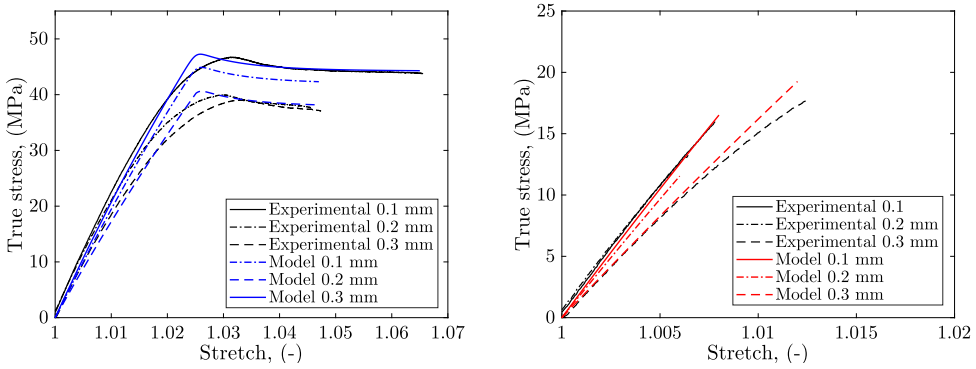

Figure 6.4 Comparison of experimental stress-strain response versus model predictions of one layer FDM ABS specimens with three different layer heights at a strain rate of $3 \cdot 10^{-4} s^{-1}$*: (a) longitudinal and (b) transversal.*

On the other hand, experimental results show that the mechanical response of FDM thermoplastics is influenced by the number of layers due to manufacturing imperfections and interfaces between filaments. This particular dependence is included in the model through a softening variable. Experimental data are compared with model predictions for 0.1 mm-layer specimens with different number of layers of material for both loading directions in Figure 6.5. The predictions demonstrate that the proposed model faithfully captures both shear modulus and yield stress dependencies with the number of layers as well as the influence with the raster orientation. However, more experimental tests are needed to fully analyse this dependence and provide the number of layers that constitutes the upper softening limit.

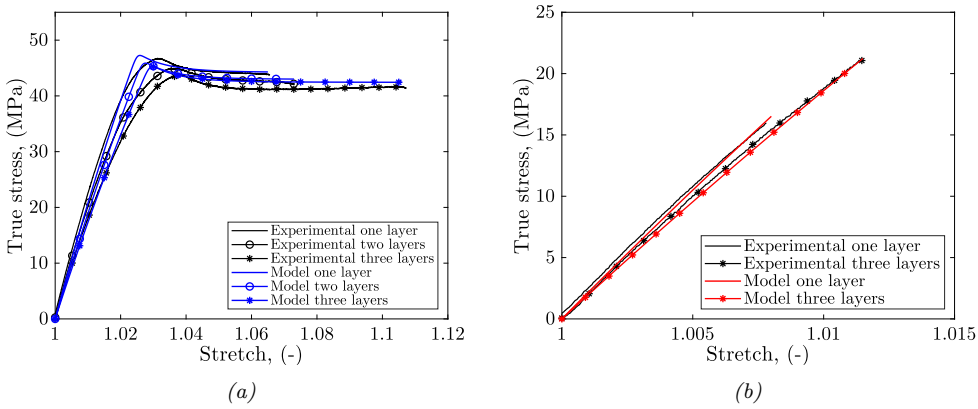

Figure 6.5 Comparison of experimental stress-strain response versus model predictions of 0.1 mm layer height FDM ABS specimens at a strain rate of $3 \cdot 10^{-4} s^{-1}$*: (a) longitudinal specimens with different number of layers and (b) transversal specimens with different number of layers.*

The ability of the model to account for strain rate dependency in both viscoelastic and viscoplastic behaviours is shown in Figure 6.6. The results confirm the ability of the model to predict the hardening increase, in both elastic and inelastic parts, with increasing loading rate.

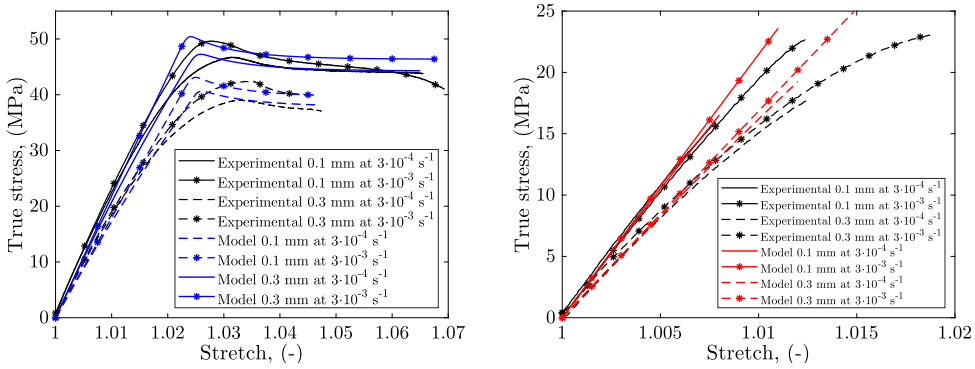

Figure 6.6 Comparison of experimental stress-strain response versus model predictions of one layer FDM ABS specimens at different strain rates: (a) longitudinal 0.1 and 0.3 mm layer height specimens and (b) transversal 0.1 and 0.3 mm layer height specimens.

Moreover, with the aim of illustrating the ability of the model to account for both the number of layers and strain rate, Figure 6.7 shows the model predictions for three-0.3 mm-layer specimens. Although the dependency with the number of layers is calibrated for 0.1 mm components, a good agreement can be also observed between model and experimental results for specimens with different layer heights and for both raster orientations.

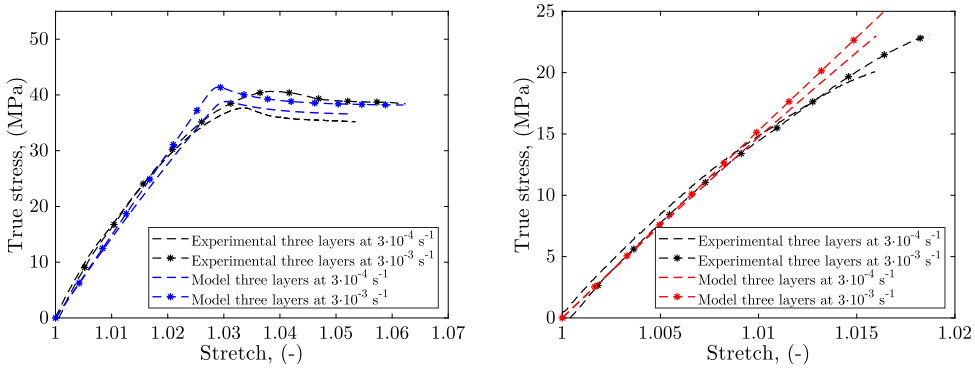

Figure 6.7 Comparison of experimental stress-strain response versus model predictions of three-0.3 mm-layer FDM ABS specimens at different strain rates: (a) longitudinal specimens and (b) transversal specimens.

Finally, Figure 6.8 shows the prediction capability of the model to capture the load-unload tensile response for a one-0.1 mm-layer longitudinal specimen.

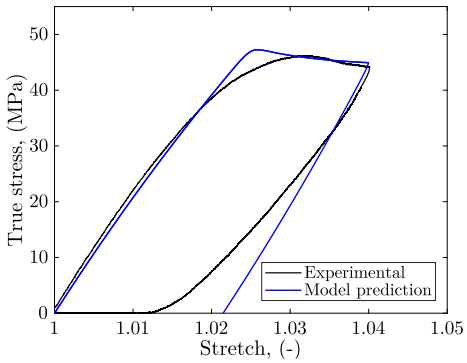

Figure 6.8 Comparison of experimental load-unload tensile response versus model predictions of one-0.1 mm-layer longitudinal FDM ABS specimens at a strain rate of $3 \cdot 10^{-4} s^{-1}$.

In view of the numerical results, it can be concluded that the proposed model constitutes the first continuum approach for finite deformations that accounts for both material and printing dependencies with a proved capability to model the mechanical behaviour of FDM 3D printed thermoplastic polymers. The model is able to capture with good agreement the dependencies with the layer height, number of layers and loading conditions (direction and strain rate). However, further efforts are needed to complete the constitutive description. In this regard, the model is not able to capture the nonlinear behaviour before yielding and fails at predicting adequately the response of 0.2 mm layer specimens.

6.4 Conclusions

FDM components present a complex mechanical behaviour. In this thesis, the influence of three printing parameters has been studied: layer height (which defines the void density), number of layers and raster orientation. In addition, thermoplastic polymers are strain rate dependent and can present different stress-strain curves with nonlinear regions and stages of softening and hardening. Considering these effects, a new constitutive model for FDM components has been developed accounting for strain rate (in both elastic and plastic responses), transverse isotropy, porosity and number of layers dependencies. The consistent thermodynamic framework proposed here is general and permits the development of further constitutive models for FDM polymers.

This general constitutive framework has been particularised for FDM ABS polymers. The model has been numerically implemented and its parameters have been identified for FDM ABS from experimental data previously obtained for uniaxial tensile states.

Good agreement between numerical predictions and experimental data has been found in terms of stress-strain curves depending on load direction, void density, number of layers and strain rate.

The results presented in this chapter demonstrate the capacity of the model proposed to predict the mechanical behaviour of FDM polymers by a continuum approach.

7 Conclusions and future works

This chapter summarises the main conclusions of this doctoral dissertation and proposes future work to follow up the new research line initiated in this thesis.

7.1 Conclusions

In accordance with the main objective, the research carried out along the thesis has allowed to deepen in the understanding of the influence of printing parameters on the mechanical properties of FDM thermoplastics. To this end, the mechanics and thermodynamics of the 3D printing process, which determine the mesostructural and mechanical properties of FDM thermoplastics, have been analysed. Moreover, a new continuum constitutive model for FDM thermoplastics has been developed. To achieve this general goal, other secondary conclusions have been previously reached. While the main results of this thesis have already been exposed at the end of each chapter, in this section, the principal outcomes associated with each specific objective are highlighted.

First, an experimental characterisation of the mesostructure of FDM components has been carried out to study the influence of the printing parameters on it:

i. A mesostructural characterisation has been carried out through the analysis of cross-sectional images of ABS specimens obtained with SEM. The specimens were manufactured with different layer heights, raster orientation and number of layers. From these results, it has been concluded that 3D printed components are porous structures highly influenced by printing parameters such as layer height and number of layers.

ii. From the results and conclusions obtained in this experimental characterisation, an analytical expression to predict the void density has been proposed. This equation has been developed by means of the final mesostructure geometry and validated with experimental results of void density.

Then, an experimental characterisation of the mechanical behaviour of FDM thermoplastics has been carried out to study the influence of printing parameters:

i. A complete experimental campaign has been carried out through the development of uniaxial tensile tests under quasi-static conditions at two different strain rates ($3 \cdot 10^{-4} s^{-1}$, $3 \cdot 10^{-3} s^{-1}$). The specimens were manufactured with different layer heights, raster orientations and number of layers, resulting in a total number of eighteen groups of specimens and more than 140 tests. The results show that the mechanical properties (in terms of elastic modulus and maximum stress) improve when the layer height and number of layers decrease. Moreover, specimens with a longitudinal raster orientation show better performance than those manufactured with a transversal raster orientation.

ii. From the results and conclusions obtained in this experimental characterisation, analytical expressions for the prediction of the mechanical properties (elastic modulus and maximum stress) have been proposed. These equations are a function of the mechanical properties of the bulk material, void density and number of layers.

Next, the mechanics and thermodynamics of the FDM process have been analysed through the development of thermal and sintering models to simulate the bond formation process between adjacent filaments:

i. A new model for the prediction of the evolution of filament temperature has been developed based on the previous work by Costa et al. (2017). Following with the thermal analysis, a 2D heat transfer model has been implemented using the finite difference method to study the intra-fibre heat transfer between adjacent filaments. This last model takes as input the temperatures obtained from the previous one.

ii. A new sintering model has been developed based on the previous work by Pokluda et al. (1997). This model describes the sintering process of two filaments with a cross-sectional geometry in accordance with the geometry observed from original mesostructural characterisation. In addition, the degree of molecular diffusion across the interface of two filaments is studied using the model proposed by Yang and Pitchumani (2002) for the healing process under non-isothermal conditions.

Then, from the analytical expressions and models developed previously, a complete methodology has been proposed for the prediction and optimisation of mesostructural and mechanical properties:

i. The two-stage model, composed by the thermal and sintering models, is combined with the theoretical expressions proposed previously to estimate the final mesostructure and mechanical properties of FDM polymers. This procedure takes as input data manufacturing parameters and material properties of bulk material.

ii. The proposed methodology has been used to conduct end-to-end simulations of the printing process and estimate the mechanical properties and structural details of ABS specimens, reproducing the conditions used in the experimental characterisation. Moreover, a parametric study is developed to study the influence of some manufacturing parameters: layer height, printing speed, environmental temperature and the temperature of the support plate. These results show that layer height is the most critical parameter followed by the environmental temperature.

Finally, a continuum constitutive model for 3D printed thermoplastics has been developed based on the results from previous sections:

i. A new constitutive model for 3D printed thermoplastic polymers has been developed taking into account the experimental insights from the analysis of FDM ABS components. This model accounts for dependencies on strain rate, anisotropy, porosity and number of layers within a thermodynamically consistent framework formulated for finite deformations.

ii. The model parameters have been identified for FDM ABS and the model has been validated for different printing parameters and loading conditions.

iii. The predictive capacity of the model has been evaluated through the study of different cases, showing a good capability to predict dependencies on: porosity (related to layer height), number of layers, strain rate and loading direction.

7.2 Future works

The research carried out in this doctoral dissertation is the beginning of a new research line in the group whose objective is the understanding of the influence of printing parameters on the mechanical response of 3D printed polymers and, ultimately, the development of continuum constitutive models for these new materials. After the completion of this thesis, we present the following works to extend this study:

- The influence of the number of layers on the mechanical behaviour has to be studied for components made with more than three layers of material. In this thesis, the influence of the number of layers on components with one, two and three layers has been approached. However, it is necessary to continue studying their influence in order to find the critical number of layers from which the mechanical softening associated is established.

- The influence of the raster orientation on the mechanical behaviour has to be studied for a wider range of angles. In this thesis, the influence of the raster orientation has been approached for two deposition orientations: 0° or longitudinal and 90° or transversal, where all the layers follow the same direction. Therefore,

the work developed in this dissertation should be extended considering other raster orientations (30°, 45° and 60°) and using an alternating raster pattern, where the print raster direction is alternated by 90° with each subsequent layer.

- The influence of other printing parameters, such as the air gap, has to be approached. In this work, a zero air gap has been used for all the components tested. Following the same experimental methodology proposed in Chapter 3, it is necessary to develop a mesostructural and mechanical characterisation to study the influence of positive and negative air gap, holding the remaining parameters at the recommended or default values.

- Development of the experimental program at different strain rates, temperatures and stress conditions. Thermoplastic polymers present a complex behaviour with strain rate and temperature dependences and pressure sensitivity. In this thesis, uniaxial tensile tests have been carried out at two strain rates at quasi-static conditions. In order to dig into the physical fundamentals behind the mechanical behaviour of 3D printed polymer, it is necessary to develop a more complete experimental program. To this end, uniaxial tensile, compression and impact tests have to be carried out considering a higher range of strain rates and testing temperatures.

- Extension of the new anisotropic viscous-hyperelastic constitutive model for FDM polymers to include the temperature and pressure sensitivities of the material, and the dependency with other printing parameters. Moreover, it would be necessary to include a failure criteria and damage evolution law to describe the mechanical behaviour of 3D printed polymers.

8 Conclusiones y trabajos futuros

Este capítulo recoge las principales conclusiones de esta tesis doctoral y propone trabajos futuros a desarrollar en la línea de investigación iniciada con este trabajo.

8.1 Conclusiones

De acuerdo con los principales objetivos, la investigación llevada a cabo en esta tesis ha permitido profundizar en la influencia de los parámetros de impresión sobre las propiedades mecánicas de polímeros termoplásticos fabricador mediante el modelado por deposición fundida (FDM). Para ello, se ha analizado la mecánica y termodinámica del proceso de impresión, los cuales determinan las propiedades mecánicas y la estructura interna del polímero. Además, se ha desarrollado un nuevo modelo constitutivo del continuo para termoplásticos fabricados por FDM. Para obtener el objetivo general, previamente se han alcanzado otros objetivos parciales. Aunque los resultados principales de esta tesis han sido previamente expuestos al final de cada capítulo, en esta sección, se destacan los principales resultados asociados con cada objetivo específico.

En primer lugar, se analiza la influencia de los parámetros de impresión sobre la mesostructura de los componentes fabricados por FDM, implicando las siguientes actividades:

i. Se ha llevado a cabo una caracterización mesoestructural mediante el análisis de imágenes obtenidas con microscopio electrónico de barrido sobre la sección transversal de muestras fabricadas con ABS. Las muestras se fabricaron variando el espesor de capa, orientación de la deposición y número de capas. A partir de estos resultados, se ha concluido que los componentes impresos por 3D son estructuras porosas altamente influenciadas por parámetros de impresión como el espesor de capa y el número de capas. De esta forma, por ejemplo, es posible disminuir la densidad de vacíos disminuyendo la altura de la capa.

ii. A partir de los resultados y conclusiones obtenidos en esta caracterización experimental, se ha propuesto una expresión analítica para predecir la densidad de vacíos. Esta expresión ha sido desarrollada para predecir de la geometría de la mesoestructura final y se ha validado con resultados experimentales.

A continuación, se analiza la influencia de los parámetros de impresión sobre el comportamiento mecánico de los polímeros termoplásticos fabricados por FDM, implicando las siguientes actividades:

i. Se ha llevado a cabo una campaña experimental mediante el desarrollo de ensayos de tracción uniaxiales en condiciones cuasiestáticas, a dos velocidades de deformación diferentes ($3 \cdot 10^{-4} s^{-1}$, $3 \cdot 10^{-3} s^{-1}$). Las muestras se fabricaron variando el espesor de capa, orientación de de la deposición y número de capas, dando lugar a un total de dieciocho grupos de muestras fabricadas bajo las mismas condiciones y ensayando un total de 140 probetas. Los resultados muestran que las propiedades mecánicas (en términos de módulo elástico y esfuerzo máximo) mejoran cuando la altura de capa y el número de capas disminuyen. Además, las muestras con una orientación de trama longitudinal muestran un mejor comportamiento que las fabricadas con una orientación transversal.

ii. A partir de los resultados y conclusiones obtenidos en esta caracterización mecánica, se han propuesto expresiones analíticas para la predicción de las propiedades mecánicas (módulo elástico y tensión máxima). Estas expresiones dependen de las propiedades mecánicas del material de partida, la densidad de vacíos y el número de capas.

Por otro lado, la mecánica y termodinámica del proceso de FDM se estudia a través del desarrollo de un modelo térmico y de sintering para simular el proceso completo de formación de enlaces entre filamentos, implicando las siguientes actividades:

i. Se ha desarrollado un nuevo modelo para predecir la evolución de la temperatura del filamento basado en el trabajo previo de Costa et al. (2017). Para completar el análisis térmico, se ha implementado un modelo de transferencia de calor 2D utilizando el método de diferencias finitas que permite analizar la transferencia de calor entre filamentos adyacentes. Este modelo toma como entrada las temperaturas obtenidas del modelo térmico previo.

ii. Se ha desarrollado un nuevo modelo de sinterización basado en el trabajo previo de Pokluda et al. (1997). Este modelo describe el proceso de sinterización de dos filamentos adyacentes con una geometría de sección transversal de acuerdo con la observada experimentalmente en este trabajo. Además, se ha estudiado el grado de healing de dos filamentos, definido éste como la difusión molecular a través de la interfaz. Para ello se ha empleado el modelo propuesto por Yang and Pitchumani (2002) desarrollado para procesos de healing en condiciones no isotérmicas.

A partir de las expresiones analíticas y modelos desarrollados previamente, se propone una metodología para predecir y optimizar la mesoestructura y las propiedades mecánicas, implicando las siguientes actividades:

i. El modelo de dos etapas, compuesto por los modelos térmicos y de sinterización, se ha combinado con las expresiones analíticas propuestas para predecir la mesoestructura y las propiedades mecánicas de los polímeros fabricados por FDM. Este procedimiento toma como datos de entrada los parámetros de fabricación y las propiedades del material de partida.

ii. La metodología propuesta se ha utilizado para realizar simulaciones de proceso completo de impresión y predecir las propiedades mecánicas y los detalles estructurales de las muestras de ABS, reproduciendo las condiciones utilizadas en la caracterización experimental. Además, se desarrolla un estudio paramétrico para estudiar la influencia de algunos parámetros de fabricación como espesor de capa, velocidad de impresión, temperatura ambiental y la temperatura de la base de la impresora. Estos resultados muestran que el espesor de capa es el parámetro de impresión más influyente seguido de la temperatura ambiental.

Por último, se desarrolla un modelo constitutivo del continuo para polímeros termoplásticos impresos por 3D basado en las observaciones experimentales obtenidas en de los capítulos anteriores, implicando las siguientes actividades:

i. Se ha desarrollado un nuevo modelo constitutivo para polímeros termoplásticos impresos en 3D teniendo en cuenta las observaciones experimentales del análisis de los componentes fabricados con ABS mediante FDM. Este modelo tiene en cuenta la velocidad de deformación, la anisotropía, la porosidad y la dependencia con el número de capas dentro de un marco termodinámicamente consistente.

ii. Los parámetros del modelo se han identificado para el ABS y el modelo se ha validado para diferentes parámetros de impresión y condiciones de carga.

iii. La capacidad predictiva del modelo se ha evaluado mediante el estudio de diferentes casos, mostrando una buena capacidad para predecir dependencias con: porosidad (relacionada con la altura de capa), número de capas, velocidad de deformación y dirección de carga.

8.2 Trabajos futuros

La investigación realizada en esta tesis doctoral es el comienzo de una nueva línea de investigación en el grupo cuyo objetivo es comprender la influencia de los parámetros de impresión en la respuesta mecánica de los polímeros impresos en 3D y, en última instancia, el desarrollo de modelos constitutivos del continuo. Después de completar esta tesis, presentamos los siguientes trabajos para extender este estudio:

- La influencia del número de capas en el comportamiento mecánico debe estudiarse para los componentes fabricados con más de tres capas de material. En esta tesis, se ha abordado la influencia del número de capas en componentes con una, dos y tres capas. Sin embargo, es necesario profundizar este estudio para encontrar el número crítico de capas a partir del cual se estabiliza el ablandamiento mecánico.

- La influencia de la orientación de deposición en el comportamiento mecánico debe estudiarse para un amplio rango de ángulos. En esta tesis, la influencia de la orientación de deposición se ha abordado para dos orientaciones diferentes: 0 ° o longitudinal y 90 ° o transversal, donde todas las capas siguen la misma dirección. Por lo tanto, el trabajo desarrollado en esta tesis debe extenderse considerando otras orientaciones de impresión (30 °, 45 ° y 60 °) y utilizando una orientación alterna, donde la dirección de impresión de las capas es alternada en 90 °.

- Se debe abordar el estudio de la influencia de otros parámetros de impresión, como el espacio entre filamentos adyacentes (air gap). En este trabajo, se ha utilizado un espacio entre filamentos adyacentes cero para todos los componentes ensayados. Siguiendo la misma metodología experimental propuesta en el Capítulo 3, es necesario desarrollar una caracterización de la mesoestructura y del comportamiento mecánico para estudiar la influencia del espacio entre filamentos adyacentes positivo y negativo, manteniendo los parámetros restantes en los valores recomendados o predeterminados.

- Desarrollo de un programa experimental a diferentes velocidades de deformación, temperaturas y condiciones de carga. Los polímeros termoplásticos presentan un comportamiento complejo con dependencia con la velocidad de deformación y temperatura y sensibilidad a la presión. En esta tesis, se han realizado pruebas de tracción uniaxiales a dos velocidades de deformación en condiciones cuasiestáticas. Para profundizar en los fundamentos físicos detrás del comportamiento mecánico del polímero impreso en 3D, es necesario desarrollar un programa experimental más completo. Para este fin, se deben realizar pruebas uniaxiales de tracción, compresión de carga cíclica considerando un alto rango de velocidades de deformación y temperaturas.

- Ampliación del nuevo modelo constitutivo para polímeros termoplástico impreso en 3D que incluya las dependencias con la temperatura y presión del material, y la dependencia con otros parámetros de impresión. Además, sería necesario incluir un criterio de fallo y una ley de evolución del daño para describir su comportamiento mecánico completo.

Acknowledgements of Financial Support of Public Institution

The author thank support from Comunidad de Madrid (Talent Attraction grant CM 2018 - 2018-T2/IND-9992), Ministerio de Ciencia, Innovación y Universidades (RTI2018-094318-B-I00) and Vicerrectorado de Política Científica UC3M (Project 2013-00219-002).

Bibliography

Ahn, S., Montero, M., Odell, D., Roundy, S., and Wright, P. K. (2002). Anisotropic material properties of fused deposition modeling abs. *Rapid Prototyping Journal*, 8(4):248–257, DOI: 10.1108/13552540210441166.

Ahn, S.-H., Baek, C., Lee, S., and Ahn, I. (2003). Anisotropic tensile failure model of rapid prototyping parts - fused deposition modeling (fdm). *International Journal of Modern Physics B*, 17:1510–1516.

Alaimo, G., Marconi, S., Costato, L., and Auricchio, F. (2017). Influence of meso-structure and chemical composition on fdm 3d-printed parts. *Composites Part B: Engineering*, 113:371 – 380, DOI: https://doi.org/10.1016/j.compositesb.2017.01.019.

Aliheidari, N., Tripuraneni, R., Ameli, A., and Nadimpalli, S. (2017). Fracture resistance measurement of fused deposition modeling 3d printed polymers. *Polymer Testing*, 60:94 – 101, DOI: https://doi.org/10.1016/j.polymertesting.2017.03.016.

Arruda, E. M. and Boyce, M. C. (1993a). Evolution of plastic anisotropy in amorphous polymers during finite straining. *International Journal of Plasticity*, 9(6):697 – 720, DOI: https://doi.org/10.1016/0749-6419(93)90034-N.

Arruda, E. M. and Boyce, M. C. (1993b). A three-dimensional constitutive model for the large stretch behavior of rubber elastic materials. *Journal of the Mechanics and Physics of Solids*, 41(2):389 – 412, DOI: https://doi.org/10.1016/0022-5096(93)90013-6.

ASTM D638-14 (2014). Standard Terminology for Additive Manufacturing Technologies. Standard, ASTM International, West Conshohocken, PA.

ASTM F2792-12a (2012). Standard Terminology for Additive Manufacturing Technologies. Standard, ASTM International, West Conshohocken, PA.

Bahr, F. and Westkamper, E. (2018). Correlations between influencing parameters and quality properties of components produced by fused deposition modeling. *Procedia CIRP*, 72:1214 – 1219, DOI: https://doi.org/10.1016/j.procir.2018.03.048. 51st CIRP Conference on Manufacturing Systems.

Bandyopadhyay, A. and Bose, S. (2015). *Additive manufacturing*. CRC press.

Bellehumeur, C., Li, L., Sun, Q., and Gu, P. (2004). Modeling of bond formation between polymer filaments in the fused deposition modeling process. *Journal of Manufacturing Processes*, 6(2):170 – 178, DOI: https://doi.org/10.1016/S1526-6125(04)70071-7.

Bellehumeur, C. T., Bisaria, M. K., and Vlachopoulos, J. (1996). An experimental study and model assessment of polymer sintering. *Polymer Engineering & Science*, 36(17):2198–2207, DOI: 10.1002/pen.10617.

Bergström, J. (2015a). 1 - introduction and overview. In Bergström, J., editor, *Mechanics of Solid Polymers*, pages 1 – 17. William Andrew Publishing.

Bergström, J. (2015b). 4 - continuum mechanics foundations. In Bergström, J., editor, *Mechanics of Solid Polymers*, pages 131 – 207. William Andrew Publishing.

Bergström, J. (2015c). 5 - elasticity/hyperelasticity. In Bergström, J., editor, *Mechanics of Solid Polymers*, pages 209 – 307. William Andrew Publishing.

Blatz, P. J. and Ko, W. L. (1962). Application of finite elastic theory to the deformation of rubbery materials. *Transactions of the Society of Rheology*, 6(1):223–252, DOI: 10.1122/1.548937.

Bower, D. I. (2002). *An Introduction to Polymer Physics*. Cambridge University Press.

Boyce, M., Socrate, S., and Llana, P. (2000). Constitutive model for the finite deformation stress–strain behavior of poly(ethylene terephthalate) above the glass transition. *Polymer*, 41(6):2183 – 2201, DOI: https://doi.org/10.1016/S0032-3861(99)00406-1.

BQ (2019). https://www.bq.com.

Butler, C. A., Mccullough, R. L., Pitchumani, R., and John W. Gillespie, J. (1998). An analysis of mechanisms governing fusion bonding of thermoplastic composites. *Journal of Thermoplastic Composite Materials*, 11(4):338–363, DOI: 10.1177/089270579801100404.

Cantrell, J., Rohde, S., Damiani, D., Gurnani, R., DiSandro, L., Anton, J., Young, A., Jerez, A., Steinbach, D., Kroese, C., and Ifju, P. (2017). Experimental characterization of the mechanical properties of 3d printed abs and polycarbonate parts. In Yoshida, S., Lamberti, L., and Sciammarella, C., editors, *Advancement of Optical Methods in Experimental Mechanics, Volume 3*, pages 89–105, Cham. Springer International Publishing.

Chacón, J., Caminero, M., García-Plaza, E., and Núñez, P. (2017). Additive manufacturing of pla structures using fused deposition modelling: Effect of process parameters on mechanical properties and their optimal selection. *Materials& Design*, 124:143 – 157, DOI: https://doi.org/10.1016/j.matdes.2017.03.065.

Choren, J. A., Heinrich, S. M., and Silver-Thorn, M. B. (2013). Young's modulus and volume porosity relationships for additive manufacturing applications. *Journal of Materials Science*, 48(15):5103–5112, DOI: 10.1007/s10853-013-7237-5.

Coleman, B. D. and Noll, W. (1963). The thermodynamics of elastic materials with heat conduction and viscosity. *Archive for Rational Mechanics and Analysis*, 13(1):167–178, DOI: 10.1007/BF01262690.

Coleman, B. D. D. and Gurtin, M. E. (1967). Thermodynamics with internal state variables. DOI: 10.1184/R1/6480089.v1.

Coogan, T. J. and Kazmer, D. (2017). Healing simulation for bond strength prediction of fdm. *Rapid Prototyping Journal*, 23, DOI: 10.1108/RPJ-03-2016-0051.

Costa, S., Duarte, F., and Covas, J. (2015). Thermal conditions affecting heat transfer in fdm/ffe: a contribution towards the numerical modelling of the process. *Virtual and Physical Prototyping*, 10(1):35–46, DOI: 10.1080/17452759.2014.984042.

Costa, S., Duarte, F., and Covas, J. (2017). Estimation of filament temperature and adhesion development in fused deposition techniques. *Journal of Materials Processing Technology*, 245:167 – 179, DOI: https://doi.org/10.1016/j.jmatprotec.2017.02.026.

Croccolo, D., Agostinis, M. D., and Olmi, G. (2013). Experimental characterization and analytical modelling of the mechanical behaviour of fused deposition processed parts made of abs-m30. *Computational Materials Science*, 79:506 – 518, DOI: https://doi.org/10.1016/j.commatsci.2013.06.041.

de Gennes, P. G. (1971). Reptation of a Polymer Chain in the Presence of Fixed Obstacles. *The Journal of Chemical Physics*, 55:572–579, DOI: 10.1063/1.1675789.

Domingo-Espin, M., Puigoriol-Forcada, J. M., Garcia-Granada, A.-A., Llumà, J., Borros, S., and Reyes, G. (2015). Mechanical property characterization and simulation of fused deposition modeling polycarbonate parts. *Materials & Design*, 83:670 – 677, DOI: https://doi.org/10.1016/j.matdes.2015.06.074.

Eshelby, J. (1949). Discussion of 'seminar on the kinetics of sintering'. *Metall. Trans*, 185:796–813.

Fehlberg, E. (1970). Klassische runge-kutta-formeln vierter und niedrigerer ordnung mit schrittweiten-kontrolle und ihre anwendung auf wärmeleitungsprobleme. *Computing*, 6(1):61–71, DOI: 10.1007/BF02241732.

Frenkel, J. (1945). Viscous flow of crystalline bodies under the action of surface tension. *J. Phys.*, 9:501–559.

Garcia-Gonzalez, D. (2016). *A continuum mechanics framework for hyperelastic materials: connecting experiments and modelling*. Tesis Doctoral, UC3M.

Garcia-Gonzalez, D. (2019). Magneto-visco-hyperelasticity for hard-magnetic soft materials: theory and numerical applications. *Smart Materials and Structures*, 28(8):085020, DOI: 10.1088/1361-665x/ab2b05.

Garcia-Gonzalez, D., Garzon-Hernandez, S., and Arias, A. (2018a). A new constitutive model for polymeric matrices: Application to biomedical materials. *Composites Part B: Engineering*, 139:117 – 129, DOI: https://doi.org/10.1016/j.compositesb.2017.11.045.

Garcia-Gonzalez, D., Jérusalem, A., Garzon-Hernandez, S., Zaera, R., and Arias, A. (2018b). A continuum mechanics constitutive framework for transverse isotropic soft tissues. *Journal of the Mechanics and Physics of Solids*, 112:209 – 224, DOI: https://doi.org/10.1016/j.jmps.2017.12.001.

Garcia-Gonzalez, D., Zaera, R., and Arias, A. (2017). A hyperelastic-thermoviscoplastic constitutive model for semi-crystalline polymers: Application to peek under dynamic loading conditions. *International Journal of Plasticity*, 88:27 – 52, DOI: https://doi.org/10.1016/j.ijplas.2016.09.011.

Gasser, T., W Ogden, R., and Holzapfel, G. (2006). Hyperelastic modeling of arterial layers with distributed collagen fibre orientations. *Journal of the Royal Society, Interface / the Royal Society*, 3:15–35, DOI: 10.1098/rsif.2005.0073.

Greenhalgh, E. S. (2009). 4 - delamination-dominated failures in polymer composites. In Greenhalgh, E. S., editor, *Failure Analysis and Fractography of Polymer Composites*, Woodhead Publishing Series in Composites Science and Engineering, pages 164 – 237. Woodhead Publishing.

Guo, Z., Caner, F., Peng, X., and Moran, B. (2008). On constitutive modelling of porous neo-hookean composites. *Journal of the Mechanics and Physics of Solids*, 56(6):2338 – 2357, DOI: https://doi.org/10.1016/j.jmps.2007.12.007.

Gurson, A. (1977). Continuum theory of ductile rupture by void nucleation and growth: Part i—yield criteria and flow rules for porous ductile media. *Transaction of ASME*, 99, DOI: 10.1115/1.3443401.

Holzapfel, G. (2000). *Nonlinear solid mechanics: a continuum approach for engineering*.

Holzapfel, G. A., Gasser, T. C., and Ogden, R. W. (2000). A new constitutive framework for arterial wall mechanics and a comparative study of material models. *Journal of elasticity and the physical science of solids*, 61(1):1–48, DOI: 10.1023/A:1010835316564.

Hopper, R. W. (1984). Coalescence of two equal cylinders: Exact results for creeping viscous plane flow driven by capillarity. *Journal of the American Ceramic Society*, 67(12):C-262–C-264, DOI: 10.1111/j.1151-2916.1984.tb19692.x.

Hull, C. W. (1986). Apparatus for production of three-dimensional objects by stereolithography.

ImageJ (2019). https://imagej.nih.gov/ij/.

ISO 527-1 (2012). Plastics-Determination of tensile properties. Standard, International Organization for Standardizationl, Geneva, CH.

Jeridi, M., Laiarinandrasana, L., and Saï, K. (2015). Comparative study of continuum damage mechanics and mechanics of porous media based on multi-mechanism model on polyamide 6 semi-crystalline polymer. *International Journal of Solids and Structures*, 53:12 – 27, DOI: https://doi.org/10.1016/j.ijsolstr.2014.10.031.

Kovácik, J. (2001). Correlation between shear modulus and porosity in porous materials. *Journal of Materials Science Letters*, 20(21):1953–1955, DOI: 10.1023/A:1013186702962.

Kreyszig, E. (2010). *Advanced Engineering Mathematics*, chapter 21, pages 906–908. John Wiley & Sons.

Laiarinandrasana, L., Lafarge, M., and Hochstetter, G. (2009). Accounting for porosity, time and temperature dependency in fracture mechanics concepts on polyvinylidene fluoride material. *Engineering Fracture Mechanics*, 76(18):2766 – 2779, DOI: https://doi.org/10.1016/j.engfracmech.2009.06.003. Fracture of Polymers, Composites and Adhesives.

Letcher, T., Rankouhi, B., and Javadpour, S. (2015). Experimental study of mechanical properties of additively manufactured abs plastic as a function of layer parameters.

Li, L., Sun, Q., Bellehumeur, C., and Gu, P. (2002). Composite modeling and analysis for fabrication of fdm prototypes with locally controlled properties. *Journal of Manufacturing Processes*, 4(2):129 – 141, DOI: https://doi.org/10.1016/S1526-6125(02)70139-4.

Lim, L.-T., Auras, R., and Rubino, M. (2008). Processing technologies for poly(lactic acid). *Progress in Polymer Science*, 33(8):820 – 852, DOI: https://doi.org/10.1016/j.progpolymsci.2008.05.004.

Liu, X., Zhang, M., Li, S., Si, L., Peng, J., and Hu, Y. (2017). Mechanical property parametric appraisal of fused deposition modeling parts based on the gray taguchi method. *The International Journal of Advanced Manufacturing Technology*, 89(5):2387–2397.

Lopez-Pamies, O. and Castañeda, P. P. (2007). Homogenization-based constitutive models for porous elastomers and implications for macroscopic instabilities: I—analysis. *Journal of the Mechanics and Physics of Solids*, 55(8):1677 – 1701, DOI: https://doi.org/10.1016/j.jmps.2007.01.007.

MyScope (2019). https://myscope.training/.

Ngo, T. D., Kashani, A., Imbalzano, G., Nguyen, K. T., and Hui, D. (2018). Additive manufacturing (3d printing): A review of materials, methods, applications and challenges. *Composites Part B: Engineering*, 143:172 – 196, DOI: https://doi.org/10.1016/j.compositesb.2018.02.012.

Oral, A., Anlas, G., and Lambros, J. (2012). Determination of gurson–tvergaard–needleman model parameters for failure of a polymeric material. *International Journal of Damage Mechanics - INT J DAMAGE MECH*, 21:3–25, DOI: 10.1177/1056789510385261.

Palais, R. S. and Palais, R. A. (2009). *Differential equations, mechanics, and computation*, volume 51. American Mathematical Soc.

Pawlak, A., Galeski, A., and Rozanski, A. (2014). Cavitation during deformation of semicrystalline polymers. *Progress in Polymer Science*, 39(5):921 – 958, DOI: https://doi.org/10.1016/j.progpolymsci.2013.10.007.

Petrie, C. J. (1999). Extensional flows. In Siginer, D., Kee, D. D., and Chhabra, R., editors, *Advances in the Flow and Rheology of Non-Newtonian Fluids*, volume 8 of *Rheology Series*, pages 613 – 636. Elsevier.

Pissanetzky, S. (1984). *Sparse Matrix Technology*. Academic Press.

Pokluda, O., Bellehumeur, C. T., and Vlachopoulos, J. (1997). Modification of frenkel's model for sintering. *AIChE Journal*, 43(12):3253–3256, DOI: 10.1002/aic.690431213.

Polanco-Loria, M., Clausen, A. H., Berstad, T., and Hopperstad, O. S. (2010). Constitutive model for thermoplastics with structural applications. *International Journal of Impact Engineering*, 37(12):1207 – 1219, DOI: https://doi.org/10.1016/j.ijimpeng.2010.06.006.

Rankouhi, B., Javadpour, S., Delfanian, F., and Letcher, T. (2016). Failure analysis and mechanical characterization of 3d printed abs with respect to layer thickness and orientation. *Journal of Failure Analysis and Prevention*, 16(3):467–481, DOI: 10.1007/s11668-016-0113-2.

Rodríguez, J. F., Thomas, J. P., and Renaud, J. E. (2001). Mechanical behavior of acrylonitrile butadiene styrene (abs) fused deposition materials. experimental investigation. *Rapid Prototyping Journal*, 7(3):148–158, DOI: 10.1108/13552540110395547.

Rodriguez, J. F., Thomas, J. P., and Renaud., J. E. (1999). Maximizing the strength of fused-deposition abs plastic parts. In *Solid freeform fabrication symposium*, pages 335–342. University of Texas at Austin, Austin, TX.

Rodriguez, J. F., Thomas, J. P., and Renaud, J. E. (2000). Characterization of the mesostructure of fused-deposition acrylonitrile-butadiene-styrene materials. *Rapid Prototyping Journal*, 6(3):175–186, DOI: 10.1108/13552540010337056.

Rosenzweig, N. and Narkis, M. (1981). Sintering rheology of amorphous polymers. *Polymer Engineering & Science*, 21:1167 – 1170, DOI: 10.1002/pen.760211709.

Samadi-Dooki, A., Malekmotiei, L., and Voyiadjis, G. Z. (2016). Characterizing shear transformation zones in polycarbonate using nanoindentation. *Polymer*, 82:238 – 245, DOI: https://doi.org/10.1016/j.polymer.2015.11.049.

Smart materials 3D (2019). https://www.smartmaterials3d.com.

Somireddy, M., Czekanski, A., and Singh, C. V. (2018). Development of constitutive material model of 3d printed structure via fdm. *Materials Today Communications*, 15:143 – 152, DOI: https://doi.org/10.1016/j.mtcomm.2018.03.004.

Song, Y., Li, Y., Song, W., Yee, K., Lee, K.-Y., and Tagarielli, V. (2017). Measurements of the mechanical response of unidirectional 3d-printed pla. *Materials & Design*, 123:154 – 164, DOI: https://doi.org/10.1016/j.matdes.2017.03.051.

Sood, A. K., Ohdar, R., and Mahapatra, S. (2010). Parametric appraisal of mechanical property of fused deposition modelling processed parts. *Materials & Design*, 31(1):287 – 295, DOI: https://doi.org/10.1016/j.matdes.2009.06.016.

Sood, A. K., Ohdar, R. K., and Mahapatra, S. S. (2012). Experimental investigation and empirical modelling of fdm process for compressive strength improvement. *Journal of Advanced Research*, 3(1):81 – 90, DOI: https://doi.org/10.1016/j.jare.2011.05.001.

Spencer, A. (1972). *Deformations of fibre-reinforced materials*. Oxford science research papers. Clarendon Press.

Srivatsan, T. and Sudarshan, T. (2015). *Additive manufacturing: innovations, advances, and applications*. CRC Press.

Sun, Q., Rizvi, G., Bellehumeur, C., and Gu, P. (2008). Effect of processing conditions on the bonding quality of fdm polymer filaments. *Rapid Prototyping Journal*, 14(2):72–80, DOI: 10.1108/13552540810862028.

Thomas, J. and Rodriguez, J. (2000). Modeling the fracture strength between fused-deposition extruded roads. *Proc. Solid Freeform Fabr. Symp*, pages 16–23.

Torrado, A. R. and Roberson, D. A. (2016). Failure analysis and anisotropy evaluation of 3d-printed tensile test specimens of different geometries and print raster patterns. *Journal of Failure Analysis and Prevention*, 16(1):154–164, DOI: 10.1007/s11668-016-0067-4.

Truss, R. W. and Chadwick, G. A. (1976). Tensile deformation behaviour of abs polymers. *Journal of Materials Science*, 11(1):111–117, DOI: 10.1007/BF00541081.

Tvergaard, V. (1981). Influence of voids on shear band instabilities under plane strain conditions. *International Journal of Fracture*, 17(4):389–407, DOI: 10.1007/BF00036191.

Tvergaard, V. (1987). Effect of yield surface curvature and void nucleation on plastic flow localization. *Journal of the Mechanics and Physics of Solids*, 35(1):43 – 60, DOI: https://doi.org/10.1016/0022-5096(87)90027-5.

Tvergaard, V. and Needleman, A. (1984). Analysis of the cup-cone fracture in a round tensile bar. *Acta Metallurgica*, 32(1):157 – 169, DOI: https://doi.org/10.1016/0001-6160(84)90213-X.

Ultimaker Cura (2019). https://ultimaker.com/software/ultimaker-cura.

Vairis, A., Petousis, M., Vidakis, N., and Savvakis, K. (2016). On the strain rate sensitivity of abs and abs plus fused deposition modeling parts. *Journal of Materials Engineering and Performance*, 25(9):3558–3565, DOI: 10.1007/s11665-016-2198-x.

Voyiadjis, G. and Samadi-Dooki, A. (2016). Constitutive modeling of large inelastic deformation of amorphous polymers: Free volume and shear transformation zone dynamics. *Journal of Applied Physics*, 119:225104, DOI: 10.1063/1.4953355.

Wang, P., Zou, B., Xiao, H., Ding, S., and Huang, C. (2019). Effects of printing parameters of fused deposition modeling on mechanical properties, surface quality, and microstructure of peek. *Journal of Materials Processing Technology*, 271:62 – 74, DOI: https://doi.org/10.1016/j.jmatprotec.2019.03.016.

Wang, X., Jiang, M., Zhou, Z., Gou, J., and Hui, D. (2017). 3d printing of polymer matrix composites: A review and prospective. *Composites Part B: Engineering*, 110:442 – 458, DOI: https://doi.org/10.1016/j.compositesb.2016.11.034.

Wool, R. P. and O'Connor, K. (1981). A theory crack healing in polymers.

Wool, R. P., Yuan, B.-L., and McGarel, O. J. (1989). Welding of polymer interfaces. *Polymer Engineering & Science*, 29(19):1340–1367, DOI: 10.1002/pen.760291906.

Yang, F. and Pitchumani, R. (2002). Healing of thermoplastic polymers at an interface under nonisothermal conditions. *Macromolecules*, 35(8):3213–3224, DOI: 10.1021/ma010858o.

Ziemian, C., Sharma, M., and Ziemian, S. (2012). Anisotropic mechanical properties of abs parts fabricated by fused deposition modelling. In Gokcek, M., editor, *Mechanical Engineering*, chapter 7. IntechOpen, Rijeka.

Zou, R., Xia, Y., Liu, S., Hu, P., Hou, W., Hu, Q., and Shan, C. (2016). Isotropic and anisotropic elasticity and yielding of 3d printed material. *Composites Part B: Engineering*, 99:506 – 513, DOI: https://doi.org/10.1016/j.compositesb.2016.06.009.

A Introdution to Continuum Mechanics

This Appendix introduces the basic fundamentals of hyperelastic constitutive modelling necessaries for the development of this dissertation. This appendix has been developed on the works of Bergström (2015b); Holzapfel (2000) and Garcia-Gonzalez (2016).

A.1 Finite deformation kinematics

The kinematics of the deformation expresses mathematically the movement of different part of a body of interest during a deformation event. A deformable continuum body $\mathcal{B}$ can be considered as a collection of infinitesimal volume elements referred as material points. During a loading event, when the deformations are finite, the shape and localization of $\mathcal{B}$ changes from the reference configuration Ω_0 at time $t = 0$ to the current configuration Ω at different times $t > 0$, as described in Figure A.1.

Taking a material point that initially occupies a position given by $\mathbf{X}$, called the reference (or material) location, is it possible to reach the new position given by $\mathbf{x}$, called current or spatial location of the material point by the mapping

$$\mathbf{x} = \chi(\mathbf{X}, t) \tag{A.1}$$

A.1.1 Deformation gradient

As stated before, under the applied displacement and load, a body $\mathcal{B}$ undergoes a variation of shape, size and localization from Ω_0 to Ω. Considering an infinitesimal line element $\mathrm{d}\mathbf{X}$ under deformation process, see Figure A.1 it is transformed into $\mathrm{d}\mathbf{x}$ by

$$\mathrm{d}\mathbf{x} = \mathbf{F}(\mathbf{X}, t)\mathrm{d}\mathbf{X} \tag{A.2}$$

where **F** referred to the deformation gradient that is defined as

$$\mathbf{F} = \frac{\partial \chi(\mathbf{X}, t)}{\partial \mathbf{X}} \tag{A.3}$$

Therefore, the deformation gradient is the primary measure of deformation and establishes a linear transformation that gives a vector d**x** by the action of **F** on the vector d**X**.

In the same way, the deformation gradient specifies how the volume is changed during a transformation. Considering a small volume element dV in the reference configuration under deformation process, it is transformed into dv in the current configuration by

$$\mathrm{d}v = \det \mathbf{F}(\mathbf{X}, t)\mathrm{d}V > 0 \tag{A.4}$$

where the determinant of **F** is referred to the Jacobian J which gives the volume ratio of the current volume to the reference volume.

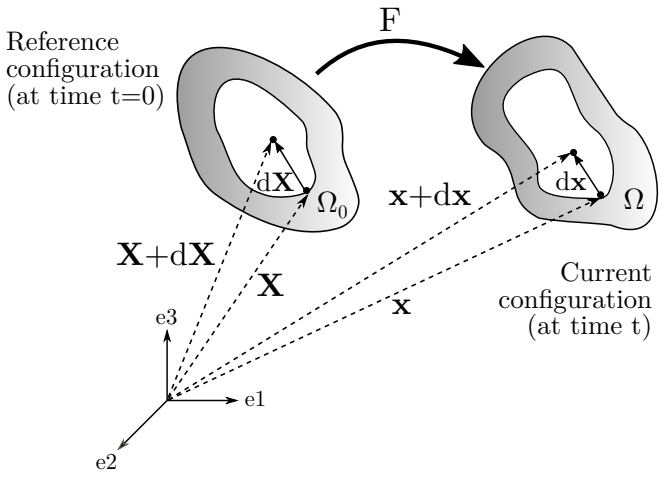

Figure A.1 Deformation of a continuum body, adapted from Holzapfel (2000).

A.1.2 Strain tensors

The deformation gradient previously described, is the fundamental second-order tensor that describes the evolution of material elements during motion in finite deformation kinematics. This gradient can be uniquely decomposed into a pure stretch component and a pure rotation as

$$\mathbf{F}{=}\mathbf{R}\mathbf{U}{=}\mathbf{V}\mathbf{R} \tag{A.5}$$

where **R** is the orthogonal rotation tensor, which is volume conserving, and **U** and **V** are right and left stretch tensors respectively, which are positive and symmetric tensors.

Unlike displacements which are measurable quantities, strain is a non-measurable concept. Since deformation gradient describes the changes of material elements during

motion, it can be used for the description of strain. However, by definition, the strain should be independent of rigid body rotation. So that, the strain tensor cannot be directly dependent on the rotation tensor $\mathbf{R}$. Therefore, the strain tensor depends on the right or left stretch tensors. Some of the most used strain tensor is the right and left Cauchy-Green tensors, defined as

$$\begin{aligned} \mathbf{C} &= \mathbf{F}^T\mathbf{F} = \mathbf{U}^2 \\ \mathbf{B} &= \mathbf{F}\mathbf{F}^T = \mathbf{V}^2 \end{aligned} \tag{A.6}$$

In addition, other common strain tensor is the Green-Lagrange strain tensor which is written as

$$\mathbf{E} = \frac{1}{2}(\mathbf{C} - \mathbf{I}) \tag{A.7}$$

where $\mathbf{I}$ is the identity second-order tensor.

A.1.3 Rates of deformation tensors

To incorporate viscoelasticity and viscoplasticity effects is necessary to consider the time derivation of the deformation gradient defined as

$$\dot{\mathbf{F}}(\mathbf{X}, t) = \frac{\partial}{\partial t}\left(\frac{\partial \mathbf{x}}{\partial \mathbf{X}}\right) = \frac{\partial \mathbf{v}(\mathbf{X}, t)}{\partial \mathbf{X}} \tag{A.8}$$

In addition, it can be also written as $\dot{\mathbf{F}} = \mathbf{l}\mathbf{F}$, where $\mathbf{l} = grad\mathbf{v}(\mathbf{X}, t)$ is the spatial velocity gradient. At the same time, the spatial gradient can be decomposed into rate of deformation tensor $\mathbf{d}$ or symmetric part, which captures rates of deformation, and the spin tensor $\mathbf{w}$ or anti-symmetric part, which captures rates of rotation, as $\mathbf{l} = \mathbf{d} + \mathbf{w}$ where

$$\begin{aligned} \mathbf{d} &= \frac{1}{2}(\mathbf{l} + \mathbf{l}^T) = \mathbf{d}^T \\ \mathbf{w} &= \frac{1}{2}(\mathbf{l} - \mathbf{l}^T) = -\mathbf{w}^T \end{aligned} \tag{A.9}$$

A.2 Stress tensor

As a result of the motion and deformation of a continuum body, there is an interaction between the material points in the interior of the body. As a consequence, stress within the body is responsible for the deformation of the material. In order to define the concept of stress, let us consider a general body $\mathcal{B}$ exposed at external forces on the boundary surface $\partial\Omega$ at time $t > 0$, see Figure A.2. This body has been virtually cut along plane π in two parts. Taking the material point $\mathbf{x}$ of the cutting surface, $\mathbf{n}$ is a unitary outward normal vector and ds an infinitesimal area at point $\mathbf{x}$. In order to satisfy force equilibrium for the interaction of both parts of the body, internal surface forces transmitted through the cut plane generate a traction vector $\mathbf{t}$, known as Cauchy traction vector. Taking

the previous concepts, Cauchy's stress theorem states that exists a unique second-order tensor field $\boldsymbol{\sigma}$ independent of $\mathbf{n}$ that is defined as

$$\mathbf{t}(\mathbf{x}, t, \mathbf{n}) = \boldsymbol{\sigma}(\mathbf{x}, t)\mathbf{n} \tag{A.10}$$

where $\boldsymbol{\sigma}$ is the symmetric Cauchy (or true) stress tensor.

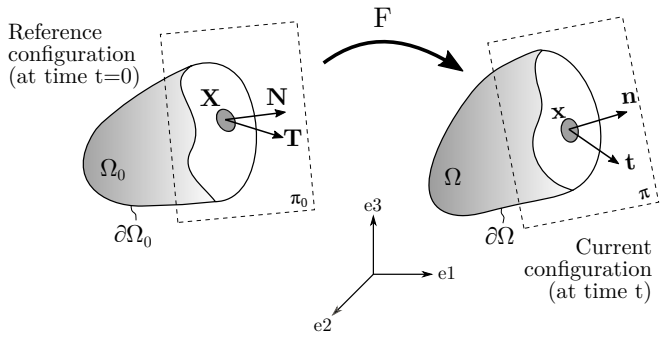

Figure A.2 Traction vectors acting on infinitesimal surface elements expressed in reference and current configurations, adapted from Holzapfel (2000).

Taking the same body $\mathcal{B}$ in the initial configuration, the position vector, normal vector and surface elements are represented by $\mathbf{X}$, $\mathbf{N}$ and $\mathbf{T}$, where the lastly is known as the first Piola-Kirchhoff traction vector. Equivalent to the current configuration, the stress tensor in the reference configuration can be written as

$$\mathbf{T}(\mathbf{X}, t, \mathbf{N}) = \mathbf{P}(\mathbf{X}, t)\mathbf{N} \tag{A.11}$$

where $\mathbf{P}$ is the non-symmetric first Piola-Kirchhoff stress tensor.

Applying Nanon's formula, it is possible to relate both stress tensors as

$$\mathbf{P}(\mathbf{X}, t) = J\boldsymbol{\sigma}(\mathbf{x}, t)\mathbf{F}^T \tag{A.12}$$

Moreover, when intermediate configurations are introduced in kinematics, other common stress tensors can be useful. Two of these are the second Piola-Kirchoff (symmetric) stress tensor $\mathbf{S}$ and Mandel stress tensors (non-symmetric) $\mathbf{M}$

$$\begin{aligned} \mathbf{S} &= J\mathbf{F}^{-1}\boldsymbol{\sigma}\mathbf{F}^{-T} \\ \mathbf{M} &= \mathbf{C}\mathbf{S} \end{aligned} \tag{A.13}$$

A.3 Balance laws

During the development of constitutive equations for a material, it is important to obey some physical principles that are introduced in this section: conservation of mass,

conservation of linear momentum, conservation of angular momentum and the first and second laws of thermodynamics.

A.3.1 Conservation of mass

The law of conservation of mass states that *the mass of a body can neither be created nor destroyed*. Therefore, if there is no exchange of material with the surroundings, the mass of a body is a conserved quantity and the time derivate of total mass must be zero

$$\frac{\mathrm{D}}{\mathrm{D}t}\int_{\Omega_0}\rho_0(\mathbf{X})\mathrm{d}V = \frac{\mathrm{D}}{\mathrm{D}t}\int_{\Omega}\rho(\mathbf{x},t)\mathrm{d}V = 0 \tag{A.14}$$

where $\rho_0(\mathbf{X})$ and $\rho(\mathbf{x},t)$ are the reference and current configurations mass densities, respectively. The equation (A.14) is the balance law that can be converted to field equations valid at each point of the body. Taking the first part of the equation, the domain Ω_0 is not dependent on time, therefore, the time derivative operator can be moved inside the integral sign

$$\int_{\Omega_0}\frac{\mathrm{D}}{\mathrm{D}t}[\rho_0(\mathbf{X})]\mathrm{d}v = 0 \tag{A.15}$$

Hence the field equation for mass concentration in the reference configuration is

$$\dot{\rho}_0(\mathbf{X}) = 0 \tag{A.16}$$

In the case of the field equation for mass conservation expressed in the current configuration, the volume integral is over Ω, which changes with time. Using the variable substitution $\mathbf{x} = \chi(\mathbf{X},t)$, and the definition of Jacobian, $\mathrm{d}v = J(\mathbf{X},t)(\mathbf{X},t)\mathrm{d}V$, the mass conservation in current configuration can be rewritten as

$$\int_{\Omega_0}[\rho_0(\mathbf{X}) - \rho(\chi(\mathbf{X},t),t)J(\mathbf{X},t)]\mathrm{d}V = 0 \tag{A.17}$$

where V is a generic volume of the solid. Hence, the previous equation must be fulfilled everywhere, leading to the continuity mass equation

$$\rho_0(\mathbf{X}) = J(\mathbf{X},t)\rho(\mathbf{X},t) \tag{A.18}$$

A.3.2 Conservation of linear momentum

Focusing on deformable bodies undergoing large deformation, the balance of linear momentum can be stated as *the sum of surface and volumetric forces acting on a body are equal to the time derivative of the linear momentum of the body*. Mathematically,

this principle can be expressed in the current configuration as

$$\frac{\mathrm{D}}{\mathrm{D}t}\int_{\Omega}\rho\mathbf{v}\mathrm{d}v=\int_{\partial\Omega}\mathbf{t}\mathrm{d}s+\int_{\Omega}\mathbf{b}\mathrm{d}v \tag{A.19}$$

where $\mathbf{v}(\mathbf{x},t)$ is the velocity field, $\mathbf{t}$ is the Cauchy vector field of surface tractions acting on the surface of the body $\partial\Omega$ in the current configuration, and $\mathbf{b}$ is the vector field of body surfaces per unit current volume.

Applying the Cauchy stress theorem, the divergence theorem and the conservation of mass principle, Equation (A.19) can be expressed as

$$\int_{\Omega}[div\boldsymbol{\sigma}+\mathbf{b}-\rho\dot{\mathbf{v}}]\mathrm{d}v=0 \tag{A.20}$$

which is called Cauchy's first equation of motion. This relation holds for any volume, therefore, it can be rewritten in local form as

$$div\boldsymbol{\sigma}+\mathbf{b}-\rho\dot{\mathbf{v}}=0 \tag{A.21}$$

This expression can be also presented in the reference configuration which is written as

$$div\mathbf{P}+\mathbf{B}-\rho_0\dot{\mathbf{V}}=0 \tag{A.22}$$

A.3.3 Conservation of angular momentum

Focusing on deformable bodies undergoing large deformation, the balance of angular momentum can be stated as *the sum of moments from surface and volumetric forces acting on a body are equal to the time derivative of angular momentum of the body.* In the current configuration, this balance law can be written as

$$\frac{\mathrm{D}}{\mathrm{D}t}\int_{\Omega}\mathbf{x}\times\rho\mathbf{v}\mathrm{d}v=\int_{\partial\Omega}\mathbf{x}\times\mathbf{t}\mathrm{d}s+\int_{\Omega}\mathbf{x}\times\mathbf{b}\mathrm{d}v \tag{A.23}$$

where $\mathbf{x}$ is the position vector.

Applying the Cauchy stress theorem and the divergence theorem on the first term on right side of the equal, Equation (A.23) is expressed as

$$\int_{\Omega}\mathbf{x}\times[\rho\dot{\mathbf{v}}-div\boldsymbol{\sigma}-\mathbf{b}]\mathrm{d}v=\int_{\Omega}\epsilon:\boldsymbol{\sigma}^{T}\mathrm{d}v \tag{A.24}$$

where ϵ is a third order permutation tensor.

Using the equation of motion previously described, it is obtained that $\epsilon:\boldsymbol{\sigma}^{T}=0$, and therefore, the equivalent condition

$$\boldsymbol{\sigma}=\boldsymbol{\sigma}^{T} \tag{A.25}$$

Hence, the balance of angular moment is satisfied if the linear moment and Cauchy stress is symmetric.

A.3.4 First law of thermodynamics

Considering a body $\mathcal{B}$ as a closed system occupying a region Ω with a boundary surface $\partial\Omega$ at time t, that has an internal volumetric heat generation r and heat flux $\mathbf{q}$ through the boundary to the surrounding, and is exposed to a surface traction $\mathbf{t}$ and body forces $\mathbf{b}$, the first law of thermodynamic state that *the rate of energy increase in the system is equal to the sum of the rate of heat supplied to the system and the rate of work done by external forces on the system.*

Mathematically, this first law can be written in the current configuration as

$$\frac{\mathrm{D}}{\mathrm{D}t}\int_{\Omega}\left(e+\frac{\rho}{2}\mathbf{v}\cdot\mathbf{v}\right)\mathrm{d}v=\int_{\partial\Omega}-\mathbf{q}\cdot\mathbf{n}\mathrm{d}s+\int_{\Omega}r\mathrm{d}v+\int_{\partial\Omega}\mathbf{t}\cdot\mathbf{v}\mathrm{d}s+\int_{\Omega}\mathbf{b}\cdot\mathbf{v}\mathrm{d}v \tag{A.26}$$

where e is the specific internal energy per unit volume.

The first term of Equation (A.26) that expresses the time derivation of the internal and kinetic energies can be simplified using $\mathrm{d}v=J(\mathbf{X},t)\mathrm{d}V$ and $\mathrm{D}/\mathrm{D}t(\rho J)=0$ as

$$\begin{aligned}\frac{\mathrm{D}}{\mathrm{D}t}\int_{\Omega}\left(e+\frac{\rho}{2}\mathbf{v}^2\right)\mathrm{d}v=\frac{\mathrm{D}}{\mathrm{D}t}\int_{\Omega_0}\left(eJ+\frac{\rho}{2}\mathbf{v}^2J\right)\mathrm{d}V=\\ \int_{\Omega_0}\left(\dot{e}J+e\dot{J}+\frac{1}{2}\frac{\mathrm{D}}{\mathrm{D}t}(\rho+J)\mathbf{v}^2+\dot{\mathbf{v}}\cdot\mathbf{v}J\rho\right)\mathrm{d}V=\\ \int_{\Omega}\left(\dot{e}+ediv\mathbf{v}+\rho\dot{\mathbf{v}}\cdot\mathbf{v}\right)\mathrm{d}v\end{aligned} \tag{A.27}$$

Combining (A.26) and (A.27), and applying the divergence theorem to the rate of heat supply to the system and the rate of work done by the external surface forces, the field equation for the energy conservation in the current configuration can be obtained from the Cauchy's first equation of motion Equation(A.21) as

$$\boldsymbol{\sigma}:\mathbf{d}-div\mathbf{q}+r=\dot{e}+ediv\mathbf{v} \tag{A.28}$$

In the same way, the field equation can be expressed in the reference configuration as

$$\mathbf{P}:\dot{\mathbf{F}}-Div\mathbf{Q}+R=\dot{e}_0 \tag{A.29}$$

A.3.5 Second law of thermodynamics

The second law of thermodynamics states that *the entropy of a thermally activated isolated macroscopic system never decreases.* In addition, for a deformable it can be written as *the rate of entropy accumulation in the system is equal to the sum of the rate of entropy input through heat transfer, rate of entropy input due to volumetric heat generation and*

rate of entropy production due to irreversible processes, that mathematically is expressed in the reference and current configurations as

$$\begin{aligned} \frac{\mathrm{D}}{\mathrm{D}t}\int_{\Omega_0}\eta_0 \mathrm{d}V &= \int_{\partial\Omega_0} -\frac{\mathbf{Q}\cdot\mathbf{N}}{\theta_0}\mathrm{d}S + \int_{\Omega_0}\frac{R}{\theta_0}\mathrm{d}V + \Gamma \\ \frac{\mathrm{D}}{\mathrm{D}t}\int_{\Omega}\eta \mathrm{d}v &= \int_{\partial\Omega} -\frac{\mathbf{q}\cdot\mathbf{n}}{\theta}\mathrm{d}s + \int_{\Omega}\frac{r}{\theta}\mathrm{d}v + \Gamma \end{aligned} \tag{A.30}$$

where η_0 and η are the entropy of the system per unit reference and current volume, $\theta_0(\mathbf{X},t)$ and $\theta(\mathbf{x},t)$ are the temperature of the system, and $\Gamma \geq 0$ is the entropy generation rate due to irreversible mechanisms. These equations are referred as the Clausius-Duhem equation, and using the divergence theorem can be expressed as

$$\begin{aligned} \dot{\eta}_0 &\geq -Div\left(\frac{\mathbf{Q}}{\theta_0}\right) + \frac{R}{\theta_0} \\ \dot{\eta} + \eta div\mathbf{v} &\geq -div\left(\frac{\mathbf{q}}{\theta}\right) + \frac{r}{\theta} \end{aligned} \tag{A.31}$$

A.4 Hyperelastic constitutive equations

A hyperelastic material postulates the existence of a Helmholtz free-energy function Ψ defined per unit of reference volume as

$$\Psi = e_0 - \theta_0\eta_0 \tag{A.32}$$

This thermodynamic potential measures the useful work from a closed system considering constant temperature. For the definition of Ψ it is possible to obtain the rate of internal energy as

$$\dot{e}_0 = \dot{\Psi} + \dot{\theta}_0\eta_0 + \theta_0\dot{\eta}_0 \tag{A.33}$$

A constitutive equation is a relationship between the strain and some physical variables such as stress and describes the mechanical behaviour of a specific material. Regarding the development of constitutive equations, these need to satisfy the balance laws in order to ensure thermodynamic consistency. In this regard, it is possible to combine the first Equation (A.29) and the second law of the thermodynamic Equation (A.31) to express the Clausius-Duhem equation in terms of energy potentials and stress tensor as

$$\dot{\eta}_0 + Div\left(\frac{\mathbf{Q}}{\theta_0}\right) - \frac{\dot{e}_0}{\theta_0} + \frac{\mathbf{P}:\dot{\mathbf{F}}}{\theta_0} - \frac{Div\mathbf{Q}}{\theta_0} \geq 0 \tag{A.34}$$

Expanding the divergence operator this equation can be rewritten as

$$\mathbf{P}:\dot{\mathbf{F}} - \dot{e}_0 + \theta_0\dot{\eta}_0 - \frac{\mathbf{Q}Grad\theta_0}{\theta_0} \geq 0 \tag{A.35}$$

Inserting the expression of $\dot{e}_0$ Equation (A.33), it is possible to obtain

$$\mathbf{P} : \dot{\mathbf{F}} - \dot{\Psi} - \dot{\theta}_0 \eta_0 - \frac{\mathbf{Q} Grad\theta_0}{\theta_0} \geq 0 \tag{A.36}$$

Finally, assuming that Ψ is a function of the deformation gradient, temperature and temperature gradient (considered for this case d(Gradθ_0)/dt=0), the equation become

$$\left(\mathbf{P} - \frac{\partial \Psi}{\partial \mathbf{F}} \right) : \dot{\mathbf{F}} - \left(\frac{\partial \Psi}{\partial \theta_0} + \eta_0 \right) \dot{\theta}_0 - \frac{\mathbf{Q} Grad\theta_0}{\theta_0} \geq 0 \tag{A.37}$$

B Planes

This Appendix introduces the planes of the grips designed specifically for the tensile test carried out in this thesis.

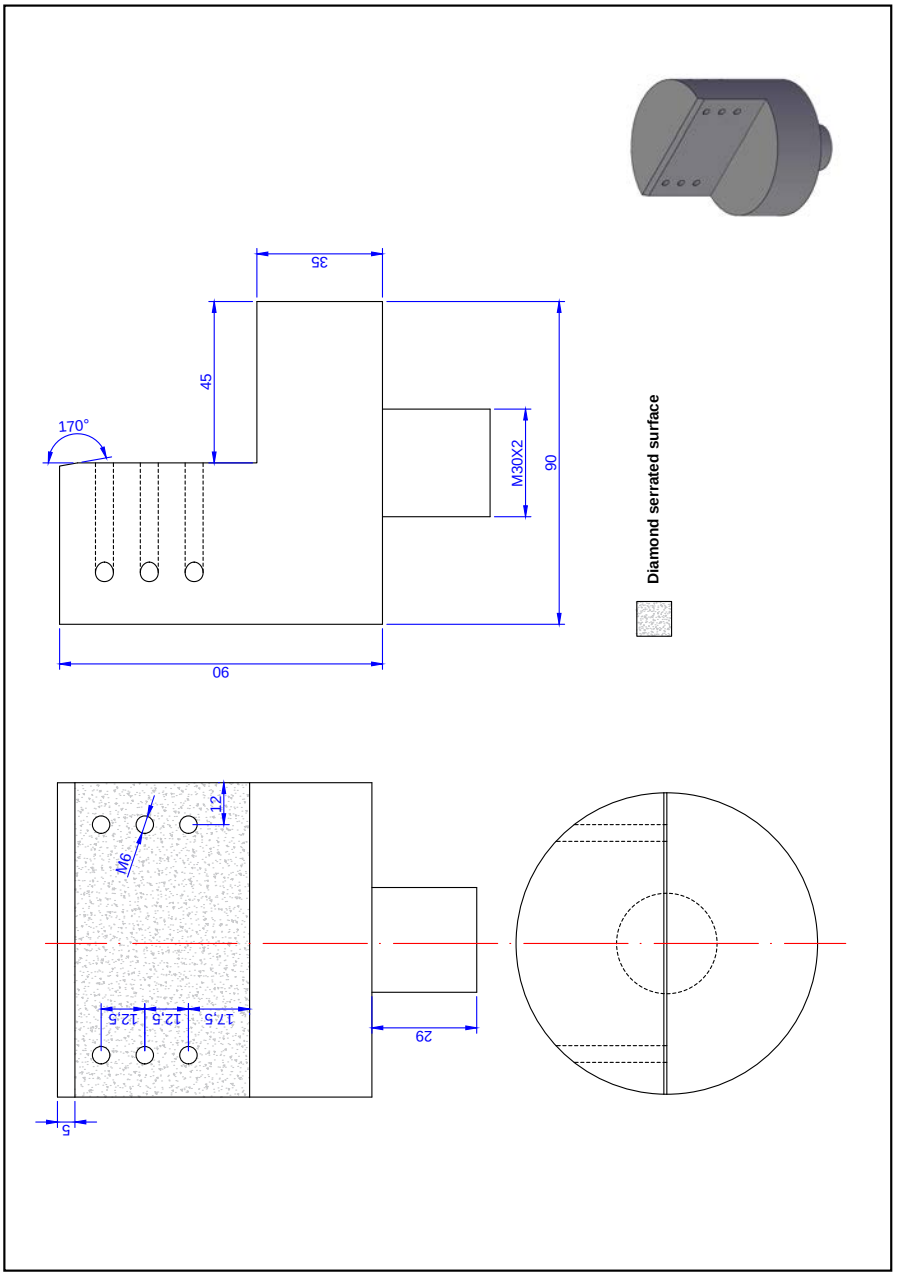

Figure B.1 Lower grip.

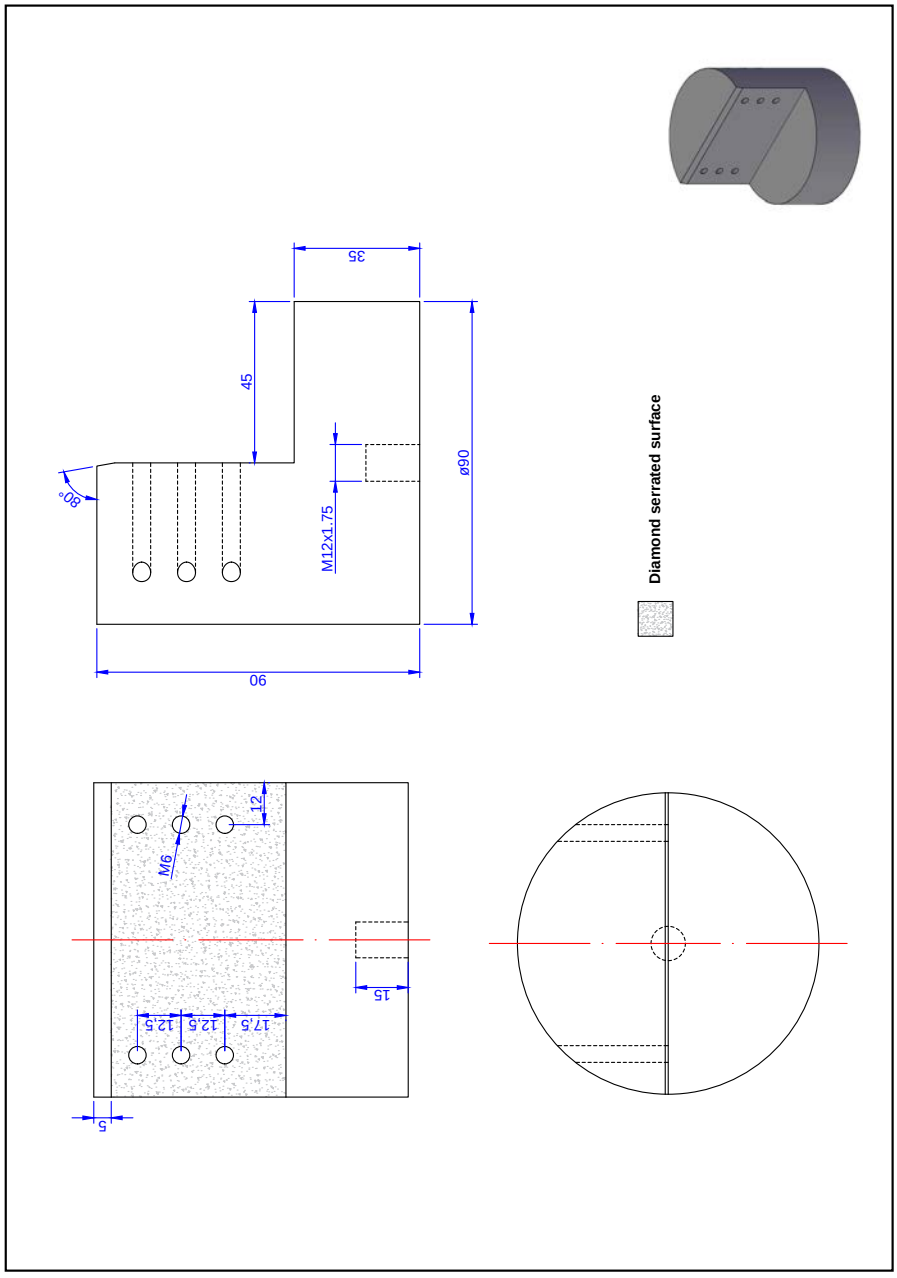

Figure B.2 Upper grip.

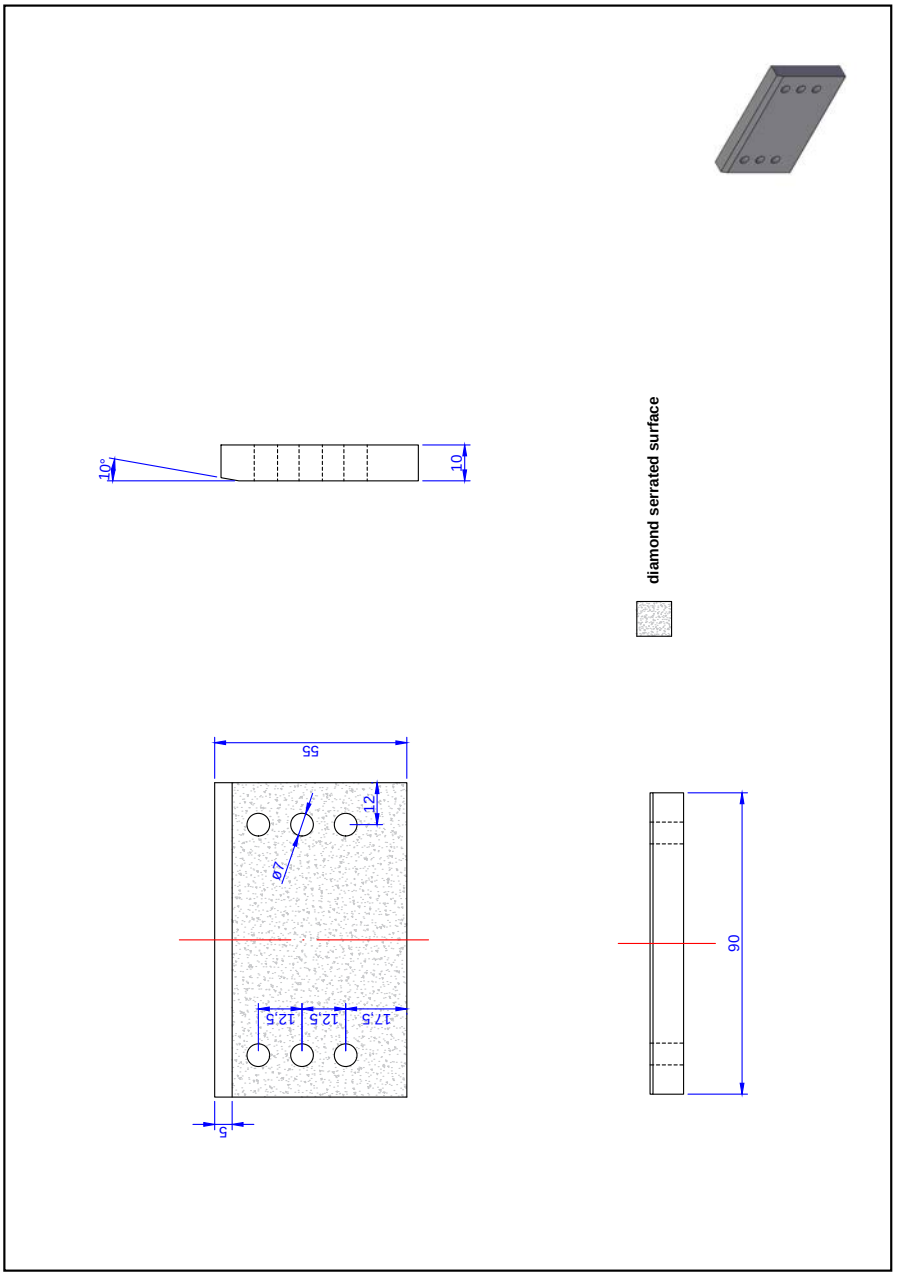

Figure B.3 Caps.